Unravelling the role of mitochondrial dysfunction in core myopathies

Jennifer Sharpe

University College London

PhD

2016

I, Jennifer Sharpe, confirm that the work presented in this thesis is my own. Where information has been derived from other sources, I confirm that this has been indicated in the thesis.

Signed: Date:

Acknowledgements

I would like to thank my principal supervisor, Professor Michael Duchen, for his guidance and valuable insight over the course of this PhD. I am also very grateful to Professor Gyuri Szabadkai, who has given me a lot of help and advice. To my colleagues within the Duchen/Szabadkai lab, thank you for your encouragement and support - through the good times and the bad! I would also like to show my appreciation to Professor Francesco Muntoni at the Institute of Child Health and his ex-postdoctoral researcher, Dr Iulia Oprea, Paul Levy and his staff at the KLB animal facility, Sam Ranasinghe at the Medical Sciences imaging facility and Muscular Dystrophy UK for contributing to the funding of this research. Finally, I would like to thank my family, friends and boyfriend Chris, for fuelling my determination to succeed (at being a true nerdwin!)

Abstract

Core myopathies are a diverse group of congenital muscle diseases, which typically present with proximal muscle weakness, hypotonia and delayed motor milestones. Biopsies from affected individuals display 'core' areas that lack mitochondrial staining; despite cores being a pathological hallmark for these diseases, their formation and development is not well understood. In this thesis I have explored the involvement of mitochondrial dysfunction in core myopathy pathology by studying different models with mutations of proteins involved in intracellular calcium (Ca^{2+}) homeostasis.

The first model discussed is a new mouse sub-line carrying the I4898T mutation in RYR1. RYR1 codes for a Ca^{2+} release channel on the sarcoplasmic reticulum (SR) called Ryanodine Receptor 1 (RyR1), and given that mitochondria localise close to the SR, a faulty RyR1 is likely to upset the Ca^{2+} balance that is required for mitochondrial function. In contrast to studies of other RyR1 I4898T models, I did not observe reduced SR-stimulated Ca^{2+} release in myotubes or myofibres isolated from the heterozygous mice. Consequently, no defects in mitochondrial localisation, respiration or biogenesis were identified.

The second model discussed is fibroblasts from a patient with a mutation in STAC3, which codes for an adaptor protein that is thought to be involved in excitation-contraction coupling. While histamine-induced Ca^{2+} signals were elevated in the patient fibroblasts, resting mitochondrial membrane potential was reduced. As STAC3 is predominantly expressed in skeletal muscle, these results are difficult to interpret and highlight the need for a future skeletal muscle model.

The final model consists of fibroblasts from individuals that have loss-of-function mutations in MICU1, which codes for a Ca^{2+} sensor that regulates the opening of the Mitochondrial Ca^{2+} Uniporter. The mitochondria in these MICU1-deficient fibroblasts are fragmented, exhibit accelerated mitochondrial Ca^{2+} uptake and are Ca^{2+}-loaded at rest. While mitochondrial membrane

potential and respiration appear normal, there is evidence for a futile Ca^{2+} cycle across the mitochondrial membrane, which illustrates the bioenergetic cost of mitochondrial Ca^{2+} accumulation.

Publications arising from this work

Bhosale G, **Sharpe JA**, Sundier SY & Duchen MR, 2015. Calcium signaling as a mediator of cell energy demand and a trigger to cell death. *Annals of the New York Academy of Sciences*, 1350(1), pp.107–116.

Logan CV*, Szabadkai GS*, **Sharpe JA***, Parry DA, Torelli S, Childs A, Kriek M, Phadke R, Johnson CA, Roberts NY, Bonthron DT, Munteanu I, Foley AR, Wheway G, Szymanska K, Natarajan S, Abdelhamed ZA, Morgan JE, Roper H, Santen GWE, Niks EH, Ludo van der Pol W, Lindhout D, Raffaello A, De Stefani D, den Dunnen JT, Sun Y, Ginjaar L, Sewry CA, Hurles M, Rizzuto R, UK10K Consortium, Duchen MR, Muntoni F & Sheridan E, 2014. Loss-of-function mutations in MICU1 cause a brain and muscle disorder linked to primary alterations in mitochondrial calcium signaling. *Nature genetics*, 46(2), pp.188–93.

* These authors contributed equally to this publication

List of abbreviations

$\Delta\Psi_m$	Mitochondrial membrane potential
ΔMICU1	MICU1-deficient
ADP	Adenosine diphosphate
AEQ	Aequorin
AMP	Adenosine monophosphate
ATP	Adenosine triphosphate
BCA	Bicinchoninic acid
BSA	Bovine serum albumin
Ca^{2+}	Calcium
$[Ca^{2+}]_c$	Cytosolic calcium concentration
$[Ca^{2+}]_m$	Mitochondrial calcium concentration
CCD	Central core disease
Co-A	Coenzyme A
Cyt c	Cytochrome c
DHPR	Dihydropyridine receptor
DMEM	Dulbecco's Modified Eagle's Medium
DNA	Deoxyribonucleic acid
DRP1	Dynamin-related protein 1
EC	Excitation-contraction
EDL	Extensor digitorum longus
ER	Endoplasmic reticulum
FAD^+	Flavin adenine dinucleotide
FADH	Reduced form of flavin adenine dinucleotide
FBS	Fetal bovine serum
FCCP	Carbonyl cyanide-4-(trifluoromethozy)phenylhydrazone
FDB	Flexor digitorum brevis

GTP	Guanosine triphosphate
H^+	Hydrogen ion (proton)
H_2O	Water
HOM	Homozygote
HET	Heterozygote
IMDM	Iscove's Modified Dulbecco's Medium
IMM	Inner mitochondrial membrane
IMS	Intermembrane space
IP_3	Inositol triphosphate
IP_3R	Inositol triphosphate receptor
iPSC	Induced pluripotent stem cell
KD	Knock-down
kDa	Kilo Daltons
KDS	King-Denborough syndrome
KO	Knock-out
MCU	Mitochondrial Calcium Uniporter
MHS	Malignant hyperthermia susceptibility
MICU1	Mitochondrial Calcium Uptake 1
MmD	Multiminicore disease
mPTP	Mitochondrial Permeability Transition Pore
mRNA	Messenger ribonucleic acid
mtDNA	Mitochondrial DNA
MyoD	Myogenic Differentiation 1
NAD^+	Nicotinamide adenine dinucleotide
NADH	Reduced form of nicotinamide adenine dinucleotide
NAM	Native American Myopathy
NCX	Sodium-calcium exchanger
OMM	Outer mitochondrial membrane

O_2	Oxygen
OXPHOS	Oxidative phosphorylation
PBS	Phosphate buffered saline
PDH	Pyruvate dehydrogenase
PDHC	Pyruvate dehydrogenase complex
PDP	Pyruvate dehydrogenase phosphatase
P_i	Phosphate
PMF	Proton-motive force
PS	Penicillin-streptomycin
Q	Quinone
RB	Recording buffer
ROI	Region of interest
ROS	Reactive oxygen species
RT	Room temperature
RyR1	Ryanodine receptor 1
SEM	Standard error of the mean
SH3	SRC Homology 3 domain
SR	Sarcoplasmic reticulum
STAC3	SH3 and cysteine-rich domain 3
TFAM	Mitochondrial Transcription Factor A
TMRM	Tetramethylrhodamine methyl ester
WT	Wild type

List of contents

List of figures

List of tables

Chapter 1 Introduction

Mitochondria play significant roles in cell and tissue physiology, including energy homeostasis, Ca^{2+} signalling and redox balance. They are regulators of not only cell life but cell death, and mitochondrial dysfunction contributes to a wide range of human diseases. In this thesis I have explored the proposition that mitochondrial dysfunction contributes to the pathophysiology of core myopathies. First, I have provided a broad overview of skeletal muscle physiology, core myopathy research and mitochondrial biology. I have then presented functional data from three different core myopathy cell models, which are finally discussed and evaluated in line with my research hypothesis.

1.1 Skeletal muscle physiology

1.1.1 Skeletal muscle structure

The skeletal muscles are the effector organs of the locomotor system, or musculoskeletal system, which is responsible for movement. They consist of bundles of multinucleated cells, called myofibres, which run roughly parallel to the line of muscle action (Figure 1.1) (Sciote & Morris 2014). Within each individual myofibre are protein filaments called myofibrils, which are subdivided into contractile elements known as sarcomeres (Figure 1.1). Sarcomeres work co-operatively so that when muscle contraction occurs, tension develops along the axis of the myofibrils and therefore along the myofibre itself. Sarcomeres are also directionally aligned across the myofibrils, giving the muscle a distinct 'striated' appearance consisting of light and dark bands. These bands are named after their birefringent properties under the light microscope: the light band is isotropic (I band) and the dark band is anisotropic (A band) (Jones & Round 1990) (Figure 1.1).

Each myofibril is a bundle of contractile protein filaments called myofilaments. There are two major types of myofilaments: thick filaments and thin filaments, which are large polymers of myosin II and actin, respectively. While the myosin (thick) filaments make up the A band, the actin (thin) filaments make up the I band. The thick and thin filaments interdigitate to form a hexagonal lattice (Lieber 1992). The thin filaments of each sarcomere overlap at the 'Z lines', which define the area of each sarcomere (Figure 1.1). The region where there is no actin-myosin overlap is called the H zone (Figure 1.1).

Figure removed due to copyright restrictions

Figure 1.1: Hierarchy of skeletal muscle organisation

Figure taken from (Bloom & Forcett 1968).

Each thin filament comprises two helical strands made up of G-actin monomers, which each have a myosin binding site. Tropomyosin winds along the groove of this actin double helix and effectively 'hides' the actin-myosin binding sites when the muscle is relaxed. Associated with tropomyosin is a protein complex called troponin, which is made up of three subunits: Tn-T, which binds to tropomyosin and regulates the interaction of the troponin complex with the thin filaments; Tn-C, which binds Ca^{2+} released during excitation-contraction coupling (discussed in 1.1.3), triggering a conformational change in the tropomyosin-troponin complex that exposes the myosin binding sites and permits actin-myosin interaction; and Tn-I, which exerts an inhibitory influence on tropomyosin when Ca^{2+} is not present (Lieber 1992).

Myosins are motor proteins that interact with actin molecules and use ATP hydrolysis to 'walk' along the actin filament. In skeletal muscle, each myosin II molecule consists of two identical heavy chains wound around each other to form a rod portion that points to the centre of the sarcomere as well as two heads that extend laterally (Figure 1.1). The myosin heads of the thick filaments are able to bind actin in the thin filaments, forming attachments called cross bridges. ATP hydrolysis allows the cross bridges to generate force through a power stroke movement (Figure 1.2). As long as ATP and Ca^{2+} are present in the cytoplasm of the myofibre, repeated ATP hydrolysis and power strokes occur in what is known as the cross bridge cycle (Figure 1.2). The resulting effect is that the thin filament is being 'pulled' by the myosin heads of the thick filament, causing both filaments to slide past each other. This reduces the size of the sarcomeres, shortening the myofibres (and the entire muscle) into a contracted state.

Figure removed due to copyright restrictions

Figure 1.2: Cross bridge cycle

When no nucleotide is bound, the myosin head binds actin tightly in a 'rigor' state. When ATP binds (1), the interaction between the myosin head and actin weakens, causing the cross bridge to detach. The myosin head then hydrolyses the ATP (2), causing a conformational change that moves it to a new position where it can bind a different actin molecule. As phosphate (P_i) dissociates from the ATP binding pocket (3), the myosin head undergoes the power stroke, which restores myosin to the rigor state and forces the myosin to move the actin filament. ADP is then released (4). Diagram adapted from figure 18.25 in (Lodish et al. 2000).

1.1.2 Skeletal muscle fibre types

Skeletal muscle fibres are generally classified according to the type of myosin heavy chain that is predominantly expressed. While type I fibres contain mostly slow-contracting myosins, type II fibres are made up of fast-contracting myosins. For this reason, type I and II fibres are also referred to as slow-twitch and fast-twitch fibres, respectively. Type II fibres can be classified further according to their metabolic properties: type IIa (fast-twitch oxidative fibres) and IIb (fast-twitch glycolytic fibres). These three main fibre types are adapted for different purposes and so have different properties (summarised in Table 1.1 below).

	Type I	Type IIa	Type IIb
Contraction time	Slow	Moderately fast	Fast
Muscle fibre diameter	Small	Intermediate	Large
Oxidative capacity	High	Intermediate	Low
Fatigue resistance	High	Intermediate	Low
Power produced	Low	Medium	High
Mitochondrial content	High	High	Low
Myoglobin content	High	High	Low
Myosin heavy chain	I	IIa	IIb
Myosin ATPase activity	Low	High	High

Table 1.1: Characteristics of different muscle fibre types

1.1.3 Skeletal muscle innervation

Unlike cardiac and smooth muscles, skeletal muscles are under voluntary control. The stimulus for physiological skeletal muscle activity is always derived from an electrical impulse, or action potential, which comes from the neurons that innervate the skeletal muscle (the motorneurons). When a motorneuron in the brain stem or spinal cord is activated, the generated

action potential travels down its myelinated axon to its branches in the muscle. Myelin insulation does not cover the entire length of the axon; there are periodic gaps called nodes of Ranvier. The concentration of voltage-dependent sodium channels in the axon membrane at each node, and electrical insulation of the fatty myelin sheath, ensure that action potentials rapidly jump from node to node by a process known as saltatory conduction (ffrench-Constant et al. 2004).

Collectively, a motorneuron and the muscle fibres it innervates are called a 'motor unit'. Once a motorneuron is activated, all of the muscle fibres in one motor unit will contract at the same time, producing a synchronous electrical discharge (action potential) and generation of force (twitch) (Jones & Round 1990). The number of muscle fibres per motor unit varies from muscle to muscle. The smallest motor units, containing as few as 3-10 muscle fibres, are found in muscles used for intricate fine movements (Hopkins 2006), for example in a small hand muscle. Much larger motor units, containing up to several hundred muscle fibres, are predominant in larger muscles used for gross vigorous movements (Hopkins 2006), such as the quadriceps. Motor units also differ in the type of muscle fibres they innervate; motor units that innervate small type I fibres are generally referred to as slow motor units, whereas the motor units that innervate type II fibres are called fast motor units.

The neuromuscular junction is the synaptic connection between the axon branch of the motorneuron and the skeletal muscle fibre (Figure 1.3). Upon the arrival of an action potential at the presynaptic terminal, voltage-dependent calcium channels open and there is an influx of Ca^{2+} from the extracellular fluid into the cytosol of the presynaptic bulb. This increase in Ca^{2+} concentration causes vesicles containing the neurotransmitter acetylcholine (ACh) to fuse with the presynaptic membrane and release their contents into the synaptic cleft (Jones & Round 1990). The ACh molecules diffuse across the cleft and fit into acetylcholine receptors (AChRs) in the postsynaptic muscle fibre membrane, referred to as the motor endplate,

which is invaginated to increase the surface area exposed to the synaptic cleft (Figure 1.3).

Binding of ACh to the AChRs causes a depolarisation of the muscle fibre membrane (referred to as the sarcolemma) (Figure 1.3). A regenerative action potential is initiated and propagates down the length of the muscle fibre. The sarcolemma is characterised by deep invaginations called transverse tubules (t-tubules) that allow the action potential to reach the fibre's interior. The t-tubule system is closely associated with the longitudinal sarcoplasmic reticulum (SR), which is the primary intracellular Ca^{2+} storage/release organelle found in striated muscles.

Figure removed due to copyright restrictions

Figure 1.3: Neuromuscular junction

When an action potential reaches the presynaptic terminal, Ca^{2+} channels open causing vesicles containing ACh (purple) to fuse with the presynaptic membrane and release ACh into the synaptic cleft. Binding of ACh to AChRs (green) in the sarcolemma triggers the opening of cationic channels thus regenerating the action potential. Figure taken from (Swaiman et al. 2011).

1.1.4 Skeletal muscle ryanodine receptor

The principal Ca^{2+} release channel on the SR is called the ryanodine receptor (RyR). The RyR family consists of three isoforms: RyR1, which was first identified in skeletal muscle (Takeshima et al. 1989; Zorzato et al. 1990), RyR2 in cardiac muscles (Nakai et al. 1990; Otsu et al. 1990), and RyR3, which was first found in the brain (Hakamata et al. 1992). Although RyR1 and RyR2 are predominantly expressed in skeletal muscle and cardiac muscle, respectively, all three isoforms are found in a wide range of tissues (Lanner et al. 2010). The RyR family are named after the plant alkaloid ryanodine, which locks the channels in an open subconductance state at nanomolar concentrations and inhibits at high concentrations (>100μM) (Lanner et al. 2010).

RyRs form homotetramers with a total molecular mass of >2MDa (Lai et al. 1988; Inui et al. 1987). This enormous size has made structural analysis challenging, but recent technological advancements in single particle cryo-electron microscopy have allowed three groups to independently solve the structure of RyR1. The tetrameric complex has a mushroom-like shape, with each monomer consisting of an extensive cytoplasmic N terminus on a short stalk (Figure 1.4), which is made up of six transmembrane segments (Zalk et al. 2015; Efremov et al. 2015; Yan et al. 2015).

Figure removed due to copyright restrictions

Figure 1.4: Structure of the RyR1 channel

Cross-sectional arrangement of the RyR1 channel in the closed conformation (left) and in the presence of Ca^{2+} (right). Purple dots illustrate Ca^{2+}-binding EF hands.

Black arrow indicates movement of each monomer during channel opening. Figure adapted from (Kuo & Ehrlich 2015).

The N terminal domain of RyR1 can directly interact with a voltage-dependent Ca^{2+} channel called the dihydropyridine receptor (DHPR). DHPRs are situated within the t-tubules, which are flanked on each side by the RyR1-studded terminal cisternae of the SR (forming a 'triad'). The physical link between RyR1 and DHPR is important for excitation-contraction (EC) coupling, which converts the incoming action potential into a mechanical event via intracellular Ca^{2+} release (Figure 1.5); Ca^{2+} binds Tn-C and triggers a conformational change in the tropomyosin-troponin complex, which allows actin-myosin interaction to occur and cross-bridge cycling to take place (see section 1.1.1).

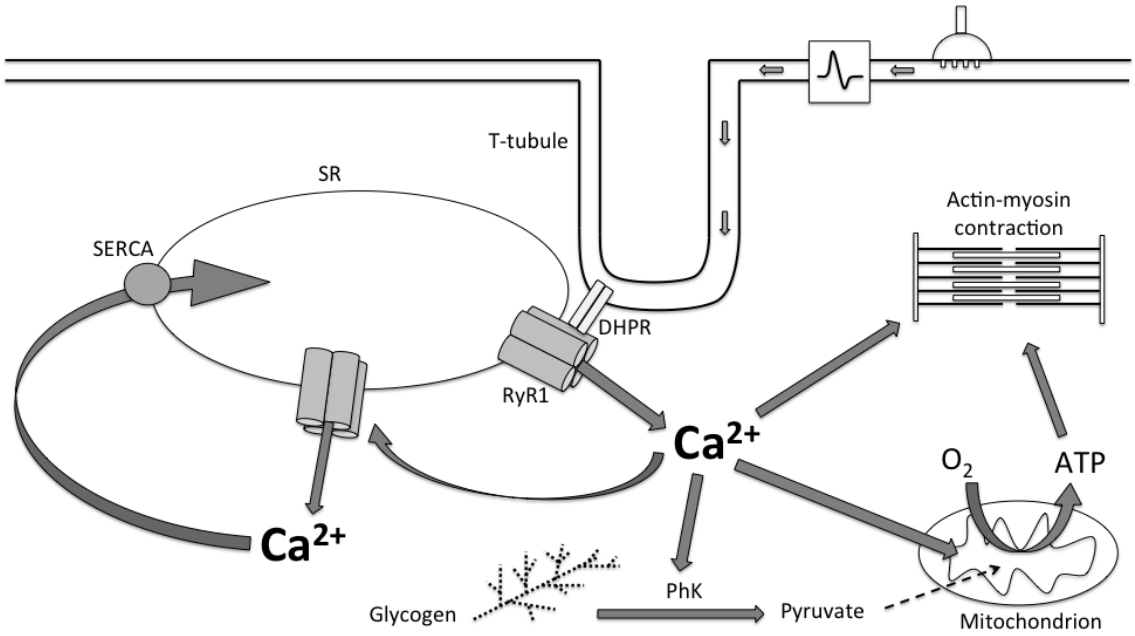

Figure 1.5: EC coupling in a skeletal muscle cell

Action potentials propagate along the sarcolemma from the neuromuscular junction to the t-tubules, where they activate voltage-sensitive DHPRs and cause a conformational change that allosterically activates RyR1. The resulting SR Ca^{2+} release activates neighbouring RyR1 channels and amplifies the Ca^{2+} signal across the skeletal muscle fibre. This Ca^{2+} signal triggers actin-myosin contraction, increases mitochondrial metabolism and causes glycogen breakdown via phosphorylase kinase (PhK) activation. When the nerve impulse stops and the sarcolemma repolarises, Sarco/Endoplasmic Reticulum ATPase (SERCA) actively pumps Ca^{2+} back into the SR, gradually decreasing $[Ca^{2+}]_c$ until relaxation occurs.

The opening of these physically coupled RyR1 channels is referred to as 'depolarisation-induced Ca^{2+} release' (DIPR). Since RyR1 itself can be activated by Ca^{2+} - a process known as Ca^{2+}-induced Ca^{2+} release (CICR) – the DIPR signal can be rapidly amplified across the large skeletal muscle fibre. More than half of the RyR1 channel population are not coupled to DHPRs, meaning they are available to participate in the CICR process (Fill & Copello 2002).

The resulting rise in cytosolic calcium concentration ($[Ca^{2+}]_c$) activates phosphorylase kinase, which then activates glycogen phosphorylase to release glucose-1-phosphate from glycogen stores (Brostrom et al. 1971) (Figure 1.5). A rise in $[Ca^{2+}]_c$ is also associated with an increase in mitochondrial calcium concentration ($[Ca^{2+}]_m$), which in turn stimulates mitochondrial dehydrogenases (described in more detail in section 1.4.1). The consequence of these two processes is an increase in ATP generation, thus ensuring that energy supply is matched with demand.

1.2 RYR1-associated diseases

1.2.1 Core myopathy disease

Core myopathies are a clinically and genetically heterogeneous group of congenital muscle diseases for which no curative treatments are currently available (Jungbluth et al. 2011). They were first described in 1956 by Shy and Magee, who identified areas devoid of stains for oxidative enzyme activity (and thus lacking in mitochondria) in the myofibres of a family with congenital hypotonia and non-progressive proximal muscle weakness (MAGEE & SHY 1956). These areas were subsequently given the name 'cores', and as they were mostly centrally located in the myofibres, the condition was termed central core disease (CCD) (Figure 1.6A & C). A spectrum of disorders have since been characterised, including multi-minicore disease (MmD), which differs to CCD in that numerous cores are seen in the myofibres, and these do not usually extend the whole length of the fibre (Brislin & Theroux 2013) (Figure 1.6B & D). While central cores are

typically found in the mitochondria-rich type I myofibres, minicores may affect both type I and type II fibres (Jungbluth 2007a; Jungbluth 2007b). Although these diseases all share the same histopathological core hallmark, the number and position of cores within each muscle fibre varies from patient to patient, and can even vary between muscles of the same patient (Dubowitz & Roy 1970).

In 1990, linkage analysis mapped the CCD locus to chromosome 19q13 (Haan et al. 1990), which was later found to be the site of skeletal muscle specific gene, RYR1 (Quane et al. 1993; Mulley et al. 1993). Mutations in RYR1 are the most common cause of core myopathies (Jungbluth et al. 2011). While CCD-associated RYR1 mutations are dominantly inherited (Jungbluth 2007a), MmD-associated RYR1 mutations are recessively inherited (Jungbluth 2007b).

Figure removed due to copyright restrictions

Figure 1.6: Oxidative stain abnormalities in core myopathy disease

Muscle biopsy sections from patients with RYR1-related CCD (A,C), Selenoprotein N1-related MmD (B), and RYR1-related MmD (D) stained with NADH tetrazolium reductase. Adapted from (Jungbluth et al. 2011).

Although most patients with RYR1 mutations present clinical signs in infancy or early childhood, there have been reports of late-onset cases, suggesting that there could be a synergistic effect between certain RYR1 mutations and the ageing process (Jungbluth et al. 2009). Typical symptoms of RYR1 related myopathies include delayed motor milestones, hypotonia (or 'floppy infant syndrome'), proximal muscle weakness (particularly in the hip girdle) and orthopaedic complications such as scoliosis and hip dislocation (Zhou et al. 2007). Axial muscle weakness, opthalmaplegia, and respiratory impairment, which can lead to secondary cardiac failure, can additionally present in MmD (Jungbluth 2007b). The degree of disability varies greatly between core myopathy patients, even those within the same family. While cases at the severe end of the clinical spectrum present with fetal akinesia syndrome and usually do not survive the neonatal period (Romero et al. 2003), most cases are non-progressive and even improve over time; the majority of CCD patients do achieve the ability to walk independently (Jungbluth 2007a).

The prevalence of congenital myopathies is estimated to be one tenth of all cases of neuromuscular disorders, and although the core myopathies are thought to be the most common of congenital myopathies, little is known about their exact epidemiology (Jungbluth 2007a). A regional study in northern England estimated a prevalence of CCD of 1:250,000 (Norwood et al. 2009), thus classifying it as an 'ultra-rare' disease (Beck 2012). Nevertheless, the variable phenotypic expression and non-progressive nature of CCD makes it likely that several cases go undiagnosed (Quinlivan et al. 2003). In Japan, the carrier frequency for heterozygous RYR1 mutations is reported to be as high as 1:2000 (Wu et al. 2006).

1.2.2 Malignant hyperthermia susceptibility

Mutations in the RYR1 gene also result in malignant hyperthermia susceptibility (MHS), meaning patients with a core myopathy carry a high risk of MHS (Brislin & Theroux 2013). MHS is defined as a pharmacogenetic disorder that manifests as a life-threatening hypermetabolic response to

inhalational anaesthetics, the depolarising muscle relaxant succinylcholine, and rarely, in humans, to stressors such as vigorous exercise and heat (Rosenberg et al. 2015). MHS exhibits an autosomal dominant mode of inheritance. While the frequency of malignant hyperthermia (MH) reactions ranges from 1:5000 to 1:100,000 anaesthetic procedures, the prevalence of the genetic abnormalities may be as great as 1:3000 individuals (Rosenberg et al. 2015). The 'gold standard' for diagnosis of MHS is currently an in vitro contracture test (IVCT), which checks to see if contracture occurs upon addition of halothane or caffeine to isolated strips of skeletal muscle. As it requires a muscle biopsy, the IVCT is relatively invasive. A more attractive option, for both clinicians and researchers, might be to establish a primary fibroblast cell line from a small skin biopsy, which can then be converted to the muscle lineage via an induced pluripotent stem cell (iPSC) route or by viral transduction with a Myogenic Differentiation 1 (MyoD) transgene. This would not only give an insight into the pathophysiology of MHS but would also allow for investigation of novel treatments (Fernandez-Fuente et al. 2014).

1.2.3 Mutations in RYR1 disrupt EC coupling

The ability to sequence the entire RYR1 coding sequence has meant more and more genotype-phenotype correlations are emerging, which will help not only with diagnosis but also with providing advice to affected families. Historically, it has been reported that mutations associated with MHS and CCD are localised at 'hot spot' regions within the N terminal, central and C terminal domains of RyR1 (Figure 1.7). While the channel-forming C terminus is a mutation hot spot for classical CCD, the N terminal and central domains are predominantly associated with a MHS phenotype (Jungbluth et al. 2011). However, as the amount of data collated increases the borders of these hot spot regions are gradually expanding, which suggests that the hot spots originally described may have resulted from screening bias (Robinson et al. 2006). Recessively inherited mutations linked to MmD are more widespread through the RYR1 gene and are often associated with reduced RyR1 protein levels rather than RyR1 malfunction itself, which may explain

why recessive RYR1-related myopathies are usually more severe (Zhou et al. 2007).

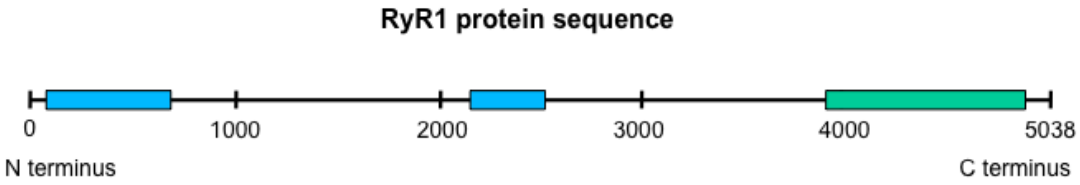

Figure 1.7: Mutation hot spots within the RyR1 protein

Mutations associated with MHS (blue) are predominantly situated in the N terminal region (1-600 amino acids (aa)) and a central region (2100-2500aa) of the RyR1 protein sequence, while mutations causing classical CCD (green) are found near the C terminus (3900-5000aa).

Previous work on core myopathy models has led to two distinct hypotheses as to how RYR1 mutations can lead to muscle weakness. The first is the 'leaky channel' hypothesis, which proposes that mutations increase the open probability of the RyR1 channel, making it constitutively active and allowing the depletion of SR Ca^{2+} stores (Zhang et al. 1993). Alternatively, RYR1 mutations can lead to 'EC uncoupled' channels, meaning SR Ca^{2+} release is no longer triggered by sarcolemmal excitation (Quane et al. 1993). Both of these mechanisms result in less Ca^{2+} being released per action potential, leading to reduced contractile activity. A reduction in SR Ca^{2+} release can also affect signals for muscle maintenance and metabolism, such as the activity of Ca^{2+} dependent effectors (De Koninck & Schulman 1998) and the Nuclear Factor of Activated T-cells (NFAT) family of transcription factors (Hogan et al. 2003). So far, mutations that result in CCD without MHS e.g. the I4898T mutation (discussed later in Chapter 2) have been linked to the EC uncoupled functional phenotype (Guerrero-Hernández et al. 2014) (Figure 1.5). Since these CCD-only mutations usually lie near the selectivity filter of the C terminus, the underlying molecular mechanism is though to be diminished Ca^{2+} permeation in the mutant channels (Avila et al. 2001; Zvaritch et al. 2007; Loy et al. 2011).

Mutations related to MHS are associated with a leaky RyR1 channel; the severity of the SR leak may dictate whether a CCD phenotype is seen in

addition to MHS (Figure 1.8). There is evidence to suggest that compensatory mechanisms, such as increased SERCA expression, are active in MHS-only models (Tong et al. 1999; Dirksen & Avila 2004), meaning SR Ca^{2+} content is normal and depolarisation-evoked Ca^{2+} release is not affected. Thus RYR1 patients with MHS alone only have a muscle phenotype when in the presence of triggering anaesthetics. During an MH episode, the RyR1 channel remains open and evokes supraphysiological levels of SR Ca^{2+} release; this leads to excessive contractile activity, heat, ATP depletion, metabolic stimulation and rhabdomyolysis (Hopkins 2011). The skeletal muscle relaxant, dantrolene, is the only known drug to specifically treat MH; although its mechanism of action is not fully understood it is thought to bind to RyR1 and inhibit SR Ca^{2+} release (Krause et al. 2004). MH-related mortality has declined since the introduction of dantrolene but remains as high as 35%, according to a study using data from the North American MH registry (Larach et al. 2010).

Figure removed due to copyright restrictions

Figure 1.8: Schematic depicting distinct cellular consequences of mutations in RyR1 that result in CCD-only, CCD with MHS, and MHS-only

Mutations that give rise to CCD in the absence of MHS (CCD-only) are thought to cause muscle weakness through EC uncoupling. Mutations that give rise to a CCD phenotype with MHS (MH+CCD) result in a hyperactive, leaky RyR1 channel, which

reduces SR Ca^{2+} content and thus the amount of Ca^{2+} available for muscle contraction. Mutations associated with MHS alone (MH-only) also result in a leaky channel but the activity of compensatory mechanisms mean that SR Ca^{2+} store content is normal. Diagram taken from (Dirksen & Avila 2004).

1.3 STAC adaptor proteins

Three isoforms make up the STAC family of adaptor proteins, so named because they consist of SRC Homology three (SH3) and cysteine-rich domains. Although they have been characterised as 14-3-3 binding proteins (Satoh et al. 2006), little is known about their function. While both STAC and STAC2 are expressed in dorsal root ganglia neurons (Legha et al. 2010), STAC3 is predominantly expressed in skeletal muscle (Bower et al. 2012; Reinholt et al. 2013).

STAC3 and EC couplingStudies of STAC3 mutant zebrafish and KO mouse models have suggested that STAC3 plays a role in EC coupling. In response to depolarisation-evoked Ca^{2+} transients, the mutant zebrafish muscles exhibit reduced contraction and the KO mouse muscles completely fail to contract (Horstick et al. 2013; Nelson et al. 2013). Both models, however, contract normally in response to RyR1 agonists, proving that the RyR1-mediated Ca^{2+} release pathway and contractile apparatus are still functional.

STAC3 has been shown to co-localise with EC coupling proteins, DHPR and RyR1, in the triads (Horstick et al. 2013). Immunoprecipitation data suggests that STAC3 forms a molecular complex with DHPR and RyR1, which both contain numerous SH3 binding sequences in their predicted cytoplasmic portions (Horstick et al. 2013). The relationship between these proteins and STAC3, however, is not well understood. Suggested functions include modulating the channel properties of DHPR and/or RyR1, helping to organise their positioning at triadic junctions between the t-tubules and SR, or regulating the amount of DHPR and/or RyR1 present in the triads by controlling their trafficking or stability (Horstick et al. 2013).

Recent evidence suggests that STAC3 does indeed control the trafficking of the muscle-specific $Ca_V1.1$ subunit of DHPR. When $Ca_V1.1$ was expressed alone in tsA201 cells, which are of non-muscle origin, it was retained intracellularly (Polster et al. 2015). However, when STAC3 was expressed alongside $Ca_V1.1$, the two proteins trafficked together to the plasma membrane (Polster et al. 2015). Moreover, despite the fact that they do not express RyR1, the L-type Ca^{2+} currents in tsA201 cells co-expressing STAC3 and $Ca_V1.1$ were functionally similar to those in myotubes (Polster et al. 2015).

1.3.1 STAC3 in skeletal muscle development

STAC3 was first identified as a nutritionally regulated gene involved in skeletal muscle growth of Atlantic salmon (Bower & Johnston 2010). It has been suggested to be involved in several signalling pathways controlling cell cycle progression, cell migration and cytoskeletal organisation, which are all important in myogenesis (Bower et al. 2012).

In vitro studies have produced conflicting answers as to the exact role of STAC3 in myogenesis. Bower et al. observed an increase in STAC3 expression during differentiation of the C2C12 myogenic cell line and showed that myotubes fail to form when STAC3 is knocked down (Bower et al. 2012). In contrast, Ge et al. showed that STAC3 has an inhibitory role in myoblast differentiation and fusion in both C2C12 and primary mouse embryonic myoblasts (Ge et al. 2014). A study using bovine satellite cells also indicated that STAC3 is a negative regulator of differentiation, although - somewhat contradictorily - its expression increased during the differentiation process (Zhang et al. 2014).

In vivo models do not support the conclusion drawn by Bower et al. that STAC3 is essential for myotube formation; myofibers are clearly formed in STAC3 KD and KO zebrafish, and STAC3 KO mice (Horstick et al., 2013; Nelson et al., 2013; Reinholt et al., 2013). Nevertheless, several skeletal muscle abnormalities were observed in homozygote KO mice, including

centrally-positioned nuclei, fewer yet larger myofibers, and fewer, smaller and less organised myofibrils within the myofibers (Reinholt et al. 2013). Musculoskeletal defects were also reported (Nelson et al. 2013). While the heterozygotes were grossly normal in appearance and behaviour, the homozygotes were born paralysed, with abnormal spinal curvature and wrist drop, and died shortly after birth due to asphyxia (Nelson et al. 2013; Reinholt et al. 2013).

1.3.2 STAC3 and congenital myopathy in humans

Native American Myopathy (NAM) is an autosomal recessive congenital myopathy first reported in the Lumbee Indian people (Bailey & Bloch 1987; Stewart et al. 1988). Clinical features of NAM include congenital onset of muscle weakness, cleft palate, short stature, dysmorphic facial features, scoliosis and MHS. 36% of affected individuals die by the age of 18 (Demetra S Stamm et al. 2008). Homozygosity mapping of 5 Lumbee families with NAM identified a common genetic locus on chromosome 12q13-14 (D S Stamm et al. 2008). It was later shown that human *STAC3* maps to this region, leading to the identification of 5 NAM families sharing the same G>C missense mutation of base pair 1046 in exon 10 of *STAC3* (Horstick et al. 2013). Carriers were heterozygous for this mutation, while affected individuals were homozygous.

The NAM mutation results in a tryptophan (W) to serine (S) substitution at amino acid 284 in the first SH3 domain of STAC3 (Figure 1.9) (Horstick et al. 2013). This W is highly conserved across SH3 domains and is important for binding specificity (Hou et al. 2012). Expression of STAC3 W284S in a STAC3-null zebrafish reduced skeletal muscle Ca^{2+} signals during touch-evoked swimming, suggesting that at least one of the SH3 domains in STAC3 forms important interactions with DHPR and/or RyR1 (Horstick et al. 2013).

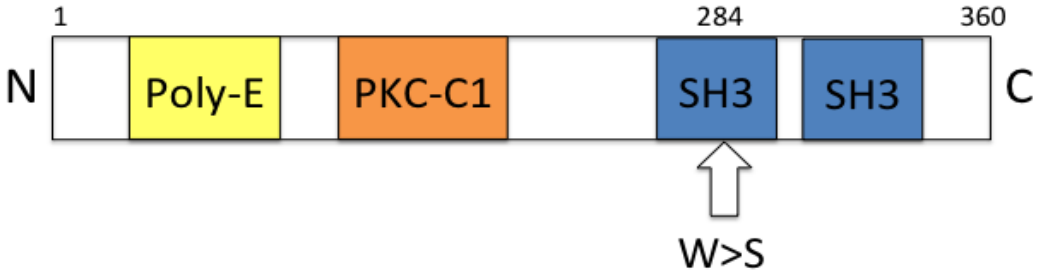

Figure 1.9: NAM mutation affects the first SH3 domain of STAC3

The domain architecture of STAC3 consists of a region containing 11 successive glutamic acid residues (Poly-E), a Protein Kinase C (PKC) C1 domain and two SH3-protein interaction domains (Nelson et al. 2013). Arrow indicates site of W284S NAM mutation. Numbers indicate amino acid position.

1.4 Mitochondrial biology

1.4.1 Mitochondrial Ca^{2+} uptake links energy demand with supply

Mitochondria are able to take up Ca^{2+} via an electrogenic mitochondrial Ca^{2+} uniporter (MCU) found in the inner mitochondrial membrane (IMM). Since three rate-limiting mitochondrial dehydrogenases are Ca^{2+}-sensitive, mitochondrial Ca^{2+} uptake provides a cellular mechanism for coupling stimulatory cytosolic Ca^{2+} signals with oxidative phosphorylation and ATP production. This is particularly important for energy demanding tissues such as skeletal muscle, where EC coupling during contraction is linked to increased mitochondrial metabolism.

The first of these Ca^{2+}-sensitive dehydrogenases is the Pyruvate Dehydrogenase Complex (PDHC), which irreversibly converts the end product of glycolysis, pyruvate, into a high-energy intermediate called acetyl coenzyme A (acetyl co-A). As it represents 'the point of no return' in carbohydrate metabolism, PDHC is subject to stringent regulation; its activity is directly affected by end-product inhibition through increasing ratios of acetyl co-A/pyruvate and $NADH/NAD^{+}$, as well as by reversible phosphorylation of three sites in its E1 subunits (Denton 2009). The

phosphatase responsible for keeping PDH in its active form is activated by Ca^{2+} (Figure 1.10).

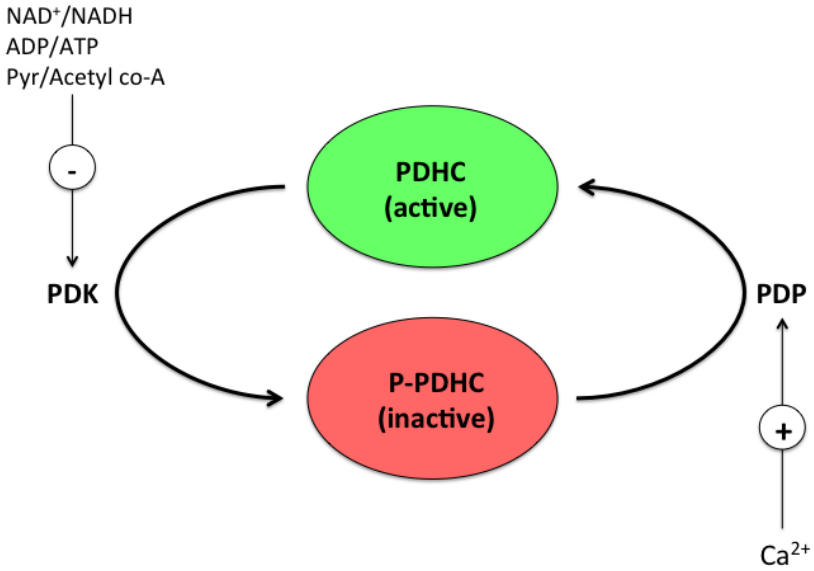

Figure 1.10: Regulation of the PDHC

PDHC is activated by Ca^{2+}-dependent Pyruvate Dehydrogenase Phosphatase (PDP). PDHC is inactivated by the phosphorylating action of Pyruvate Dehydrogenase Kinase (PDK). PDK is inhibited by increases in NAD^+, ADP and pyruvate (pyr).

Acetyl co-A produced by PDHC and fatty acid β-oxidation is subsequently oxidised by a series of enzymes that make up the citric acid cycle (Figure 1.11). Two of these enzymes - α-ketoglutarate dehydrogenase and isocitrate dehydrogenase - are Ca^{2+}-sensitive. Like the PDHC, they are inhibited by increasing ATP/ADP and NADH/NAD^+ ratios (Denton 2009) but the activation mechanism by Ca^{2+} is different. Ca^{2+} apparently binds directly, resulting in variations in the kinetics of both substrates and inhibitory metabolites (Balaban 2009).

Figure removed due to copyright restrictions

Figure 1.11: Glycolysis and the citric acid cycle

Glycolysis in the cytosol produces pyruvate, which is transported across the IMM by the Mitochondrial Pyruvate Carrier (MPC) and converted to acetyl co-A by PDHC in the mitochondrial matrix. Acetyl co-A is then oxidised by a series of enzymes (blue) that make up the citric acid cycle. This provides important reducing agents (pink) for the electron transport chain, as well as small carbon units for making amino acids. Adapted from Figure 1.17.15 within (Berg et al. 2002).

Glycolysis, fatty acid oxidation and the citric acid cycle feed important reducing power in the form of NADH and $FADH_2$, into the electron transport chain of the IMM (Figure 1.12). NADH supplies electrons to Complex I (NADH dehydrogenase), which subsequently shuttles them to the quinone (Q) pool of electron carriers. $FADH_2$ also supplies electrons to the Q pool via Complex II (succinate dehydrogenase), which is the only membrane bound enzyme of the citric acid cycle. Electrons then move from the Q pool to cytochrome c (cyt c) through Complex III (ubiquinone:cyt c oxidoreductase). The final stage of the electron transport chain is the oxidation of reduced cyt c by Complex IV (cyt c oxidase), which passes electrons to O_2 and results in the formation of water.

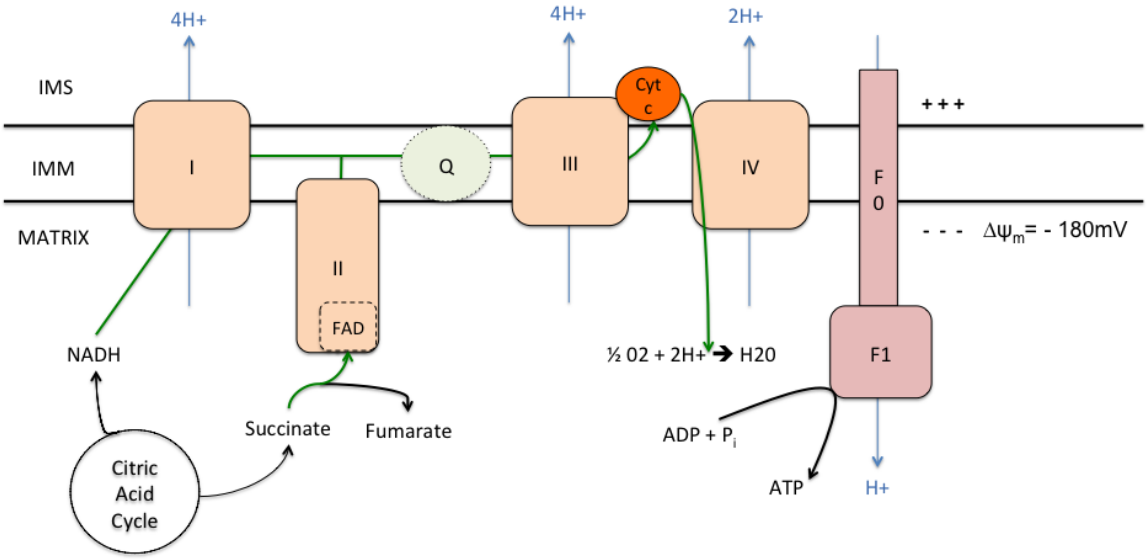

Figure 1.12: Oxidative phosphorylation

Electrons (green arrows) are shuttled though the electron transport chain (orange) before reducing the final electron acceptor, oxygen (O_2). The energy released through this process allows Complex I, III and IV to pump protons (blue arrows) into the intermembrane space (IMS), setting up a proton gradient across the inner mitochondrial membrane (IMM). Protons then preferentially flow back into the matrix through Complex V (pink) and ATP is produced.

As electrons pass down this long chain of donor and acceptor molecules, they fall to successively lower energy states (Berg et al. 2002). Complex I, III and IV use the energy released by this process to pump protons from the matrix into the intermembrane space (IMS). This proton pumping sets up a gradient called the protonmotive force (PMF), which is dictated by a chemical component (ΔpH) and an electrical component ($\Delta\Psi_m$) (Mitchell 1961). In mammalian mitochondria, $\Delta\Psi_m$ (also called mitochondrial membrane potential) is usually around 180mV (negative to the IMS and cytosolic exterior) and ΔpH is approximately 1 unit (the matrix is more alkaline than the IMS and cytosolic exterior) (Skulačev et al. 1981).

The PMF drives ATP production by allowing protons to travel back into the matrix via the ATP synthase (also referred to as Complex V) (Figure 1.12). The ATP synthase essentially converts the energy of this proton movement into the mechanical movement of its transmembrane rotor ring, which in turn rotates a matrix-protruding stalk domain. On the end of the stalk sits a stationary bulbous head domain containing binding sites for ADP and inorganic phosphate (P_i). Rotation of the stalk repeatedly causes conformation changes within the head (Boyer 1993; Abrahams et al. 1994), rapidly driving the formation of 100 ATP molecules a second (Alberts et al. 2002). The number of protons translocated for each synthesised ATP (H^+/ATP ratio) is an important parameter for the mechanism of the enzyme and energy transduction in cells; the H^+/ATP ratio can vary among different species and may be determined by the number of subunits within the catalytic head domain (Petersen et al. 2012).

1.4.2 A history of mitochondrial Ca^{2+} uptake

In the early 1960s, it was shown that rat kidney mitochondria accumulate large amounts of Ca^{2+} in the presence of ATP (Deluca & Engstrom 1961; VASINGTON & MURPHY 1962). Two models were proposed to explain this process: the first being that Ca^{2+} transport is directly and stoichiometrically coupled to the generation of a high energy phosphorylated chemical intermediate by the electron transport chain (Chance 1965), and the second being that there must exist a specific Ca^{2+} carrier which passively transports Ca^{2+} across the membrane in response to a electrochemical gradient generated by electron transport (Lehninger 1970). Although the latter model appeared more feasible at the time, it was not until the general acceptance of Mitchell's chemiosmotic theory that the major driving force for Ca^{2+} accumulation was realised to be the $\Delta\Psi_m$ (Moyle & Mitchell 1977). Thus Ca^{2+} enters the mitochondrial matrix down its electrochemical gradient, which can either be generated by electron flow through the respiratory chain, or if oxidisable substrates are lacking or the respiratory chain is blocked, by the reversal of the ATP synthase (and ATP hydrolysis) (Drago et al. 2011).

After some debate, it was agreed that the unknown mitochondrial Ca^{2+} carrier must function as a uniporter, and not a H^+/Ca^{2+} antiporter, as the net positive charge transported across the mitochondrial membrane during Ca^{2+} import was found to be 2 (Brand et al. 1976). Since there is no counteracting ion exchange, the process of mitochondrial Ca^{2+} import effectively acts like an inward current, and a transient depolarisation of $\Delta\Psi_m$ is witnessed (Duchen 1992; Duchen 2000). In theory, electrochemical equilibrium should be reached if mitochondrial Ca^{2+} accumulation depends solely on $\Delta\Psi_m$. However, according to the Nernst equation, a $\Delta\Psi_m$ value of -180mV would imply about a million fold accumulation of Ca^{2+} in the matrix, which has never been witnessed in cells and does not comply with general physiological concepts (Drago et al. 2011). This paradox was eventually solved upon the discovery of mitochondrial Ca^{2+} efflux pathways, such as via the Na^+/Ca^{2+} exchanger (NCLX) (Palty et al. 2010) and the H^+/Ca^{2+} exchanger. The activity of these antiporters, in addition to matrix calcium buffering

mechanisms, is important in the regulation of $[Ca^{2+}]_m$ and thus the prevention of detrimental mitochondrial Ca^{2+} overload (described in more detail in 1.4.5).

The establishment of fluorescent cytosolic Ca^{2+} indicators during the 1980s seeded doubts regarding the significance of mitochondria in Ca^{2+} homeostasis. The Ca^{2+} concentrations measured under resting (≈ 0.1 μM) or stimulated (1-3μM at the peak) conditions seemed too low for substantial uptake through the low affinity mitochondrial Ca^{2+} uniporter (Rizzuto et al. 2012). Surprisingly, the development of mitochondrial-targeted aequorin (mtAEQ) in the early 1990s showed that the rise in $[Ca^{2+}]_m$ closely follows a stimulated increase in $[Ca^{2+}]_c$ (Rizzuto et al. 1992; Rizzuto et al. 1993). Furthermore, the use of low affinity variants of mtAEQ showed that peak $[Ca^{2+}]_m$ can actually exceed 100μM in some cell types (Montero et al. 2000).

The discrepancy between the amplitude of $[Ca^{2+}]_m$ rises and the low affinity of the mitochondrial Ca^{2+} uniporter was later explained by the observation that mitochondria position themselves close to the Ca^{2+} release channels that evoke the rise in $[Ca^{2+}]_c$ i.e. IP_3Rs in the ER (Rizzuto et al. 1998; Csordás et al. 1999), RyRs in the SR (Szalai et al. 2000) and voltage-operated channels and store-operated channels in the plasma membrane (David et al. 1998; Glitsch et al. 2002). Thus, these microdomains of high $[Ca^{2+}]_c$ are rapidly dissipated by the mitochondria without causing harmful Ca^{2+} overload and/or futile Ca^{2+} cycling across the mitochondrial membrane (Rizzuto et al. 2012). In this way, mitochondria act as high capacity Ca^{2+} buffers, which can influence the spatiotemporal properties of Ca^{2+} signals (Tinel et al. 1999; Boitier et al. 1999) and regulate the activity of Ca^{2+} channels themselves.

Although more and more was being understood about the role of mitochondrial Ca^{2+} uptake in cell physiology, the identity of the mitochondrial Ca^{2+} uniporter eluded scientists for decades. It was not until 2010 that the first molecular component was discovered; Perocchi et al. used a targeted RNA interference (RNAi) screening approach to highlight the necessity of a gene called *CBARA1* (which they renamed as *Mitochondrial Ca^{2+} Uptake 1*

(*MICU1*)) in mitochondrial Ca^{2+} uptake (Perocchi et al. 2010). The presence of two EF hands indicated that MICU1 was a Ca^{2+} sensor, but was unlikely to be part of the pore-forming channel as it was predicted to have only one membrane-spanning domain. It was suggested that its role could be in gating the activity of the bona fide channel, which was actually not far from the truth.

1.4.3 Mitochondrial Ca^{2+} uniporter

The discovery of MICU1 helped reignite the search for the mitochondrial Ca^{2+} uniporter, which came to a remarkable conclusion in 2011 when two papers reporting the identification of the same protein using different approaches were published side by side in Nature (Baughman et al. 2011; De Stefani et al. 2011). Both groups agreed that the Mitochondrial Ca^{2+} Uniporter (MCU) (previously called CCDC109A) was a 40kDa protein ubiquitously expressed in all mammalian tissues and in most eukaryotes, and its down regulation caused considerably reduced mitochondrial Ca^{2+} uptake in living cells stimulated with Ca^{2+} mobilising agonists, permeabilised cells perfused with buffered Ca^{2+} and isolated mitochondria. The presence of two transmembrane domains strongly suggested that the MCU oligomerised in the IMM to form a gated ion channel, which is now believed to exist as a tetramer (Raffaello et al. 2013).

While its overexpression sensitised cells to apoptotic stimuli, silencing of the MCU was originally shown to have little effect on mitochondrial respiration, membrane potential or basic morphology (Baughman et al. 2011; De Stefani et al. 2011), which might seem surprising given its role in satisfying energy demands. A more recent study, however, showed that MCU knockdown (KD) in pancreatic islet cells decreased respiratory chain activity by affecting the expression of its components (Quan et al. 2015).

Interestingly, it is possible to create viable mice in which the MCU is globally knocked out (MCU-KO) (although only when using an outbred strain; MCU deletion is embryonic lethal on the inbred C57BL/6 strain (Murphy et al. 2014)). Despite a complete lack of any capacity for mitochondrial Ca^{2+}

accumulation, the MCU-KO mice showed no change in basal metabolism, mitochondrial morphology or autophagy (Pan et al. 2013). Although MCU-KO mitochondria from these mice lacked evidence for Ca^{2+}-induced mitochondrial permeability transition pore (mPTP) opening, the absence of MCU did not protect against in vitro cell death or ischaemia-reperfusion (IR) injury in the heart (Pan et al. 2013). Besides being slightly smaller than their wild type littermates, the only reported physiological difference was that MCU-KO mice showed reduced maximal skeletal muscle power output, suggesting that altering matrix Ca^{2+} in vivo maybe important in response to exercise (Pan et al. 2013). It is also worth noting that in the MCU-KO mice, mitochondrial Ca^{2+} levels were reduced but were not zero, so alternative entry mechanisms may have been active. One possible mechanism could be the rapid mode of Ca^{2+} uptake (RaM), which has been observed in isolated mitochondria with kinetics much faster than the MCU (Sparagna et al. 1995; Buntinas et al. 2001) but currently has no molecular identity.

Recent work using a conditional, cardiac-specific MCU-KO mouse shows that while it may be indispensible for homeostatic cardiac function, the MCU is required to match metabolic output with contractile demand during stress (Luongo et al. 2015; Kwong et al. 2015). In addition, these mice had reduced activation of the mPTP, which protected them against mitochondrial Ca^{2+} overload during myocardial IR injury (Luongo et al. 2015; Kwong et al. 2015). This suggests that the global KO mouse may have developed adaptations where mPTP opening was prevented but cell death at reperfusion wasn't reduced.

Another recent study has shown that MCU-dependent mitochondrial Ca^{2+} uptake controls muscle size in mice through two major trophic pathways. Skeletal muscle specific silencing of the MCU after birth led to a reduction in PGC1α4 expression and IGF1-Akt/PKB signalling, subsequently triggering atrophy, whereas MCU overexpression had the opposite effect and resulted in hypertrophy (Mammucari et al. 2015). Furthermore, MCU overexpression was protective against denervation-induced atrophy (Mammucari et al. 2015). Interestingly, MCU-overexpressing and MCU-silenced myofibres

showed respective increases and decreases in mitochondrial volume, suggesting that mitochondrial Ca^{2+} homeostasis might have a role in organelle biogenesis and morphology (Mammucari et al. 2015).

1.4.4 Mitochondrial Ca^{2+} uniporter complex

Alongside the channel-forming MCU, a number of regulatory proteins have been identified that form a mitochondrial Ca^{2+} uniporter complex (Figure 1.13). Their exact stoichiometry, role and interaction within the complex are still under scrutiny. Essential MCU Regulator (EMRE) is a 10kDa protein containing a single transmembrane domain, which has been reported to interact with MCU and other regulators MICU1 and MICU2 (Sancak et al. 2013) (Figure 1.13). Solute carrier 25A23 (SLC25A23), a Mg-ATP / P_i carrier in the IMM, also interacts with MCU and MICU1 (Hoffman et al. 2014) (Figure 1.13). KD of either of these proteins has been shown to reduce mitochondrial Ca^{2+} uptake (Sancak et al. 2013; Hoffman et al. 2014).

The MCU paralogue MCUb (previously known as CCDC109b) has been found to act as a dominant negative subunit of the MCU channel (Figure 1.13). The MCU/MCUb ratio appears to vary across different tissues, potentially providing a molecular mechanism to regulate levels of mitochondrial Ca^{2+} uptake (Raffaello et al. 2013).

Mitochondrial Ca^{2+} Uptake Regulator 1 (MCUR1, previously known as CCDC90A) was originally reported to be essential for MCU function, as its KD diminished mitochondrial Ca^{2+} uptake and compromised cellular bioenergetics (Mallilankaraman, Cárdenas, et al. 2012) (Figure 1.13). A subsequent study, however, concluded that MCUR1 is involved in the assembly of Complex IV and does not directly regulate the MCU; the observed reduction in mitochondrial Ca^{2+} uptake was shown to be a consequence of altered $\Delta\Psi_m$ (Paupe et al. 2015). The authors of the first study have recently challenged the observations of Paupe et al. by showing that MCUR1 KD does not affect $\Delta\Psi_m$ or decrease the expression of subunit II of Complex IV (Vais et al. 2015).

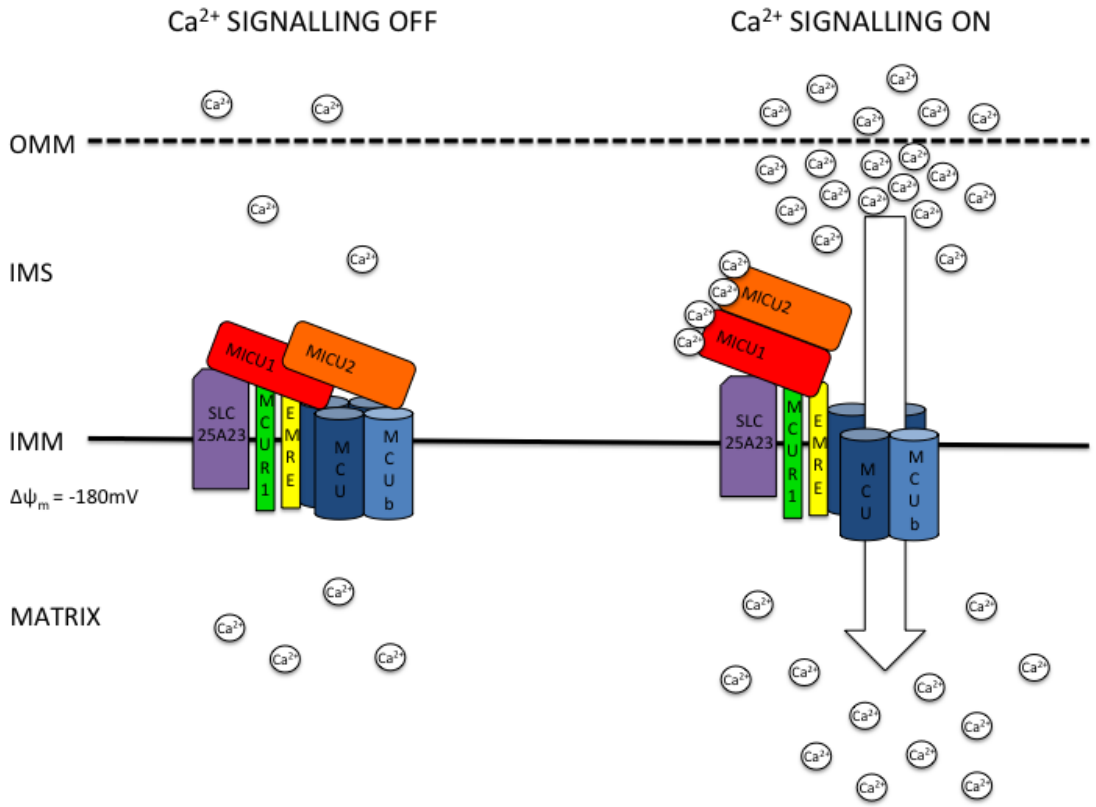

Figure 1.13: Mitochondrial Ca^{2+} uniporter complex

Mitochondrial take up Ca^{2+} through the MCU when a threshold $[Ca^{2+}]_c$ is reached i.e. during a robust intracellular Ca^{2+} signal. The opening of the MCU is controlled by SLC25A23, MCUR1, EMRE, MICU1 and MICU2, which all form part of the uniporter complex.

The most documented regulators of the MCU are the Mitochondrial Ca^{2+} Uptake (MICU) family of proteins. MICU1 was the first identified member of the mitochondrial uniporter complex (even before the MCU itself), and when initially characterised it was described as indispensable for mitochondrial Ca^{2+} uptake (Perocchi et al. 2010). However, subsequent studies have found this not to be the case. It is now widely agreed that MICU1 acts as a gatekeeper of the MCU by setting the threshold concentration of intracellular Ca^{2+} for mitochondrial Ca^{2+} uptake (Mallilankaraman, Doonan, et al. 2012; Csordás et al. 2013).

The precise localisation of MICU1 is still under debate; some studies show that it senses Ca^{2+} on the matrix side of the IMM (Mallilankaraman, Doonan, et al. 2012; Hoffman et al. 2013), while others demonstrate that it resides in

the IMS (Csordás et al. 2013; Hung et al. 2014; Lam et al. 2014; Patron et al. 2014). The significance of MICU1's Ca^{2+} binding EF hands is also not well understood; one model suggests that MICU1 inhibits the MCU in the Ca^{2+}-bound state (Mallilankaraman, Doonan, et al. 2012), while another model involves MICU1 inhibition in the apo-state (Csordás et al. 2013). The latter model also proposes that Ca^{2+} binding to MICU1 is responsible for the cooperative activation of the MCU (Csordás et al. 2013).

Although it is widely recognised that MICU1 is an important regulator of mitochondrial Ca^{2+} uptake, there are still some discrepancies in the literature concerning mitochondrial Ca^{2+} levels at rest and after stimulation in the absence of MICU1. The studies by Mallilankaraman et al. and Patron et al. found that mitochondria were constitutively Ca^{2+} loaded in MICU1 KD cells (Mallilankaraman, Doonan, et al. 2012; Patron et al. 2014), whereas other studies did not observe a change in resting mitochondrial Ca^{2+} levels (Perocchi et al. 2010; Csordás et al. 2013; de la Fuente et al. 2014). Some groups also noted diminished mitochondrial Ca^{2+} uptake in response to agonist-induced ER-mediated Ca^{2+} release (Perocchi et al. 2010; Csordás et al. 2013), which was not observed by Mallilankaraman et al.

While MICU1 KD does not seem to affect $\Delta\Psi_m$ or the resting rate of O_2 consumption, other bioenergetic differences have been reported. Mallilankaraman et al. showed that O_2 consumption was enhanced upon 10μM histamine stimulation in MICU1 KD cells but not in controls. However, upon stimulation with 100μM histamine, a similar increase in O_2 consumption was observed in both control and MICU1 KD cells. The results of Csordas et al. partly agreed with this; compared to controls, MICU1 KD hepatocytes showed increased O_2 consumption in response to low Ca^{2+} (0.2mM CaCl added) but reduced O_2 consumption in response to high Ca^{2+} (10mM CaCl added). Mallilankaraman et al. also showed that pyruvate dehydrogenase was hypophosphorylated (i.e. more active) in MICU1 KD cells, reflecting enhanced Ca^{2+}-dependent activity of pyruvate dehydrogenase phosphatase. In contrast, Perocchi et al. described a reduced increase in NADH

fluorescence in response to 150μM histamine, suggesting that matrix dehydrogenases were less active.

The discovery of MICU2 has added another level of complexity to the regulation of MCU. MICU2 shares 27% sequence identity with MICU1, contains two EF hands and has been shown to form heterodimers with MICU1 in the IMS (Patron et al. 2014). The silencing of MICU1 leads to a loss of MICU2 at the protein level, indicating that MICU2 requires the presence of MICU1 for stability, but not vice versa (Patron et al. 2014; Kamer & Mootha 2014). Biochemical studies also show that association of MICU2 and MCU requires the presence of MICU1 (Kamer & Mootha 2014). These observations therefore complicate interpretation of previous MICU1 KD studies where the expression levels of MICU2 may have been altered.

Work by Patron et al. suggests that MICU2 is actually the gatekeeper of the MCU, and MICU1 instead acts as an activator of the MCU. Whether overexpressing or knocking down MICU1, or knocking down MICU2 alone, the authors saw elevated agonist-induced matrix Ca^{2+} (Patron et al. 2014). This was attributed to a reduction in MICU1-MICU2 heterodimers and the predominance of MICU1-MICU1 homodimers, meaning less MCU inhibition and more activation, respectively. Furthermore, electrophysiological experiments using planar bilayer membranes demonstrated that purified MICU1 failed to have an effect on MCU open probability until Ca^{2+} was raised from 0-1μM (Patron et al. 2014). MICU2, on the other hand, completely inhibited MCU channel activity in the absence of Ca^{2+}.

In contrast, the Mootha group, who originally identified MICU1, believe that MICU1 and MICU2 play nonredundant gatekeeping roles. Both MICU1 and MICU2 KO cells lost a normal threshold for mitochondrial Ca^{2+} uptake, and mutation of either protein's EF hands abolished uptake altogether (Kamer & Mootha 2014). The authors concluded that MICU2 function requires MICU1 but the converse is not true. Somewhat curiously, their data also showed that EF hand mutant MICU1 was able to rescue the gatekeeping function that was compromised in cells lacking MICU2, whereas wild type MICU1 could

not (Kamer & Mootha 2014). Although the authors did not explain this observation, they thought it likely that MICU1 has a different [Ca^{2+}] threshold to MICU2; perhaps the EF hands of each MICU protein have a different functionality in the regulation of MCU.

While MICU1 and MICU2 share similar tissue expression patterns with MCU, MICU3 is found mainly in the nervous system with some expression in skeletal muscle (Plovanich et al. 2013). Very little is known about the functionality of MICU3, but its distinct pattern of expression suggests tissue-specific differences in the regulation of mitochondrial Ca^{2+} uptake.

1.4.5 Mitochondrial Ca^{2+} overload

Though mitochondrial Ca^{2+} accumulation is important for metabolism, too much of it can be detrimental. An excessive increase in $[Ca^{2+}]_m$ can trigger mitochondrial permeability transition, which has been implicated in cell death associated with ischaemia reperfusion injury (Crompton & Andreeva 1993; Halestrap et al. 1997), neurodegenerative disorders (Rao et al. 2014), diabetes (Fujimoto et al. 2010) and various forms of myopathy (Palma et al. 2009). Permeability transition is the formation of a non-specific high conductance channel (the mPTP) in the IMM, which permits unrestricted movement of solutes up to 1.5kDa in size (Haworth & Hunter 1979; Hunter & Haworth 1979). Persistent mPTP opening irreversibly commits cells to death by a series of events: depolarisation of the IMM, which uncouples oxidative phosphorylation and decreases ATP production; matrix swelling and cristae unfolding, and the eventual rupture of the OMM, releasing Ca^{2+} and pro-apoptotic proteins (Rasola & Bernardi 2011). The uncoupling of oxidative phosphorylation not only stops mitochondria from making ATP, but also means that the proton-translocating ATP synthase will run in reverse and cause ATP depletion (Halestrap 2009). Increased $[Ca^{2+}]_m$ alone may not be sufficient to induce mPTP opening; additional factors including oxidative stress, adenine nucleotide depletion, elevated phosphate concentrations and mitochondrial depolarisation are also thought to be critical (Halestrap 2009).

Mitochondrial Ca^{2+} overload could also result in a futile Ca^{2+} cycle (Bhosale et al. 2015). An increase in $[Ca^{2+}]_m$ will inevitably lead to activation of Ca^{2+} efflux pathways – most notably via the mitochondrial Na^+/Ca^{2+} exchanger (NCX). This will raise matrix Na^+, which will in turn activate Na^+/H^+ exchange and allow protons back into the matrix without going through the ATP synthase (Figure 1.14). Hence, the processes that balance Ca^{2+} influx may cause loss of PMF at the expense of ATP production.

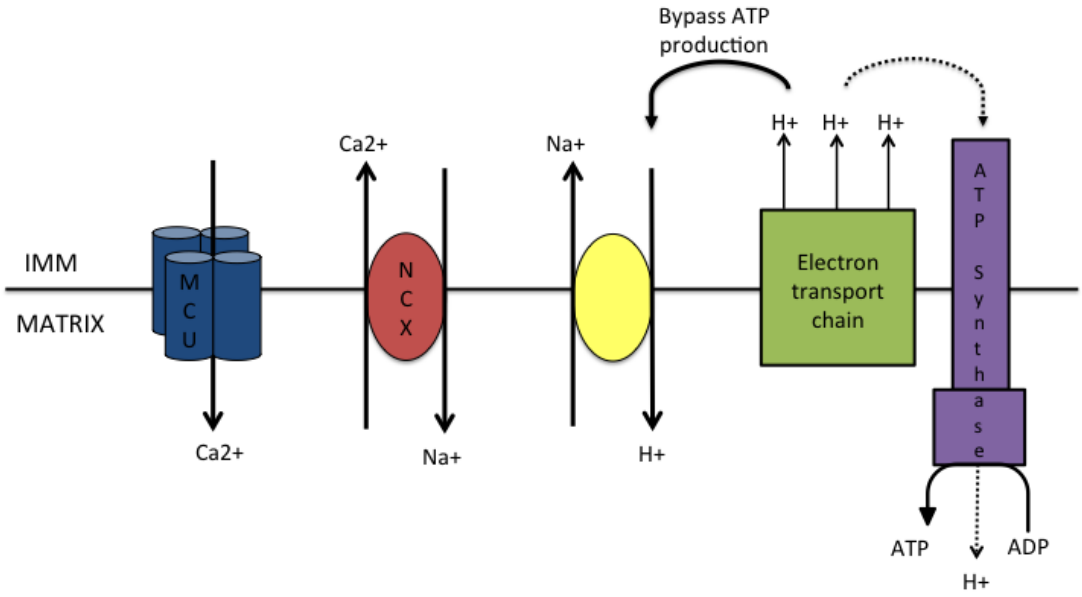

Figure 1.14: Futile Ca^{2+} cycling across the inner mitochondrial membrane

Constitutive mitochondrial Ca^{2+} accumulation carries an energetic cost through the activation of the NCX-mediated efflux pathway.

1.4.6 Mitochondrial ROS production

Reactive Oxygen Species (ROS) are molecules originating from O_2 that can readily oxidise other molecules. Most intracellular ROS are derived from superoxide (O_2^-), which is produced by the one electron reduction of O_2 (Sena & Chandel 2012). O_2^- can be detoxified to the less reactive H_2O_2 by superoxide dismutases, and then to O_2 and H_2O by antioxidants (Brand 2010). However, there are limits to these antioxidant defence systems, and O_2^- that escapes them will damage lipids, proteins and DNA (Brand 2010).

Mitochondria are believed to be major producers of O_2^- as electrons can leak out of the respiratory chain. According to Harman's free radical theory of aging, mitochondrial ROS (mROS) generation is the inevitable outcome of oxidative ATP production and the major cause of macromolecular damage (HARMAN 1972). Some ROS-induced damage may not be repaired thus leading to the gradual decline of the cell's machinery, which has been linked to multiple pathologies including neurodegenerative diseases, diabetes and cancer. On the other hand, mROS production is now understood to be an important signalling pathway in a number of physiological processes, including adaptation to hypoxia, autophagy, immunity, differentiation and longevity (Sena & Chandel 2012).

Seven sites of mROS production have been identified, which are, in order of descending capacity: the ubiquinone binding sites of complex I and complex III, glycerol-3-phosphate dehydrogenase, the flavin in complex I, the electron transferring flavoprotein Q oxidoreductase of fatty acid β-oxidation, and PDH and α-ketoglutarate dehydrogenase (Brand 2010). All of these appear to produce mROS in the matrix, which makes the mtDNA particularly vulnerable to damage. Furthermore, mtDNA lacks the protection conferred by histones characteristic of nuclear DNA and mitochondria have an inadequate repair system for mtDNA mutations (Adhihetty et al. 2003). This means tissues with high oxidation rates e.g. skeletal muscle may be particularly susceptible to an (age or disease related) increase in ROS-induced mtDNA mutations, leading

to dysfunctional OXPHOS and a feed forward cycle of progressive deterioration (Adhihetty et al. 2003).

Skeletal muscle cells experience a high level of ROS generation during contractile activity, though mitochondria may not be the primary source (Barbieri & Sestili 2012). Muscle inactivity also increases mROS production, which could be due to disrupted intracellular Ca^{2+} handling, augmented mitochondrial levels of fatty acid hydroperoxides, impaired protein import into mitochondria or an increase in mitochondrial fission (Powers et al. 2012).

It is sometimes theorised that Ca^{2+} uptake into the mitochondria should result in enhanced mROS generation by the stimulation of the citric acid cycle and OXPHOS, which make the mitochondrion work faster and consume more O_2. In practice, however, it does not appear that simple; observations in the literature vary greatly, which may be due to differences in the specific inhibitors used, the presence of uncouplers, the source and the metabolic state of the mitochondria (Brookes et al. 2004). On the whole it appears that Ca^{2+} reduces mROS from complexes I and III under normal conditions but augments mROS when the complexes are inhibited (Brookes et al. 2004).

1.4.7 Mitochondrial biogenesis

Mitochondria have their own genome, which is maternally inherited and consists of double stranded circular DNA (mtDNA). mtDNA contains 37 genes; 13 of which code for essential subunits of respiratory complexes I,III, IV and V, while the remaining genes encode transfer RNAs and ribosomal RNAs required for translating the respiratory subunit mRNAs in the mitochondrial matrix. The limited coding capacity of mtDNA means that mitochondria are genetically semi-autonomous; they are dependent on the expression of nuclear genes for all their biological functions (Scarpulla 2011).

For mitochondrial biogenesis to occur, the expression of nuclear and mitochondrial genomes must be carefully co-ordinated. Peroxisome Proliferator-Activated Receptor (PPAR)-γ Co-activator 1α (PGC1α) appears

to be at the centre of this co-ordinated response by binding to a large complement of transcription factors and subsequently triggering a complex signalling cascade (Wu et al. 1999). Two such transcription factors are Nuclear Respiratory Factors (NRF) 1 and 2, which contribute to the expression of many genes required for the maintenance and function of the mitochondrial respiratory apparatus (Figure 1.15) (Scarpulla 2008). NRF-1 and NRF-2 directly promote the expression of nuclear-encoded respiratory chain subunits but indirectly promote the expression of mitochondrial-encoded subunits through the activation of proteins involved in mtDNA transcription and replication (Figure 1.15). This includes Mitochondrial Transcription Factor A (TFAM), which is essential for mammalian mitochondrial biogenesis and embryonic development (Larsson et al. 1998).

Figure removed due to copyright restrictions

Figure 1.15: Summary of the nuclear control of mitochondrial functions by NRF-1 and NRF-2

NRFs act on genes encoding cytochrome c (cyt c), the majority of nuclear subunits of respiratory complexes I-V and the rate-limiting heme biosynthetic enzyme, 5-aminolevulinate synthase. In addition, NRFs promote the expression of key components of the mitochondrial transcription and translation machinery, which includes TFAM, a number of mitochondrial ribosomal proteins and tRNA synthetases. NRFs are also involved in the expression of important constituents of

the mitochondrial protein import and assembly machinery. Figure taken from (Scarpulla 2008).

In muscle, PGC1α plays a role in the determination of fibre type. There are two main types of muscle fibre: slow twitch (type I), which are much higher in mitochondrial content and are more dependent on oxidative metabolism, and fast twitch (type II), which contain less mitochondria and rely more on glycolysis (Berchtold et al. 2000). Transgenic mice with a skeletal muscle specific overexpression of PGC1α show a predominance of slow twitch fibres, as well as fatigue resistance and an increased expression of mitochondrial genes (Lin et al. 2002).

Mitochondrial biogenesis can be modulated by a number of physiological conditions. While aging has been linked to reduced biogenesis, there is evidence that calorie restriction can prevent these age-related changes (Picca et al. 2013). In skeletal muscle, mitochondrial biogenesis can be activated by adaptive thermogenesis in response to low temperature or excessive calorific intake (Wu et al. 1999), as well as by chronic contractile activity e.g. endurance training (Hood 2001). Large Ca^{2+} fluxes within the contracting muscle cell activate a number of Ca^{2+}-sensitive enzymes, such as Ca^{2+}-calmodulin kinase II (CaMKII), protein kinase C (PKC) and calcineurin, which are ultimately translocated to the nucleus to affect the activity of transcription factors like PGC1 (Hood 2001). The increased rate of ATP turnover i.e. increased rates of ATP synthesis and degradation during moderate-intensity exercise has also been linked to increased biogenesis through increased AMP-activated Protein Kinase (AMPK) signalling and partial mitochondrial uncoupling (Hood 2001).

1.4.8 Mitochondrial dynamics

Mitochondria are dynamic organelles that undergo constant cycles of morphological remodelling in response to changing intracellular requirements and extracellular cues. The balance of fission and fusion events determines the overall appearance of mitochondria, which reflects the cell's physiological state (Figure 1.16). Typically, dominance of fusion or suppression of fission activity leads to branched, tubular networks; conversely, dominance of fission or suppression of fusion activity causes mitochondria to fragment into short rods or spheres (Jeyaraju et al. 2009). Mitochondrial dynamics and structure can vary between tissues and cell types; for example, mitochondria in cultured primary rat myotubes derived from Flexor Digitorium Brevis (FDB) muscle show an elongated shape like those in adult rat FDB fibres, but because they are not restricted by precisely organised myofilaments, they are more motile and can undergo more fusion events (Eisner et al. 2014).

The mitochondrial fusion machinery includes Mitofusin (Mfn) 1, 2 and optic atrophy 1 (OPA1). OPA1 is a dynamin-related GTPase that is anchored on the IMM and mediates IMM fusion (van der Bliek et al. 2013). OPA1 activity is controlled by OMA1, a protease in the IMM that is rapidly activated by low membrane potential and low ATP levels; this provides a quality control mechanism to prevent damaged mitochondria from re-joining the mitochondrial network (Youle & van der Bliek 2012). Mfn1 and Mfn2 are large GTPases in the outer mitochondrial membrane (OMM) that tether adjacent mitochondria together by forming homo- and hetero-dimers (Chen et al. 2003). Transgenic mice carrying specific deletions of Mfn1 and Mfn2 in skeletal muscle displayed severe mitochondrial dysfunction, compensatory mitochondrial biogenesis and muscle atrophy (Chen et al. 2010). These abnormalities were preceded by a severe loss of mtDNA and a rapid accumulation of mtDNA mutations, highlighting the importance of mitochondrial fusion for mtDNA fidelity and for maintaining respiratory activity in cells carrying a mix of wild type and mutant mtDNA i.e. heteroplasmic cells (Chen et al. 2010) (Figure 1.16). Fusion also allows the mitochondria to act as electrically unified systems, meaning a membrane potential generated in

the cell periphery can be dissipated over a large area and produce ATP in remote parts of the cell (Skulachev 2001) (Figure 1.16). This is particularly important in skeletal muscle, where mitochondrial filaments connect the oxygen-poor mitochondria in the core of the fibre with the oxygen rich peripheral mitochondria (Glancy et al. 2015).

Central to mitochondrial fission events is dynamin-related protein 1 (Drp1 in mammals). Drp1 is a large cytosolic GTPase that self-assembles into a multimeric scission complex at punctate sites on the OMM upon fission initiation (Jeyaraju et al. 2009). A number of OMM proteins including Mitochondrial Fission protein 1 (Fis1) have been reported to be important for Drp1 recruitment during fission (Losón et al. 2013). Drp1-dependent mitochondrial fragmentation is controlled by phosphorylation at two conserved sites, serine 616 (activating) and 637 (inhibiting). S616 is phosphorylated by protein kinase C (PKC) δ, Rock kinase, CDK1/cyclin B or CaMKIα, and S637 is phosphorylated by PKA (van der Bliek et al. 2013). While S616 phosphorylation promotes fission during mitosis, the dephosphorylation of S637 by Ca^{2+}-dependent calcineurin is involved in apoptotic mitochondrial fragmentation (Cribbs & Strack 2007). Opposing effects of PKA and calcineurin on the same site may serve as a switch to translate Ca^{2+} signals of different strength and duration into different mitochondrial morphologies i.e. PKA takes precedence during physiological Ca^{2+} transients but long-lasting Ca^{2+} plateaus will fully activate calcineurin (Cereghetti et al. 2008). Besides mitosis and apoptosis, fission is also important for trafficking mitochondria by cytoskeletal-mediated transport, which is crucial for large extended cells like neurons (Figure 1.16).

Expression of the fission machinery is sufficient to cause muscle wasting in mice by triggering mitochondrial dysfunction, energy stress and AMPK activation (Romanello et al. 2010). AMPK triggers activation of the Forkhead box O (FoxO) class of transcription factors, which drive protein degradation during atrophy via the ubiquitin-proteasome and autophagy-lysosome pathways (Romanello & Sandri 2010). In contrast, inhibition of mitochondrial fission prevents muscle loss during denervation, showing that disruption of

the mitochondrial network is an essential amplifying loop of the muscle atrophy program (Romanello et al. 2010; Romanello & Sandri 2010).

Figure removed due to copyright restrictions

Figure 1.16: Mitochondrial dynamics in various intracellular processes

Mitochondria undergo frequent cycles of fusion and fission that allow the cell to produce several heterogeneous mitochondria or interconnected mitochondrial networks, depending on physiological requirements. Fission is necessary for mitochondrial inheritance during cell division, apoptosis, intracellular mitochondrial distribution and mitochondrial turnover (mitophagy). Fused mitochondrial networks are important for the dissipation of metabolic energy and for the complementation of mtDNA gene products in heteroplasmic cells to counteract decline of respiratory functions in ageing (X and Y represent alleles of different mitochondrial genes). Figure adapted from (Westermann 2010).

1.4.9 Mitochondrial autophagy

Autophagy is a conserved lysosomal degradation pathway that plays an important part in the breakdown and recycling of cellular components, including damaged organelles. The selective autophagic removal of mitochondria is often referred to as mitophagy. This turnover process is co-ordinated with biogenesis and morphological remodelling to maintain the steady state population of mitochondria.

Fission is required to isolate damaged mitochondria so they can be removed by mitophagy. A study of mitochondrial dynamics in fibroblasts showed that 1 in 5 daughter mitochondria is depolarised and eradicated by mitophagy (Twig et al. 2008). In most fission events, one daughter mitochondrion is transiently hyperpolarised while the other is transiently depolarised, suggesting that fission serves as a 'stress test' that can push a daughter mitochondrion to completely depolarise if it is functionally compromised (Youle & van der Bliek 2012).

Two gene products mutated in familial Parkinson's disease, PTEN-induced putative kinase 1 (PINK1) and Parkin, have given an insight into the molecular mechanism for mitophagy. PINK1 kinase is maintained at low levels on healthy mitochondria by constitutive import into the IMM and degradation by a protease called Presenilin-associated Rhomboid-like protein (PARL) (Youle & van der Bliek 2012). When a mitochondrion becomes damaged to the point of uncoupling, protein import to the IMM is prevented and PINK1 accumulates on the OMM (Youle & van der Bliek 2012). The kinase activity of PINK1 then recruits Parkin, an E3 ubiquitin ligase that ubiquitinates OMM proteins and initiates the signal for autophagic removal. However, a recent study has shown that PINK1 is capable of initiating mitophagy in the absence of Parkin, suggesting that PINK1 is actually the signal initiator and Parkin instead acts as a signal amplifier (Lazarou et al. 2015). The PINK1 and Parkin pathway also prevents damaged mitochondria from fusing and contaminating the mitochondrial network through the ubiquitination of Mfn1 and Mfn2 and the phosphorylation

of mitochondrial-motor protein Miro, subsequently marking them for degradation (Youle & van der Bliek 2012).

Upon initiation of the mitophagy signal, a double membrane structure called the isolation membrane (or phagophore) is recruited to the mitochondria and grows around it, essentially engulfing it. The resulting autophagosome then fuses with a lysosome, allowing degradation of the mitochondrial cargo and the inner bilayer of the double membrane, which can be reused or catabolised (Youle & Narendra 2011). A marker for mammalian autophagy is Microtubule-associated Protein 1 Light Chain 3 (MAP1LC3, hereafter referred to as LC3), which exists in two forms: LC3-I, which has a cytosolic distribution and is 18kDa in size, and LC3-II, a lipid-conjugated 16kDa version, which is integrated into the isolation membrane upon autophagy induction (Kabeya et al. 2000).

FoxO3, a transcription factor that is active during muscle atrophy, enhances the transcription of autophagy-related genes including LC3 (Mammucari et al. 2007). The master regulator of mitochondrial biogenesis, PGC1α, is protective against atrophy as it inhibits FoxO3-dependent transcription (Sandri et al. 2006), but its role in autophagy and mitophagy is not well understood. Some atrophy studies have shown increased autophagic flux upon PGC1α overexpression (Vainshtein et al. 2015), whereas others have seen a reduction in autophagy (Cannavino et al. 2014). Nevertheless, there is a clear link between mitochondrial biogenesis and autophagy, and the balance between these two pathways is crucial in determining the quality and quantity of mitochondria.

1.5 What is known about mitochondrial function in core myopathies?

To date, the majority of core myopathy literature has focussed on the study of mouse models, which may reflect the difficulties in accessing patient muscle samples or perhaps practical difficulties in producing muscle cell models from patient fibroblasts. How well these mouse models reflect the human form of CCD varies considerably; for example, the RyR1 T4825I mutation has only been associated with MHS in humans, however, in mouse, it also causes core-like regions (Table 1.2) (Yuen et al. 2011).

While most of these mouse models show characteristic, mitochondria-deficient cores, fibres isolated from the RyR1 T4826I mouse also displayed unusual accumulations of mitochondria in subsarcolemmal areas peripheral to the cores, suggesting that cores are a result of abnormal mitochondrial migration (Yuen et al. 2011). Moreover, fibres from the RyR1 Y522S mouse showed a small but significant increase in the average distance between the mitochondria and the triads (Durham et al. 2008).

Various alterations in mitochondrial morphology have also been reported. Although there were variations from fibre to fibre and area to area, a significant number of FDB fibres from heterozygous RyR1 Y522S mice showed a large number of mitochondria that were abnormally shaped, swollen, and sometimes severely disrupted (Durham et al. 2008). The prevalence of these deteriorations seemed to increase with age. Changes noted included widening and loss of matrix density, an increase in overall size, loss/disorganisation of the internal cristae, disruption of the external membrane and vacuolisation (Durham et al. 2008). Similar abnormalities have been reported in the RyR1 T4826I mouse (Yuen et al. 2011) and the calsequestrin 1 (CASQ1) KO mouse (Paolini et al. 2015), but not in the RyR1 I4895T model (Zvaritch et al. 2007; Zvaritch et al. 2009) (Table 1.2), which will be discussed in more detail in the following chapter.

	RyR1 I4895T	RyR1 Y522S	RyR1 R163C	RyR1 T4826I	CASQ1 KO
Human disease	CCD	CCD & MHS	CCD & MHS	MHS	None*
Viability	HOM die at birth HET viable	HOM die ED17 HET viable	HOM die ED17/18 HET viable	HOM & HET viable	Viable
MHS	-	+	+	+	+
Core-like regions	+	+	-	+	+
Nemaline rods	+	-	-	-	-
Myofibrillar disorganisation	+	+	Unknown	+	+
Mitochondrial swelling / degeneration	-	+	Unknown	+	+
Location in RyR1	C terminal	N terminal	N terminal	C terminal	NA
RyR1 phenotype	EC uncoupled	Leaky	Leaky	Leaky	Leaky
References	(Zvaritch et al. 2007; Zvaritch et al. 2009; Boncompagni et al. 2010; Loy et al. 2011)	(Chelu et al. 2006; Durham et al. 2008; Boncompagni et al. 2009)	(Yang et al. 2006; Giulivi et al. 2011)	(Yuen et al. 2011; Barrientos et al. 2012)	(Paolini et al. 2007; Dainese et al. 2009; Paolini et al. 2015)

Table 1.2: Summary of available core myopathy mouse models

*CCD= central core disease, MHS= malignant hyperthermia susceptibility, HOM= homozygote, HET= heterozygote, ED= embryonic day, NA= not applicable, * though the N244G mutation in CASQ1 causes a vacuolar myopathy (Rossi et al. 2014)*

A study using the CASQ1 KO mouse has suggested that mitochondrial biogenesis may be affected in core myopathies. The authors reported a two-fold increase in PGC1α expression in EDL muscle homogenates from adult CASQ1 KO mice, which was consistent with increased mitochondrial volume and increased oxidative fibre content (Paolini et al. 2015). This PGC1α upregulation could be linked to Ca^{2+} deregulation, as free myoplasmic Ca^{2+} levels were increased at physiological temperature in CASQ1 KO fibres (Dainese et al. 2009).

Although their mutations are more closely associated with MHS in humans, the RyR1 Y522S and CASQ1 KO mice present evidence that increased oxidative stress contributes to mitochondrial damage and possibly core development. Both mutations result in elevated resting myoplasmic Ca^{2+}, which increases mitochondrial ROS and Reactive Nitrogen Species (RNS) production (Durham et al. 2008; Paolini et al. 2015). This then creates a feed-forward mechanism where the ROS and RNS cause activity-enhancing modifications to RyR1, leading to further SR Ca^{2+} leak and enhanced Ca^{2+} release in response to heat stress (Durham et al. 2008). In support of this, treatment with potent antioxidant, N-acetylcysteine, reduced oxidative stress and improved muscle function in both models (Durham et al. 2008; Paolini et al. 2015). In agreement with these murine studies, cultured myotubes from patients with RYR1-related myopathies have been shown to exhibit oxidative stress (Dowling et al. 2012). This was attributed to increased mitochondrial ROS production and could also be treated with N-acetylcysteine (Dowling et al. 2012).

1.6 Research hypothesis

The ‘health’ of muscle mitochondria is crucial for maintaining normal muscle function and to provide the energy for force generation, as emphasized by the predominantly muscle phenotype of patients with mitochondrial DNA mutations. As has been described in earlier sections of this thesis, mitochondrial biology and intracellular Ca^{2+} homeostasis have an intricate relationship. Ca^{2+} plays a central role in the modulation of mitochondrial function through several pathways that ultimately converge to promote oxidative phosphorylation. On the other hand, excessive mitochondrial Ca^{2+} uptake can cause mitochondrial damage and potentially cell death. This delicate balancing act means it is not surprising that an alteration in intracellular Ca^{2+} signalling can result in a mitochondrial phenotype. In spite of this, the literature has somewhat overlooked the possibility that disruptions to intracellular Ca^{2+} homeostasis may cause mitochondrial dysfunction and altered bioenergetics, which could contribute to the muscle weakness observed in core myopathy patients. Therefore my research hypothesis is as follows:

Mitochondria are contributing to core myopathy pathology by suffering Ca^{2+}-related dysfunction.

I will test this hypothesis by characterising mitochondrial function in three core myopathy models with mutations in RYR1, STAC3 and MICU1, all of which play a role in muscle Ca^{2+} homeostasis (Figure 1.17). More specifically, I aim to complete the following objectives in each model:

1. Characterise intracellular Ca^{2+} homeostasis, which is known to be disrupted in core myopathies
2. Examine possible mitochondrial defects, including alterations in bioenergetics and mitochondrial distribution/morphology
3. Compare my results to previous literature
4. Discuss and evaluate my results in line with the above research hypothesis

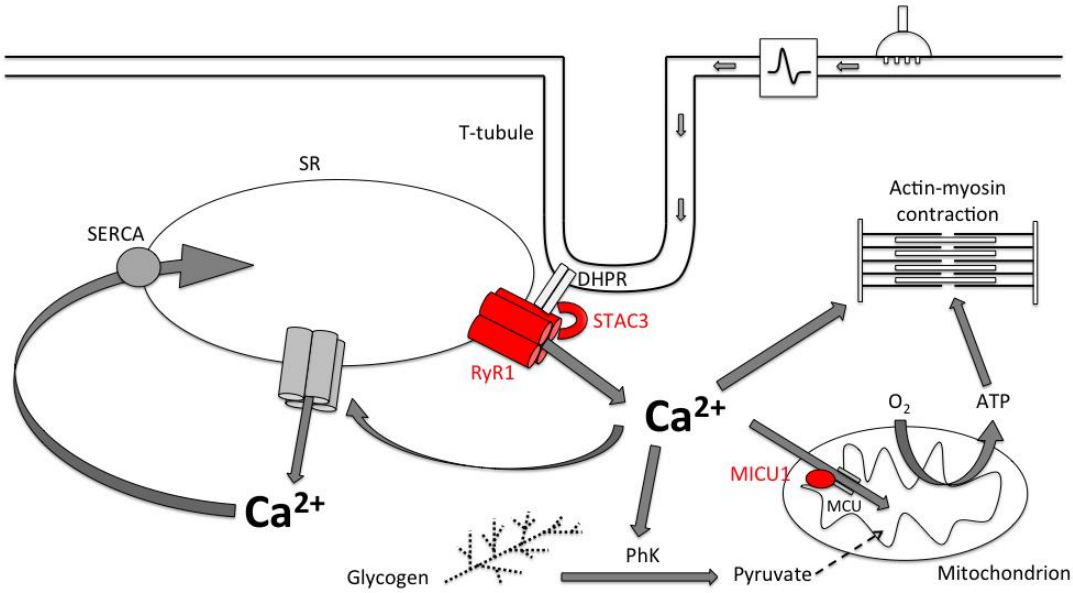

Figure 1.17: Proteins involved in muscle Ca^{2+} homeostasis

Mutations in RyR1, STAC3 and MICU1 proteins (red) result in a core myopathy phenotype. I will answer my research hypothesis by characterising mitochondrial function in three models with mutations in these proteins.

Chapter 2 Assessing mitochondrial function in a new RyR1 I4895T mouse model

2.1 Introduction

2.1.1 I4898T mutation in RYR1

The I4898T mutation has been associated with the dominant inheritance of CCD in at least seven unrelated families around the world (Robinson et al. 2006). The degree of severity within each family varies from mild to severe, but a lethal de novo case of the mutation has also been reported in newborn twins (Hernandez-Lain et al. 2011). In addition to central cores, muscle biopsies from these twins showed nemaline rods, which have never been seen in I4898T-affected humans before.

The I4898T mutation is situated in the C-terminal 'hotspot' region of RyR1 (see Introduction 1.2.3), or more specifically, the transmembrane/luminal domain (or selectivity filter) (Lynch et al. 1999). Whether this mutation resulted in a 'leaky' or 'EC-uncoupled' RyR1 channel was not clear from early in vitro studies. The group that identified the first I4898T-affected family showed that transient expression of both normal and mutant channels (mimicking the patient heterozygosity) in HEK cells resulted in increased resting $[Ca^{2+}]_c$ through RyR1 leak, which may have been due to a reduction in the Ca^{2+} concentration required for channel activation (Lynch et al. 1999). However similar experiments in dyspedic (RyR1 KO) mouse myotubes by Avila et al. did not show a change in resting or luminal Ca^{2+} concentrations; instead the authors observed a reduction in electrically-evoked Ca^{2+} transients, which may have been due to an uncoupling of sarcolemma excitation from SR Ca^{2+} release (Avila et al. 2001).

2.1.2 RyR1 I4895T knock-in mouse

The generation of a knock-in mouse line carrying the analogous murine I4895T mutation in RyR1 provided a valuable in vivo insight into the

pathogenesis caused by this *RYR1* mutation. Homozygous mice are born with skeletal muscle paralysis, are unable to breathe, and die perinatally (Zvaritch et al. 2007). Analysis of the homozygote foetuses showed abnormal myogenesis and skeletal and cardiovascular development, suggesting that RyR1-mediated Ca^{2+} signalling is important in embryogenesis. Although muscle triad architecture and channel assembly was deemed normal in the mice, primary mutant myotubes were completely unresponsive to electrical and drug stimulation. Zvaritch et al. interpreted this as a defect in Ca^{2+} permeation/gating rather than a leaky channel, since resting $[Ca^{2+}]_c$ and SR Ca^{2+} content were no different to that in wild type (WT) myotubes.

Although heterozygous RyR1 I4895T mice also undergo neonatal respiratory stress, they recover from this and go on to exhibit a slowly progressive myopathy with varying degrees of severity (Zvaritch et al. 2009). Phenotypic features include impaired locomotion, dorsal kyphosis and in some mice, complete hind limb paralysis. Grip strength and hanging tasks showed that 4-5 month old adult heterozygotes have a significant reduction in in vivo muscle strength (Loy et al. 2011). Single skeletal muscle fibres from these mice exhibited a significant reduction in the magnitude and rate of cytosolic Ca^{2+} signals during electrically evoked EC coupling and 4-chloro-m-cresol induced RyR1 activation, but did not have altered SR store content or RyR1 channel sensitivity thus agreeing with Zvaritch's diminished Ca^{2+} permeation theory (Loy et al. 2011). It is now widely agreed that the I4895T mutation causes RyR1 to become 'EC uncoupled', while other mutations result in an over-sensitive, 'leaky' channel (see Table 2.1, Introduction 1.5).

It has been shown that heterozygous RyR1 I4895T myofibres undergo an age-dependent transition from small, compacted focal areas resembling minicores in younger mice, to cores and nemaline rods in adult and aged animals (Zvaritch et al. 2009). In areas of structural disorganisation, the mitochondria were displaced but did not show signs of swelling or degeneration as seen in other core myopathy mouse models (Table 2.1, Introduction 1.5). In the RyR1 I4895T and Y522S models, spatial inhomogeneity in local Ca^{2+} releases was proposed as a possible

mechanism for the formation of localised alterations in muscle structure (Zvaritch et al. 2009; Boncompagni et al. 2009). Functional heterogeneity in WT:mutant RyR tetramers could be the cause of such nonuniform Ca^{2+} release, which would result in shearing forces and possible disruption to sarcotubular and mitochondrial systems over time (Zvaritch et al. 2009).

Genetic background appears to have a strong influence over the disease phenotype of the RyR1 I4895T knockin mouse. When the mutation was bred on a congenic 129S2/SvPasCrl background, it resulted in a variable but severe phenotype; 80% of HET mice exhibited some degree of motor dysfunction by 10 months old and 14% suffered complete hind limb paralysis at 12 months (Zvaritch et al. 2009). However, RyR1 I4895T mice on a mixed 129S6/SvEvTac and 129S2/SvPasCrl background had a much milder disease phenotype (Boncompagni et al. 2010). The mixed sub-line showed mild structural alterations with relatively little mitochondrial involvement, whereas widespread areas of mitochondria-deficient contracture (localised regions of severe sarcomere shortening) were a prominent feature of the congenic sub-line.

A study of MmD patients has reported a correlation between variations in clinical phenotype and RyR1 expression levels, demonstrating that epigenetic allele silencing can play an important role in disease presentation (Zhou et al. 2006; Zhou et al. 2007). However, it is unlikely that this applies to the I4895T mouse models, as the same study also showed that the RYR1 mouse orthologue does not undergo genetic imprinting. In agreement with this, Zvaritch et al. found that WT and mutant alleles were expressed at similar levels in their congenic colony (Zvaritch et al. 2009). Nevertheless, other factors such as differences in epigenetic modulators or stability of the mutant protein might explain the phenotypic variation between I4895T mouse strains (Boncompagni et al. 2010).

2.1.3 Aims

The degree of mitochondrial involvement varies considerably between different core myopathy mouse models (see Introduction 1.5) and even between sub-lines of mice carrying the same RyR1 mutation. The Duchen laboratory has created a new sub-line of RyR1 I4895T mice on a mixed 129S2/SvPasCrl and C57BL/6J genetic background. In line with the objectives set out in 1.6, the aim of this chapter is to characterise the phenotype of this new sub-line by assessing Ca^{2+} homeostasis and mitochondrial function in a primary muscle cell model.

2.2 Methods

2.2.1 Animal handling

RyR1 I4895T knock-in mice on a 129S2/SvPasCrl background were kindly provided by the Hamilton laboratory, Texas, USA. These founder mice were rederived using C57BL/6J mice as this strain is reliable for breeding. This resulted in a new sub-line with a mixed genetic background (approximately 50% 129S2/SvPasCrl and 50% C57BL/6J after rederivation). Since homozygotes have a perinatal lethal phenotype (Zvaritch et al. 2007), heterozygotes (HET) were crossed with wild type (WT) littermates or C57BL/6J mice (Charles River) to maintain the colony. At least five such crosses had occurred before my experiments. Ear snips from adult mice and tail snips from sacrificed neonates were retained for genotyping.

2.2.2 Animal genotyping

DNA was extracted from tissue samples using the Extract-N-Amp kit (Sigma) and PCR was used to amplify the fragment covering the mutation site. Forward and reverse primers were 5'-GGTCTTCCTGTCTCAATAACCCGATCTAGAAAC-3' and 5'-GATGGAGAAACCAAAGCTCAGAGAGACCAC-3' respectively. PCR reactions were made up to 25µL and contained the following: 1X Green GoTaq® reaction buffer (ProMega), 0.2mM PCR nucleotide mix (ProMega), 3mM $MgCl_2$ (ProMega), 1µM forward and 1µM reverse primers (Sigma), 1.25 units of GoTaq® Hot Start polymerase (ProMega) and 1µL DNA template. PCR was performed in an Eppendorf MasterCycler using the cycling profile: 95°C for 2mins, followed by 35 cycles at 95°C for 30secs, 60°C for 30secs, 72°C for 1min. 2.5 units of Age I (NEB) was added to each amplified sample and incubated at 37°C for 2 hrs. 5µL of 1kB DNA marker (NEB) and 10µL of each restriction digest was loaded onto a 3% agarose gel (made with 1X TAE buffer and 0.5µg/mL ethidium bromide) and electrophoresis was carried out at 75V until the dye line was approximately 70% of the way down the gel. DNA was then visualised under UV light on a transilluminator (Figure 2.1).

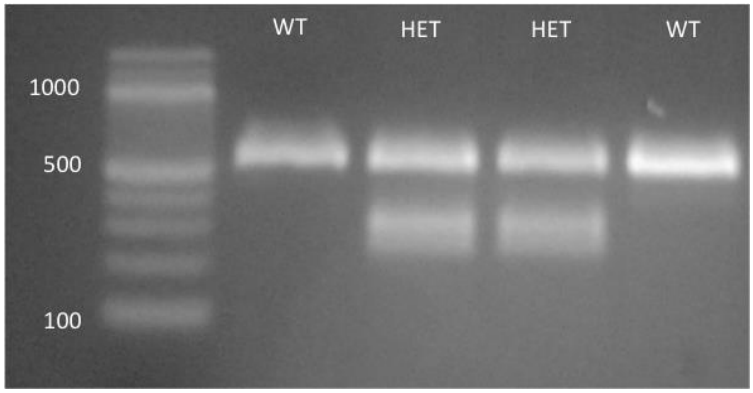

Figure 2.1: Example of genotyping restriction digest

Since the inserted mutation site also contains an Age I target sequence, only samples containing the mutated allele undergo Age I digestion. Therefore HET mice show two lower 'cut' bands in addition to the 'uncut' WT band. With hindsight, a negative (no DNA template) control should have been included in each PCR experiment to check for extraneous DNA contamination.

2.2.3 Chemicals

All chemicals were purchased from Sigma unless otherwise stated.

2.2.4 Cell culture

Primary myotube cultures were produced from postnatal (P) day P2-P7 WT and HET littermates. As genotype was unknown at time of dissection, each mouse and its subsequent myoblast population were processed separately. Pups were sacrificed by cervical dislocation and the hind limbs dissected. Muscles were minced finely and shaken for 1 hr at 37°C in a digestion mix containing 1mg/mL collagenase (from *Clostridium histolyticum*, Sigma) and 3.5mg/mL dispase (Invitrogen) diluted in Iscove's Modified Dulbecco's Medium (IMDM) containing Glutamax (cat. no. 31980030, Invitrogen). Centrifugation and filtration were used to remove large debris, and then the cell suspension was pre-plated for 3-4 hrs to remove fibroblasts and purify the myoblast population. During this time, 22mm glass coverslips, 35mm imaging dishes (FluoroDish, WPI) or 96 well imaging plates (BD Biosciences) were coated with Matrigel (BD Biosciences, diluted 1:100 in ice-cold IMDM) for at least 1 hr at RT before washing with IMDM. After 3-4 hrs pre-plating,

myoblasts were centrifuged and resuspended in proliferation media consisting of IMDM, 20% Fetal Bovine Serum (FBS) (Invitrogen), 1% chicken embryo extract (MP Biomedicals), and 0.05mg/mL gentamycin (Sigma), and plated on the Matrigel-coated cultureware. When myoblasts started to spontaneously fuse after 3-4 days, the proliferation media was removed and concentrated Matrigel (diluted 1:2 in ice-cold IMDM) was carefully pipetted on top of the cells and left to set for 30 mins at 37°C. Differentiation media consisting of IMDM, 2% horse serum (HS) (Invitrogen), 100ng/mL rat agrin (R&D Systems) and 0.05mg/mL gentamycin was then added to the Matrigel-coated cells. Myotubes were imaged at days 8-10 of agrin differentiation.

2.2.5 Myofiber isolation

6-7 month old female WT and HET mice were sacrificed by CO_2 inhalation and FDB muscles were dissected. This muscle was selected because its small size was optimal for tituration (see below). FDBs were digested for 1.5 hrs at 37°C in 2mg/mL collagenase type I (Sigma) before being transferred to Dulbecco's Modified Eagle's Medium (DMEM) containing Glutamax (cat. no. 10569010, Invitrogen), 10% FBS, 1% PS and left at 37°C 5% CO_2 for at least 15mins. Individual myofibers were released by titurating the muscles with a range of fire-polished glass bore pipettes decreasing in diameter. Tituration steps were carried out directly on Matrigel (diluted 1:10 in ice-cold DMEM) coated 35mm imaging dishes and 24-well imaging plates (iBidi). Plating medium consisted of DMEM, 20% controlled serum replacement (Sigma), 1% HS and 1% PS. Myofibers were imaged within 24 hrs of plating.

2.2.6 Immunofluorescence

Primary mouse myotubes were fixed in PBS/3.7% paraformaldehyde for 15 mins, washed with PBS, permeabilised with PBS/0.25% Triton X-100 for 10 mins and blocked in PBS containing 3% BSA and 10% donkey serum (Sigma) for 30 mins at room temperature (RT). Primary anti-RyR1 antibody (mouse IgG1, Abcam) was used at 1:200 dilution in PBS/0.25% Triton X-100/3% BSA for 2 hrs RT. Secondary anti-mouse AlexaFluor647 antibody

(donkey, Invitrogen) was used at 1:500 dilution in PBS/0.25% Triton X-100/3% BSA for 30 mins RT. Cells were washed with PBS and incubated with 2µg/mL Hoechst stain for 10 mins RT. Cells were then washed with PBS, covered in Fluoromount (Sigma) and left to air dry before imaging on a Zeiss 700 CLSM. A secondary control (no primary antibody incubation) was used to establish acquisition settings so that background staining was excluded.

ImageJ (NIH) was used for image analysis. Differentiated myotubes were identified as cells containing more than one nucleus (using the Hoechst image). Myotubes with a stripy RyR1 patterning as in (Falcone et al. 2014) were scored as 'striated'.

2.2.7 Cytosolic Ca^{2+} imaging

Myotubes and myofibres, cultured in 96 well and 24 well imaging plates, respectively, were loaded with recording buffer (RB) (150mM NaCl, 4.25mM KCl, 4mM $NaHCO_3$, 1.25mM NaH_2PO_4, 1.2mM $MgCl_2$, 1.2mM $CaCl_2$, 10mM D-glucose, 10mM HEPES pH7.4) containing 5µM fura-2 AM (Molecular Probes) for 40 mins at 37°C. 0.002% pluronic acid was also included in the loading buffer to aid solubilisation and loading of the AM ester. Cells were washed with RB before being imaged on an Olympus IX71 inverted epifluorescence microscope using a 20x objective. Stock concentrations of caffeine and 4-chloro-m-cresol were made up in RB. Potassium chloride (KCl) solutions were made up so the final total ionic strength remained as 154.25mM ($[K^+]$ + $[Na^+]$). Fura-2 was sequentially excited at 340nm and 380nm, while emission was measured at 510nm. Images were acquired using a CCD camera (Hamamatsu Corporation) and were recorded and analysed in the MetaFluor 7.8 software (Universal Imaging).

Background was subtracted from both 340nm and 380nm images and regions of interest (ROIs) were drawn around individual myotubes and myofibres. Myotubes were defined as cells with more than one nucleus. Damaged or contracted myofibres were excluded from analysis. The ratio of

the background-corrected fluorescence intensities detected at 510nm (hereafter referred to as fura-2 ratio) was used to illustrate cytosolic Ca^{2+} levels in each cell. By using the ratio of fluorescence intensities produced by excitation at two wavelengths, factors such as uneven dye loading and photobleaching are minimised as they should affect both measurements to a similar extent. ∆fura-2 was calculated as the difference between the average resting fura-2 ratio and the peak ratio following stimulation. Only 'responding' cells i.e. that showed a ≥10% increase in fura-2 ratio following stimulation, were analysed. Data originating from the same mouse was pooled together to give an average value, which was then used in statistical analysis.

2.2.8 Measurements of resting $\Delta\Psi_m$

Isolated myofibres were equilibrated with RB containing 25nM tetramethylrhodamine methyl ester (TMRM) for 15 mins at 37°C. Confocal z stacks were then acquired on a Zeiss 510 UV-VIS CLSM using a 40x oil objective. RB containing only 25nM TMRM was present throughout imaging. Fluorescence was excited at 543nm and measured at >560nm.

ImageJ was used for image analysis. Damaged or contracted myofibres were excluded from analysis. ROIs were drawn around individual myofibres and images were thresholded to quantify the mean of mitochondria-localised signal intensities within each ROI. Maximum intensity projections were used for quantification to avoid bias in the focal plane. Identical acquisition settings and threshold values were used in repeat experiments.

2.2.9 Resting NADH measurements

Isolated myofibres were imaged as a z stack using a Zeiss 510 UV-VIS CLSM with a 40x oil objective. Fluorescence was excited using the 351nm line of an argon laser and was measured between 435-485nm. The pinhole was kept wide open to maximise NADH signal.

ImageJ was used for image analysis. Damaged or contracted myofibres were excluded from analysis. ROIs were drawn around individual myofibres and images were thresholded to quantify the mean of mitochondria-localised signal intensities within each ROI. Maximum intensity projections were used for quantification to avoid bias in the focal plane. Identical acquisition settings and threshold values were used in repeat experiments.

2.2.10 Respirometry of permeabilised muscle fibres

5 month old female WT and HET mice were sacrificed by CO_2 inhalation. EDL and soleus muscles were dissected and put in ice-cold Biopsy Preservation Solution (BIOPS) (2.77mM CaK_2EGTA, 7.23mM K_2EGTA, 5.7mM Na_2ATP, 6.56mM $MgCl_2.6H_2O$, 20mM taurine, 15mM Na_2Phospho-creatine, 20mM imidazole, 0.5mM dithiothreitol, 50mM MES, pH7.1). Muscles and fibre bundles were kept on ice at all times prior to respirometry measurement. After removing connective tissue and tendon, muscles were gently separated into 6-8 fibre bundles of roughly equal size using a pair of needles. To maximise muscle surface area, individual fibres within each bundle were teased apart with needles. Fibre bundles were permeabilised in ice-cold BIOPS containing 25µg/mL saponin for 30 mins with gentle agitation, before being washed with ice-cold Mitochondrial Respiration medium 5 (Miro5) (0.5mM EGTA, 3mM $MgCl_2.6H_2O$, 60mM K-lactobionate, 20mM taurine, 10mM KH_2PO_4, 20mM HEPES, 110mM sucrose, 1g/L BSA, pH7.1) for 10 mins with gentle agitation. 3 bundles of roughly equal size were transferred to a Miro5-filled chamber of a high-resolution Oxygraph (Oroboros Oxygraph-2K) maintained at 37°C. The chambers were then hyper-oxygenated to at least 500µM [O_2] by injecting a 95% O_2 / 5% CO_2 medical gas mixture (Figure 2.2). Complex I substrates, 10mM glutamate and 2.5mM malate, were added to measure the leak state (non-phosphorylating resting state of intrinsic uncoupled respiration), followed by 2.5mM ADP to observe the active state. 10µM cyt c was used to test the intactness of the OMM (Pesta & Gnaiger 2012). 10mM succinate was then added to assess respiration in the presence of both complex I & II substrates. Maximal oxidative capacity was determined in the presence of 0.25µM

FCCP, complex II-driven respiration measured in the presence of 0.5μM rotenone and non-mitochondrial (background) O_2 consumption determined in the presence of 2.5μM Antimycin A.

As the instrument contained two measuring chambers, WT and HET samples were assessed simultaneously in one experiment. To minimise any possible variation between the chambers, WT and HET samples swapped chambers in repeat experiments.

At the end of each experiment, muscle bundles were removed from the chambers and frozen at -80°C. The bundles were homogenised using a hand-operated Kontes Pellet Pestles grinder (Kimble) and lysed in RIPA buffer (150mM NaCl, 0.5% sodium deoxycholic acid, 0.1% SDS, 1% Triton X-100, 50mM Tris pH8, 1mM PMSF) for 30 mins on ice. Samples were subsequently centrifuged at 16,000g at 4°C and protein concentrations determined using Pierce BCA assay (Thermo Scientific). These values were then input into DatLab5 (Oroboros Oxygraph-2K) to normalise O_2 flux to total protein content of each sample. Average O_2 consumption rates were calculated by manually selecting a region where the signal was relatively stable (Figure 2.2). These rates were then corrected for background/non-mitochondrial respiration by deducting the value for average O_2 flux in the presence of Antimycin A.

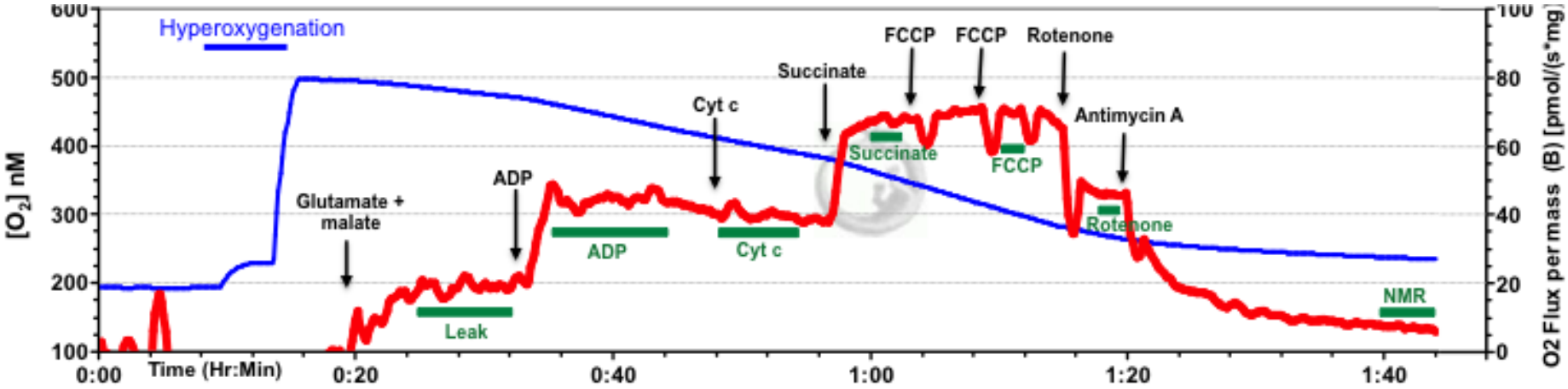

Figure 2.2: Example of O_2 consumption measurements of permeabilised muscle fibres

Blue line indicates O_2 concentration inside the chamber, while the red line shows O_2 flux per mg protein i.e. O_2 consumption normalised to total protein content. After inserting the fibre bundles, the chambers were hyperoxygenated and glutamate and malate were added to kick-start mitochondrial respiration. ADP, cyt c, succinate, FCCP (titrated), and rotenone were added in succession to observe transition between different respiratory states. A final addition of Antimycin A was used to measure non-mitochondrial respiration (NMR). Green bars indicate regions over which average respiratory state values were calculated.

2.2.11 Western blotting

6-8 month old female WT and HET mice were sacrificed by CO_2 inhalation and dissected of EDL and soleus muscles, which were then frozen at -80°C. These muscles were chosen to see if the pathological impact of the I4895T mutation varies in different muscle types (in human CCD type I fibres are predominantly affected (Jungbluth 2007a)). The muscles were homogenised, lysed and had total protein concentration determined as above (section 2.2.10). 25µg of protein was heated to 55°C for 5 mins in NuPAGE 4X LDS sample buffer (Invitrogen) containing 5% β-mercapethanol. Proteins were separated using 4-12% NuPAGE Bis-Tris gels (Invitrogen) with MOPS running buffer (Invitrogen) and transferred onto Immobilon PVDF membranes (Millipore) using NuPAGE transfer buffer (Invitrogen) supplemented with 20% methanol. Membranes were washed with PBS-T and blocked with 5% dried skimmed milk in PBS-T for 1 hour at RT, before being incubated with primary antibody solution overnight at 4°C. Following 3 x 10 min washes in PBS-T, membranes were incubated with secondary antibody solution for 1-1.5 hrs at RT. After 3 x 5 min washes in PBS-T, the membranes were developed using Amersham ECL reagent (GE Healthcare) and imaged with a ChemiDoc system (BioRad). Densitometry analysis was carried out using ImageJ.

Primary antibodies used were total OXPHOS rodent antibody cocktail (mouse, MitoSciences; 1:1000), anti-TFAM (rabbit, Abcam; 1:1000) and anti-GAPDH (rabbit, Sigma; 1:5000). The total OXPHOS antibody cocktail contains antibodies against the following complex subunits: CI subunit NDUFB8, CII-30kDa, CIII-core protein 2, CIV subunit I and CV alpha subunit. Secondary antibodies used were goat anti-mouse and goat anti-rabbit HRP conjugated IgGs (both from Thermo Scientific and diluted 1:4000).

2.2.12 Statistics

Values are presented as mean ± standard error. Statistical analysis was performed using Prism 6 (GraphPad). Unpaired two-tailed t-tests were applied to test significance to a P value of 0.05. Significant differences are

indicated with asterisks (* if $P<0.05$, ** if $P<0.01$, *** if $P<0.001$). N indicates number of mice used for statistics (unless otherwise stated).

2.3 Results

2.3.1 Agrin-treated primary mouse myotubes do not exhibit striated triads but are a functional muscle model

Skeletal muscle has an intricate striated architecture in vivo, which has been replicated with some success in in vitro culture systems (Cooper et al. 2004; Cusimano et al. 2009; Flucher et al. 1991). A recent study has reported using agrin to grow myotubes with the striated pattern of transversal triads (Falcone et al. 2014), essentially mimicking mature myofibres. Agrin is a large proteoglycan that induces clustering of acetylcholine receptors and aids the formation of neuromuscular junctions (Patthy & Nikolics 1993). Falcone et al. showed that up to 80% of their primary myotubes had organised triads after 10 days of agrin-supported differentiation, compared to only 20% in non-treated cultures (Falcone et al. 2014) (Figure 2.3b). Given that the triads are where EC coupling takes place, and EC coupling has been shown to be defective in the RyR1 I4895T mouse model, it seems important to attain triadic striations in my primary muscle cultures. Despite following the same protocol as Falcone et al., I did not find any striated myotubes in my cultures (Figure 2.3a & c).

a

Figures removed due to copyright restrictions

b

c

	No. striated myotubes	Total no. myotubes
WT	**0**	63
HET	**0**	61
Total	**0**	124

Figure 2.3: Quantification of striated myotubes in agrin-treated cultures

After 10 days of agrin-supported differentiation, myotubes were fixed and immunostained for RyR1 (a). Myotubes exhibiting a distinct, striped RyR1 patterning were scored as 'striated' (b). Image in (b) is adapted from (Falcone et al. 2014). Scorings indicate pooled myotubes from 3 different WT and HET mice (c). Scale bars 10µm.

Exposing fura2-loaded myotubes to the RyR1 agonist caffeine resulted in robust cytosolic Ca^{2+} signals (Figure 2.4) associated with contraction. This suggests that although there is a lack of triadic structure, RyR1 is still present and functional in these myotubes, making them an adequate model for studying EC coupling and how it affects mitochondrial function.

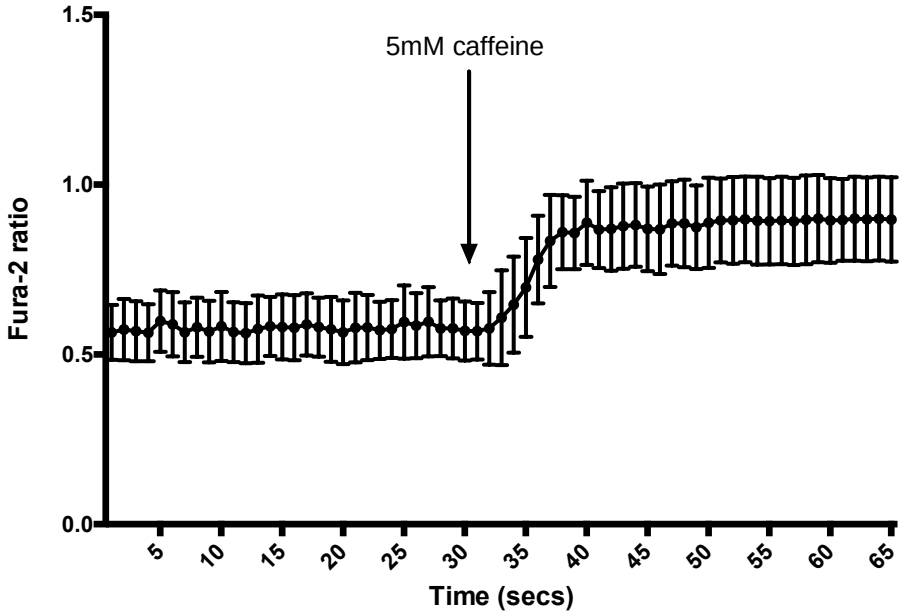

Figure 2.4 Agrin-treated myotubes are caffeine sensitive

Addition of 5mM caffeine (arrow) triggers SR Ca^{2+} release in agrin-treated myotubes loaded with fura-2 AM. This increase in $[Ca^{2+}]_c$ is observed as an increase in fluorescence intensity at 340nm (Ca^{2+} bound) and a decrease in fluorescence at 380nm (Ca^{2+} free) i.e. an increase in the ratio of 340nm/380nm (Fura-2 ratio). Trace represents the initial stage of the Ca^{2+} response of >25 myotubes originating from 4 different WT mice (n=4). Errors bars indicate SEM.

2.3.2 Ca^{2+} homeostasis is unaltered in primary HET myotubes

Previously, it has been shown that mature myofibres isolated from two different strains of HET RyR1 I4895T mice have reduced Ca^{2+} transients in response to RyR1 activation (Boncompagni et al. 2010; Loy et al. 2011). To see if this is also the case in my model, I applied different concentrations of caffeine to myotubes loaded with fura-2 AM and measured the change in fura-2 ratio (∆fura-2). No significant differences in ∆fura-2 were identified between WT and HET myotubes stimulated with 1mM (P=0.928), 2mM (P=0.607) or 5mM caffeine (P=0.454) (Figure 2.5a). It has also been suggested previously that the I4898T mutation in RyR1 causes chronic Ca^{2+} leak from the SR and elevated resting $[Ca^{2+}]_c$ (Lynch et al. 1999). In disagreement with this, no significant difference in resting cytosolic Ca^{2+} was observed (P=0.257) (Figure 2.5b).

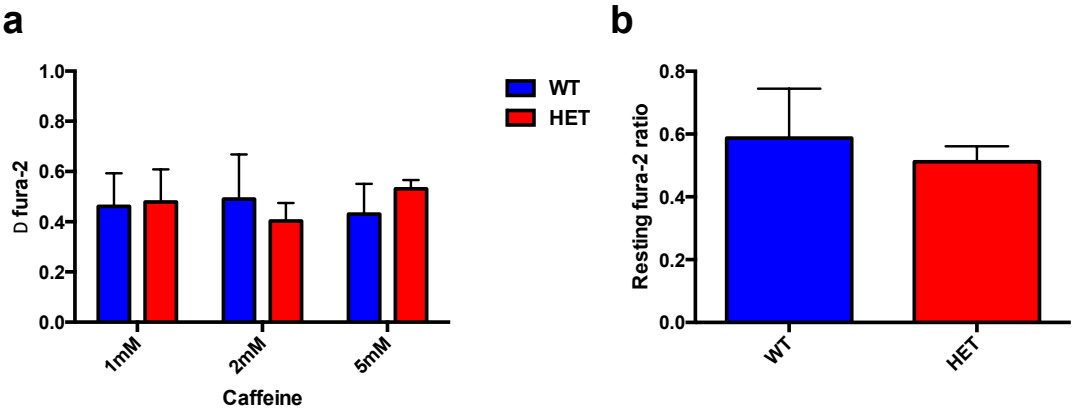

Figure 2.5: Average resting and agonist-induced cytosolic Ca^{2+} levels are similar between WT and HET mouse myotubes

Myotubes were loaded with fura-2 AM and stimulated with different concentrations of caffeine (a). Average fura-2 ratios prior to stimulation were used as a measure of resting cytosolic Ca^{2+} (b). ∆fura-2 was calculated as the difference between the average resting fura2 ratio and the peak ratio following caffeine addition. n ≥ 4 mice, with at least 3 myotubes measured per mouse (and thus per caffeine experiment). Myotube measurements from one mouse were averaged to give the mean value for that particular mouse. Therefore values shown are mean of means ± standard error.

Given that the I4895T mutation is associated with an 'EC uncoupled' RyR1 phenotype, I was surprised that caffeine-induced Ca^{2+} transients were not

significantly reduced in myotubes produced from the HET mouse. This may reflect the fact that they do not have the same triadic structure as a mature muscle fibre, which may be important for replicating physiological Ca^{2+} signals.

2.3.3 Single myofibres isolated from adult HET mice produce slightly higher Ca^{2+} transients in response to depolarisation

Given that myotubes are an immature form of a myofibre, I decided to also characterise Ca^{2+} homeostasis in mature myofibres isolated from the FDB muscle of adult WT and HET mice. As caffeine and 4-chloro-m-cresol did not seem to be reliable stimuli for this model, KCl was used to depolarise the myofibres, triggering EC coupling and Ca^{2+} release from the SR. Δfura-2 in response to 50mM KCl was significantly larger in HET myofibres (0.769 ± 0.00645) than in WTs (0.714 ± 0.0125) (P=0.0181), though this difference was relatively small (Figure 2.6a). Quantification of the number of fibres that responded to the KCl stimulus suggested that HET fibres are more likely to respond, though this result was not statistically significant (P=0.421) (Figure 2.6b). In agreement with my measurements in myotubes, resting cytosolic Ca^{2+} levels were not significantly different (P=0.0839) between WT and HET myofibres (Figure 2.6c).

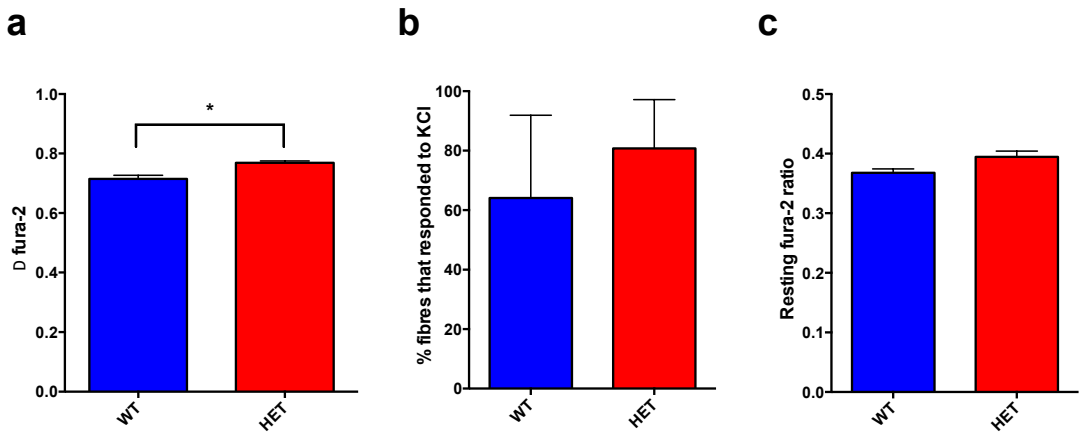

Figure 2.6: Average depolarisation-induced cytosolic Ca^{2+} rise is significantly higher in HET mutant fibres

FDB myofibres isolated from 6-7 month old mice were loaded with fura-2 AM and depolarised with 50mM KCl (a). The number of myofibres that produced a cytosolic

Ca^{2+} response to KCl was quantified (b). Average fura-2 ratio prior to stimulation was used as a measure of resting cytosolic Ca^{2+} (c). n=3 mice, with at least 5 myofibres measured per mouse. Measurements from one mouse were averaged to give the mean value for that particular mouse. Therefore values shown are mean of means ± standard error.

2.3.4 Mitochondrial distribution and $\Delta\Psi_m$ are unchanged in HET myofibres

$\Delta\Psi_m$ is a key bioenergetic parameter that determines respiratory rate, ATP synthesis and ROS generation. To assess whether $\Delta\Psi_m$ was affected in the mixed background mouse model, WT and HET FDB myofibres were imaged in the presence of TMRM, a cell-permeant cationic dye that is readily sequestered by active mitochondria (Figure 2.7a & b). Quantification of average basal TMRM fluorescence showed no significant difference between WT and HET myofibres (P=0.827) (Figure 2.7c).

Qualitative analysis of the same TMRM z stacks did not show a difference in mitochondrial distribution between WT and HET myofibres (Figure 2.7a & b). Previous work on the RyR1 I4895T and the RyR1 Y522S mouse models have shown the presence of contracture cores (localised regions of severe sarcomere shortening) where mitochondria are absent (Zvaritch et al. 2009; Boncompagni et al. 2009). I was unable to identify such contractures in the HET myofibres, though there is the possibility that during image collection I may have overlooked such structures as damage sustained to the fibre during the isolation process.

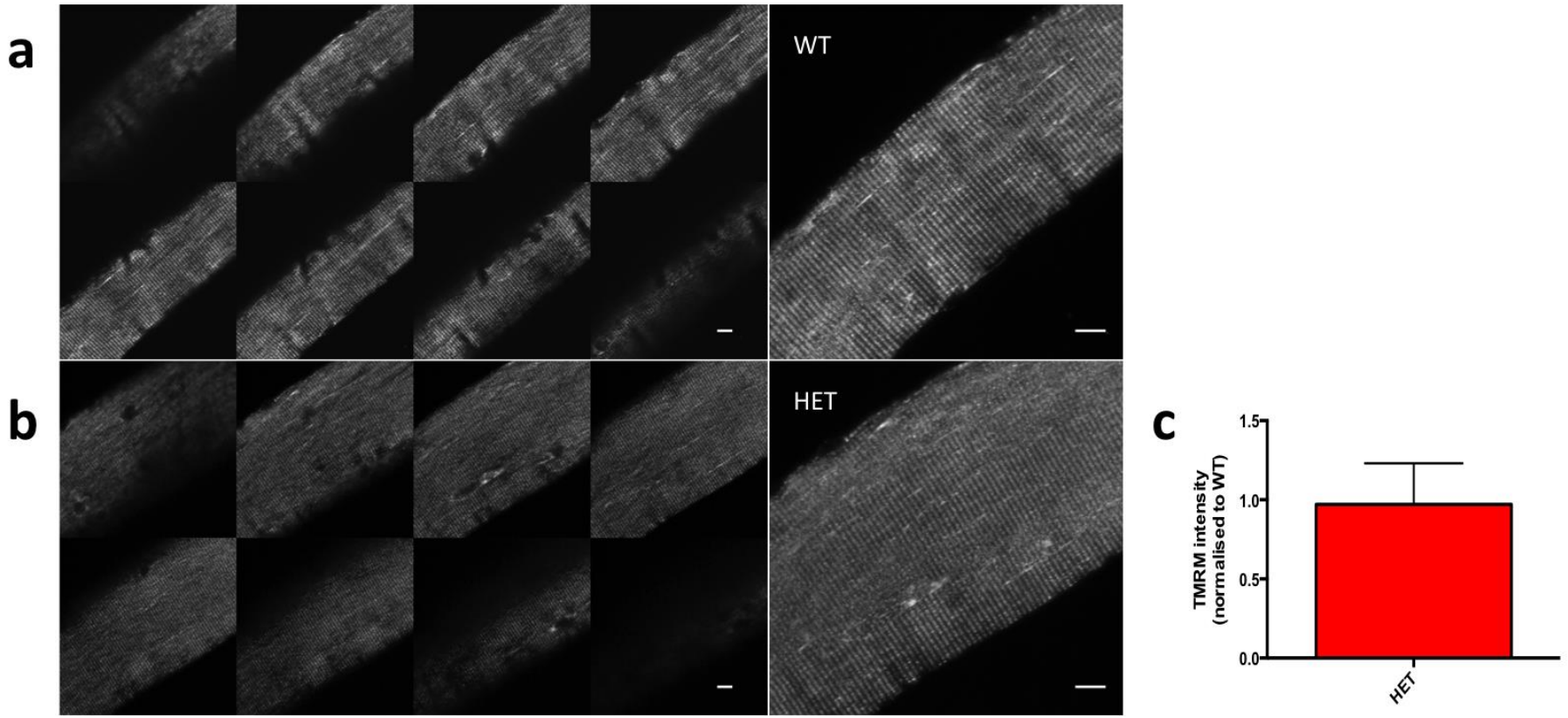

Figure 2.7: Resting $\Delta\Psi_m$ is similar between WT and HET myofibres

FDB myofibres isolated from 6-7 month old mice were loaded with TMRM and imaged from one end to the other through a z stack series (inset montages, a & b). Maximal projection images were used for intensity analysis (right hand image, a & b). Average TMRM fluorescence of HET myofibres was normalised to WT average on each experimental day (c). Scale bars 10μm. n=4 mice, with at least 7 myofibres measured per mouse. Measurements from one mouse were averaged to give the mean value for that particular mouse. Therefore values shown are mean of means ± standard error.

2.3.5 HET myofibres are not bioenergetically compromised

NADH (but not NAD^+) is fluorescent, absorbing light of about 350nm in wavelength and emitting fluorescence at 460nm. To get a rough indication of cellular redox state and energy metabolism in this new RyR1 I4895T mouse model, resting NADH fluorescence was measured in single WT and HET myofibres (Figure 2.8a). Quantification of average fluorescence showed no significant difference between WT and HET myofibres (P=0.224) (Figure 2.8b).

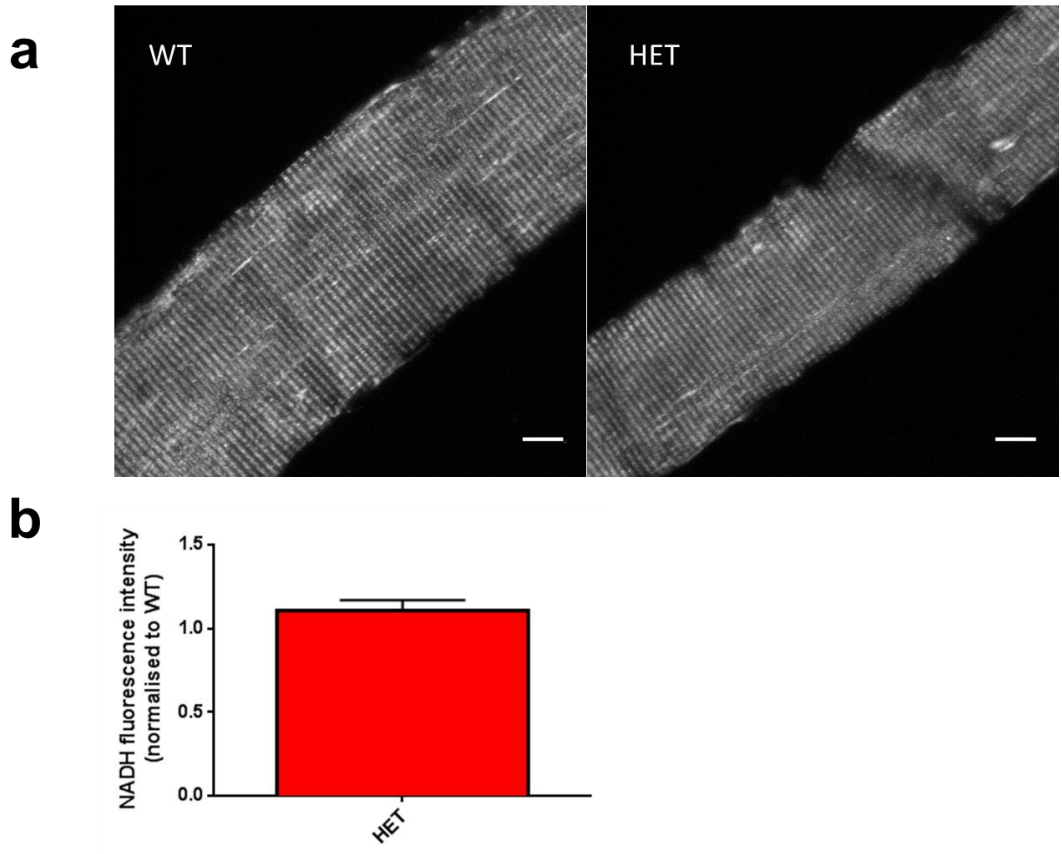

Figure 2.8: Resting NADH levels are similar between WT and HET myofibres

Representative maximal projections of NADH fluorescence in FDB myofibres isolated from 6-7 month old WT and HET mice (a). Average NADH fluorescence of HET myofibres was normalised to WT average on each experimental day (b). Scale bars 10µm. n=2 mice, with at least 12 myofibres measured per mouse. Measurements from one mouse were averaged to give the mean value for that particular mouse. Therefore values shown are mean of means ± standard error.

Basal NADH signal is difficult to interpret in terms of cell redox state; the NADH/NAD^+ pool may differ between two separate biological preparations. For example, two samples with identical resting NADH levels may have considerably different NAD^+ levels. Thus to directly compare the redox state of two specimens, the dynamic range of NADH fluorescence should be measured (Duchen 2004). This can be done using drug treatments to maximally reduce and maximally oxidise mitochondrial NAD (Figure 2.9). I did trial such an experiment on the isolated mouse myofibres but concluded that it was practically too difficult to carry out; there was usually only one fibre in a field and it often moved upon drug addition. In addition, each mouse preparation gave a relatively low yield of healthy fibres, thus limiting the number of different experiments I could carry out.

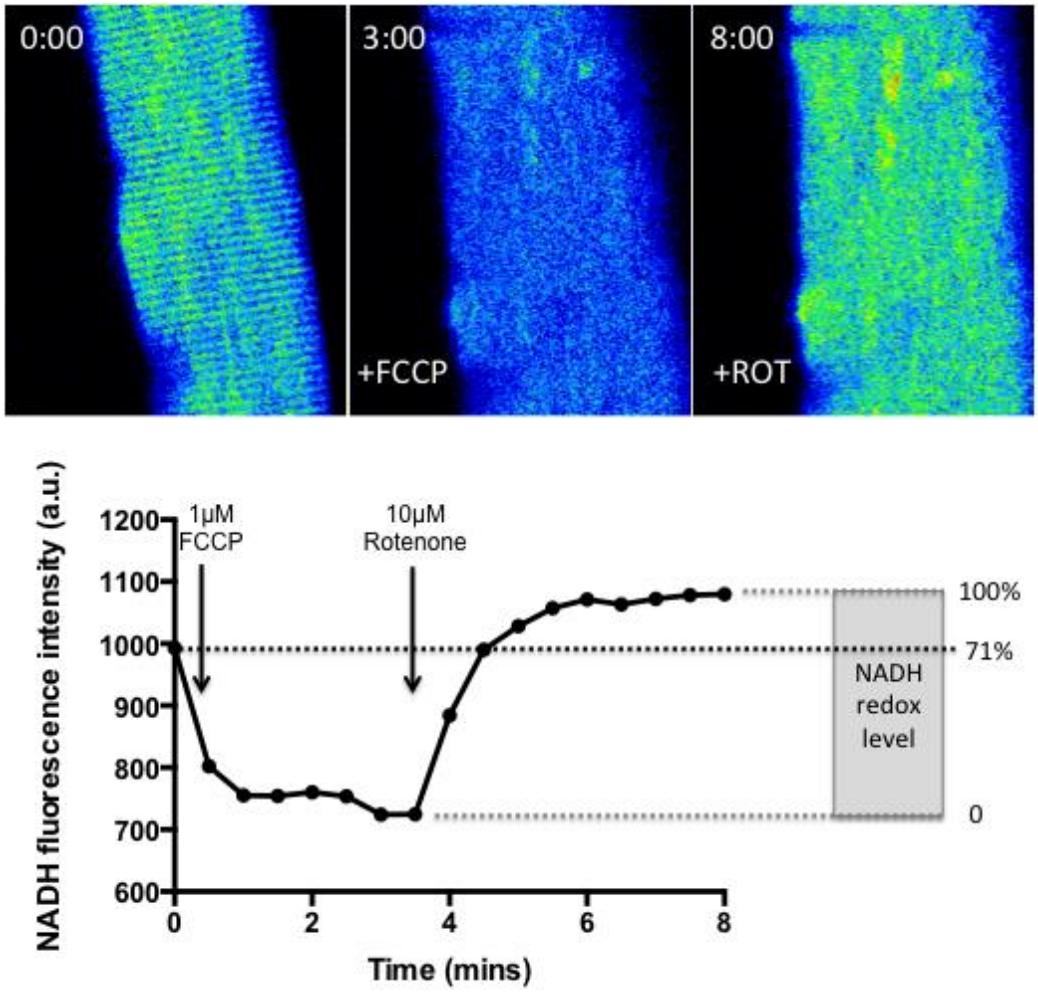

Figure 2.9: Quantifying the dynamic range of NADH fluorescence

Example of an experiment for quantifying the dynamic range of NADH fluorescence. Basal NADH fluorescence was measured at t=0. Addition of uncoupler FCCP

caused a decrease in fluorescence, as the mitochondrial NADH pool became maximally oxidised i.e. 0% NADH redox level. Addition of complex I inhibitor rotenone caused an increase in fluorescence, as the mitochondrial NADH pool became maximally reduced i.e. 100% NADH redox level. Basal fluorescence was then calibrated to these minimum and maximum values to give a measure of NADH redox level.

Respirometry measurements also give an indication of cellular bioenergetics and the functionality of the electron transport chain. Rather than isolating mitochondria, which requires a lot of muscle tissue, muscle fibres can be gently permeabilised to allow for the exchange of soluble molecules between the cytosolic phase and the external medium without permeabilisation of the mitochondrial membranes. If the mitochondrial membranes have become damaged by the permeabilisation process, addition of cytochrome c causes a substantial rise in O_2 consumption (Pesta & Gnaiger 2012). Having previously optimised the permeabilisation procedure, no effect of cyt c was ever seen in my experiments (see figure 2.2 for example trace and figures 2.10 & 2.11 for average values). Respirometry measurements were carried out on both fast-twitch (Figure 2.10) and slow-twitch (Figure 2.11) muscles but there was no significant difference between WT and HET muscles in any respiratory state in either muscle type.

	Leak		ADP		Cyt c		Succinate		FCCP		Rotenone	
	WT	**HET**	**WT**	**HET**	**WT**	**HET**	**WT**	**HET**	**WT**	**HET**	**WT**	**HET**
Day 1	4.6	23.9	23.2	89.3	20.6	69.6	42.1	106.1	49.7	109.1	29.8	62.3
Day 2	34.0	12.4	93.0	45.2	81.0	43.3	115.3	84.1	119.2	83.4	72.0	60.4
Day 3	3.9	21.6	32.9	54.4	30.5	47.3	58.0	72.8	68.4	76.0	43.7	45.3
Day 4	27.8	16.4	124.3	115.6	113.8	104.7	126.7	129.5	162.2	164.9	97.6	99.3
Mean	**17.6**	**18.6**	**68.4**	**76.2**	**61.5**	**66.2**	**85.5**	**98.1**	**99.9**	**108.4**	**60.8**	**66.8**
S.D.	15.6	5.16	48.4	32.4	43.7	28.1	41.7	25.1	50.9	40.3	30.2	22.9
P value	0.909		0.799		0.861		0.624		0.802		0.760	

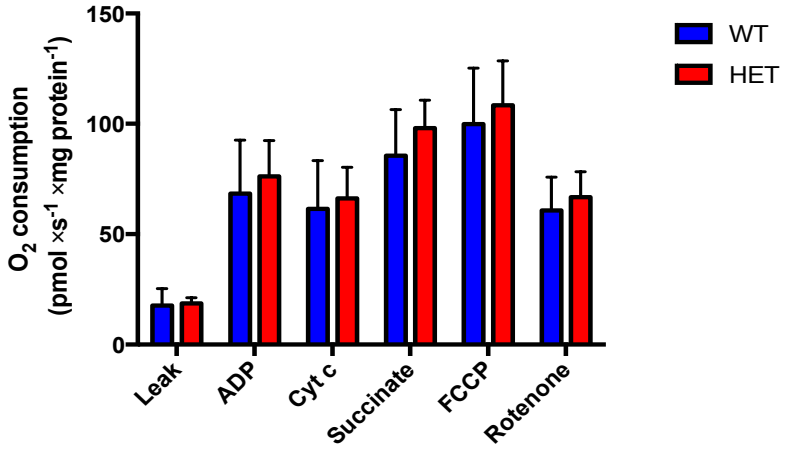

Figure 2.10: Mitochondrial O_2 consumption in permeabilised HET EDL muscle fibres is comparable to WT EDL

High-resolution respirometry was used to measure O_2 consumption of permeabilised WT and HET EDL fibres in the leak state (only glutamate and malate present), active state (ADP also present), complex II driven state (succinate), maximal state (FCCP) and under complex I inhibition (rotenone). Raw O_2 consumption measurements (pmol s^{-1} mg $protein^{-1}$) from each experimental day are shown in the table. The mean averages of these measurements are shown in the bar graph (error bars SEM). n=4 mice (one on each experimental day), with 3 fibre bundles measured per mouse.

	Leak		ADP		Cyt c		Succinate		FCCP		Rotenone	
	WT	**HET**	**WT**	**HET**	**WT**	**HET**	**WT**	**HET**	**WT**	**HET**	**WT**	**HET**
Day 1	6.2	37.1	19.9	61.8	12.0	40.6	46.8	77.3	49.5	70.1	30.7	47.0
Day 2	25.3	12.6	106.0	60.2	98.8	57.0	138.5	86.8	127.5	98.8	79.3	48.4
Day 3	13.1	34.3	47.3	86.4	45.6	60.8	69.7	93.8	72.9	101.2	50.1	58.6
Day 4	12.0	4.4	35.8	42.8	32.4	46.5	75.1	107.8	77.8	113.8	46.0	63.1
Mean	**14.1**	**22.1**	**52.2**	**62.8**	**47.2**	**51.2**	**82.5**	**91.4**	**81.9**	**96.0**	**51.5**	**54.2**
S.D.	8.03	16.1	37.6	18.0	37.1	9.31	39.3	12.8	32.8	18.5	20.3	7.83
P value	0.411		0.630		0.841		0.681		0.484		0.811	

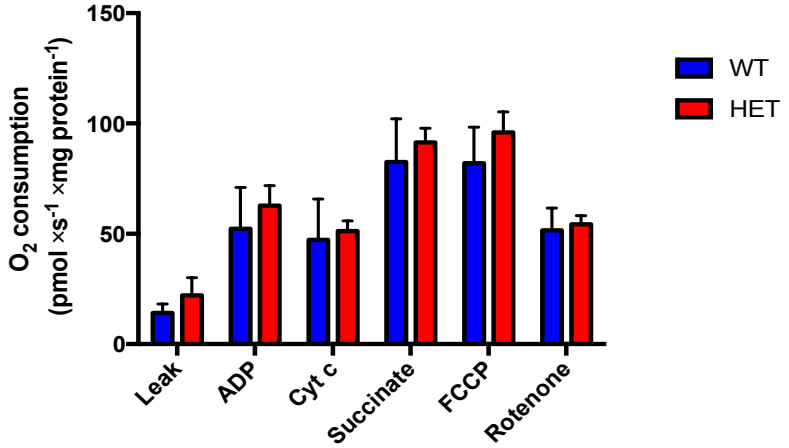

Figure 2.11: Mitochondrial O_2 consumption in permeabilised HET soleus muscle fibres is comparable to WT soleus

High-resolution respirometry was used to measure O_2 consumption of permeabilised WT and HET soleus fibres in the leak state (only glutamate and malate present), active state (ADP also present), complex II driven state (succinate), maximal state (FCCP) and under complex I inhibition (rotenone). Raw O_2 consumption measurements (pmol s^{-1} mg $protein^{-1}$) from each experimental day are shown in the table. The mean averages of these measurements are shown in the bar graph (error bars SEM). n=4 mice (one on each experimental day), with 3 fibre bundles measured per mouse.

2.3.6 Levels of expression of complex III and IV subunits are reduced in fast-twitch muscle from HET adult mice

Alterations in electron transport chain assembly can lead to respiratory deficiency, as demonstrated in many mitochondrial disorders. To assess relative levels of electron transport chain subunits in this RyR1 I4895T mouse model, western blotting analysis was carried out on EDL and soleus homogenates using a commercial antibody cocktail (Figure 2.12a & d). Quantification showed that the relative levels of complex III were significantly reduced in HET fast-twitch EDL muscle (WT 0.548 ± 0.039; HET 0.432 ± 0.015; P=0.0331) (Figure 2.12b). A significant reduction in the relative levels of complex IV was also observed (WT 0.752 ± 0.036; HET 0.570 ± 0.025; P=0.00629) (Figure 2.12b). Although there was a trend for reduced expression of each complex subunit in HET slow-twitch soleus muscle, the differences were not statistically significant (Complex V: P=0.564, complex IV: P=0.314, complex III: P=0.532, complex II: P=0.204, complex I: P= 0.470) (Figure 2.12c).

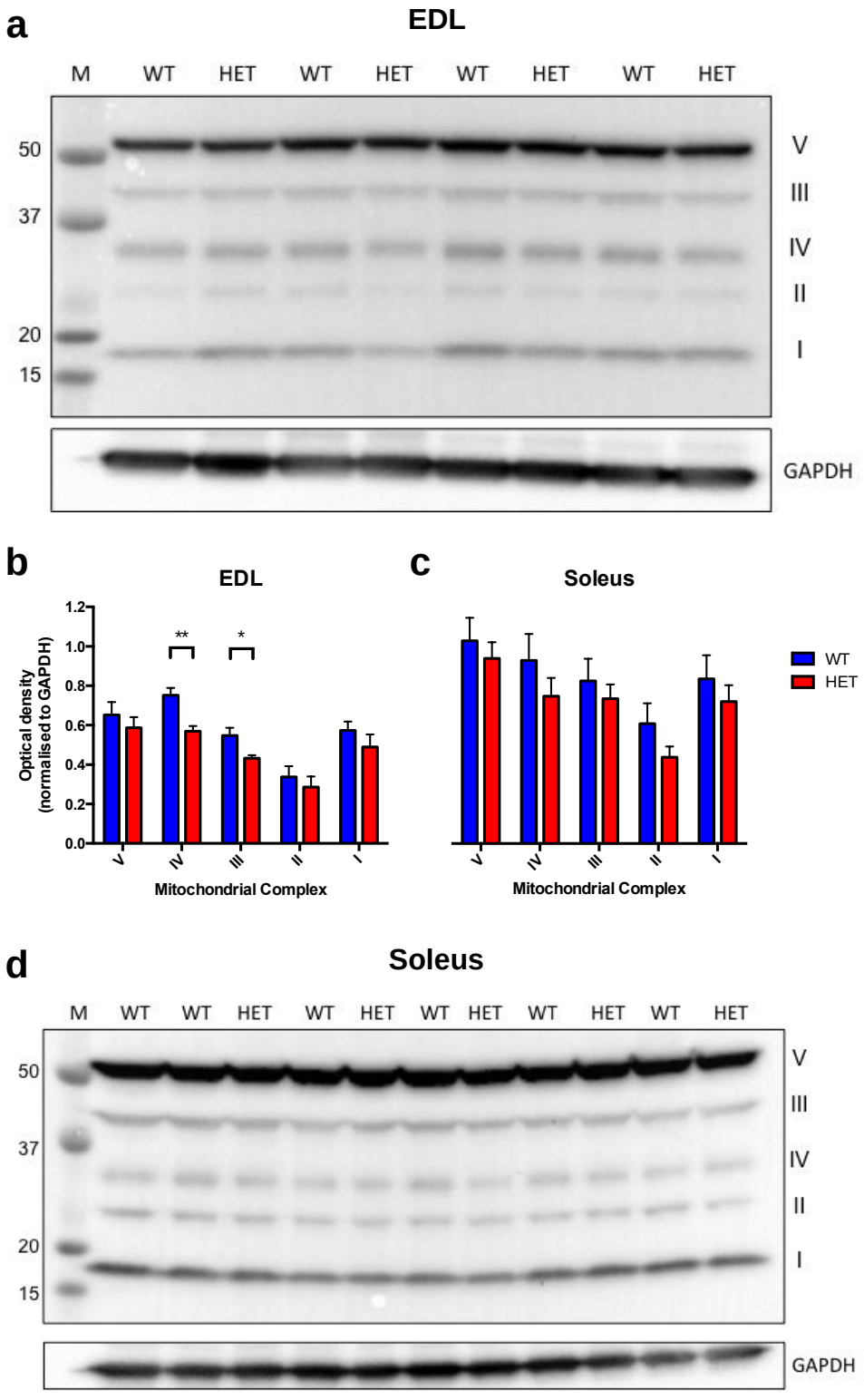

Figure 2.12: Levels of complex III and IV subunits are reduced in HET EDL muscle

Muscle homogenates from EDL (a) and soleus (d) were immunoblotted for the following complex subunits: complex I NDUFB8 (20kDa), complex II SDHB (30kDa), complex III UQCRC2 (48kDa), complex IV MTCO1 (40kDa), complex V ATP5A

(55kDa). Band intensities were normalised to GAPDH loading control (b & c). n≥4 mice

2.3.7 Mitochondrial biogenesis appears normal in skeletal muscle of HET adult mice

Down regulation of electron transport chain subunits at the protein level could suggest that HET mice have fewer mitochondria in their skeletal muscle, which could be a consequence of reduced mitochondrial biogenesis. To test this theory, western blotting analysis was carried out on EDL and soleus homogenates using an antibody targeted to TFAM (Figure 2.13a & b), which is a major transcription factor driving the expression of mitochondrial-encoded proteins. Densitometry analysis showed no significant differences between WT and HET mice, in either fast-twitch EDL (P=0.811) (Figure 2.13c) or slow-twitch soleus muscle (P=0.653) (Figure 2.13d).

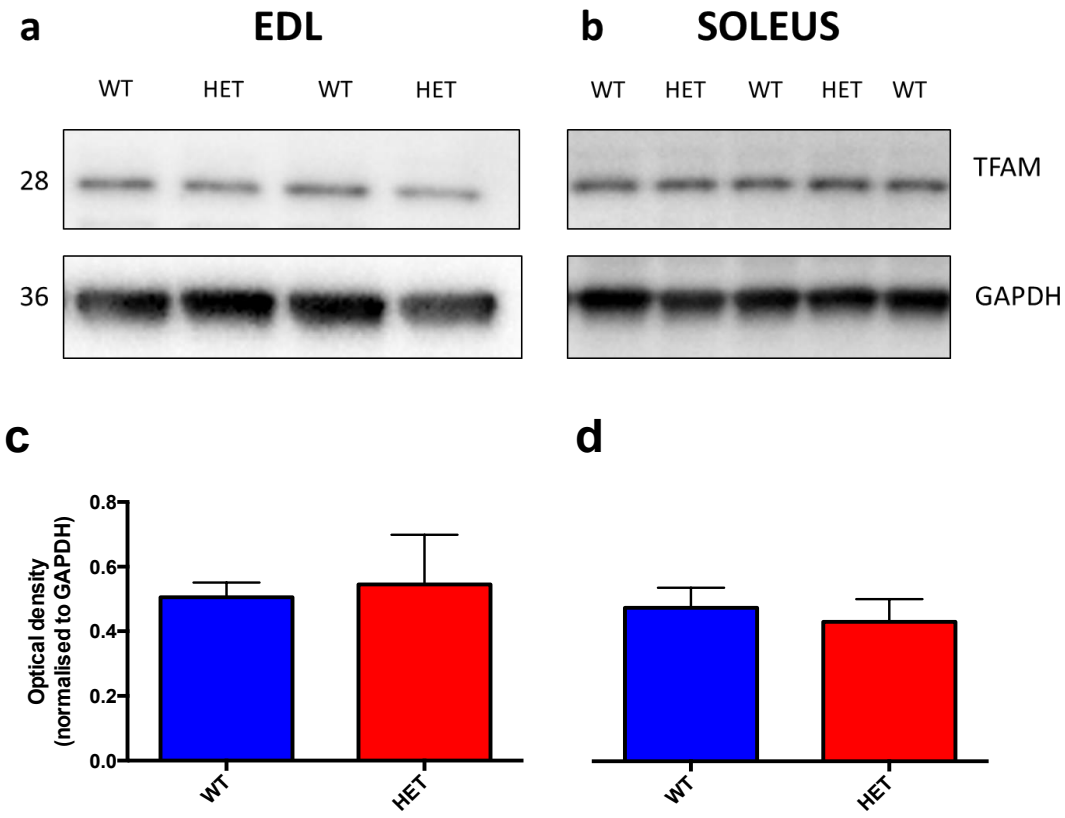

Figure 2.13: TFAM protein levels are similar in WT and HET skeletal muscle

Muscle homogenates from EDL (a) and soleus (b) were immunoblotted for TFAM. Band intensities were normalised to GAPDH loading control (c & d). n≥4 mice

2.4 Discussion

In this chapter, I have characterised the RyR1 and mitochondrial phenotype of a new sub-line of RyR1 I4895T mice by using two different muscle cell models. The first consisted of myotubes produced from neonates, which were treated with agrin in an attempt to replicate the striated triadic structure seen in mature myofibres. Despite following the same protocol used by Falcone et al., I could not identify any striated myofibres in my primary cultures at day 10 of agrin-supported differentiation. Instead the myotubes had diffuse RyR1 staining, similar to that described by Falcone et al. at day 5 of agrin-supported differentiation. This suggests that my myotubes may have been slower to mature and perhaps needed longer in culture. I did try extending the differentiation period but it was too difficult to quantify striations as most of the cells had detached themselves from the coverslips by day 12 (probably through natural cell death or increased spontaneous contractions).

2.4.1 RyR1 phenotype

As a skeletal muscle model, primary myotubes may not be structurally accurate but stimulation with caffeine proved that they have a functional RyR1 and are contractile. Previous studies have shown that the I4895T mutation in RyR1 causes a reduction in stimulated SR Ca^{2+} release (Avila et al. 2001; Boncompagni et al. 2010; Loy et al. 2011). In contrast, I found that HET myotubes behaved similarly to controls and did not show reduced cytosolic Ca^{2+} transients in response to any caffeine concentration tested. Although these myotubes did show spontaneous twitching in culture, it is unlikely that they experienced the same frequency and intensity of contractile activity that would occur in vivo. Perhaps if a regular in vitro activity regime were implemented, such as applying caffeine or electrical stimulation, abnormalities in Ca^{2+} homeostasis and mitochondrial function might be revealed in the HET cells.

As I was unable to show a RyR1-related Ca^{2+} defect in the HET myotubes, I decided to switch to a more mature muscle cell model, which consisted of

isolated FDB myofibres from adult mice. Initially, I attempted to measure cytosolic Ca^{2+} signals in myofibres loaded with fura-2 and stimulated with 10mM caffeine or 500uM 4-chloro-m-cresol (another RyR1 agonist) (as in 2.2.7). Unfortunately these RyR1 agonists failed to reliably produce Ca^{2+} signals in even isolated WT fibres so I proceeded to use KCl-induced depolarisation as an alternative stimulus for muscle contraction. My results showed a very small but significant increase in depolarisation-induced Ca^{2+} release in the HET myofibres. This result was surprising as previous mouse studies have shown reduced Ca^{2+} transients in response to electrical stimulation (Boncompagni et al. 2010; Loy et al. 2011). Although depolarising with KCl has not been tested in HET I4895T myofibres before, it should in theory stimulate RyR1-mediated Ca^{2+} release in the same way as an electrical stimulus, so it's difficult to understand why I saw the opposite in this model. Perhaps it reflects something unreliable about my myofibre isolating procedure, which might also explain the problems I had with caffeine and 4-chloro-m-cresol stimulation.

2.4.2 Mitochondrial phenotype

To characterise the bioenergetic status of this new mouse sub-line, I measured resting $\Delta\Psi_m$, NADH levels and O_2 consumption in isolated HET myofibres. No significant differences were found in any of these measurements, suggesting that the I4895T mutation in RyR1 does not compromise bioenergetic function on a mixed genetic background. This is consistent with the observation that this sub-line does not show an 'EC uncoupled' RyR1 phenotype. To date, these bioenergetic parameters have not been assessed in human or mouse models expressing the RyR1 I4895T mutation. As mitochondrial energy production is closely linked to cytosolic Ca^{2+} signalling (see Introduction 1.4.1), I would expect mitochondrial metabolism to be reduced in models showing an 'EC uncoupled' RyR1 phenotype.

Mitochondrial function was also characterised by immunoblotting for OXPHOS subunits in fast-twitch and slow-twitch HET muscle. This showed

that there was a significant decrease in the expression of Complex III and IV subunits in fast-twitch EDL muscle. Given that type I fibres are more affected in human CCD (ENGEL et al. 1961; Telerman-Toppet et al. 1973; Isaacs et al. 1975), I would have expected to see a more of a defect in the soleus rather than the EDL muscle. A possible explanation for this discrepancy maybe because mice are physiologically more dependent on fast-twitch muscle activity (Close 1972). There was certainly a trend for reduced expression of all complex subunits in both fast-twitch and slow-twitch HET muscle, but the degree of variability between mice made this statistically non-significant. Reduced complex subunit expression might suggest that HET muscles have smaller mitochondrial populations, which would correspond with the presence of cores (though I found no visual evidence of cores or mitochondrial displacement in the HET fibres). A reduction in mitochondrial number could be the result of diminished mitochondrial biogenesis, but this did not seem to be the case as TFAM protein levels were similar between WT and HET muscles. An alternative explanation is that the mitochondria are being turned over quicker in the HET muscles; this idea could be explored in future by assessing the activity of proteins involved in autophagy/mitophagy. As mitochondria move towards physiological Ca^{2+} signals (Yi et al. 2004), it would also be interesting to observe mitochondrial trafficking in muscles affected by cores; perhaps mitochondria are re-located from the cores, rather than being destroyed.

2.4.3 Evaluation of I4895T mouse models

Although the I4895T mutation in RyR1 is known to result in ‘EC uncoupling’ and reduced Ca^{2+} ion permeation (Zvaritch et al. 2009; Loy et al. 2011), I was unable to identify such a defect in primary cells derived from this mouse sub-line, which greatly limits its significance in core myopathy research. In contrast to the severely affected congenic mice produced by Zvaritch et al., this sub-line appeared quite healthy and never showed any sign of physical muscle dysfunction (though they were usually culled before reaching a year old). It seems that successive breeding to a C57BL/6J background has drastically diluted the disease phenotype as well as the functional RyR1

phenotype of the mouse, which would explain why mitochondrial function is mostly unaffected. Perhaps the mice and/or cell models need to be put under physiological stress to reveal a phenotype, so I suggest that any future work using this mouse sub-line explores this idea. With hindsight, histological analysis of skeletal muscle from these mice would have been beneficial in determining whether they have a core myopathy; this should also be included in future work using this sub-line.

The association between genetic background and phenotype in the I4895T mice closely reflects the variable disease presentation seen in heterozygous individuals from human families carrying the analogous I4898T mutation (Lynch et al. 1999; Monnier et al. 2001) and across the core myopathy spectrum as a whole. In contrast to human CCD, type I fibre predominance is not a feature of mice expressing the RyR1 I4895T mutation (Zvaritch et al. 2009). Nevertheless, the human disease is somewhat replicated through the preferential involvement of type I fibres, where greater structural defects and z-line streaming have been reported (Boncompagni et al. 2010). The congenic I4895T mouse sub-line also presented with minicores and nemaline rods, which have been observed in a few human CCD cases but - somewhat strangely - never with humans expressing the analogous I4898T mutation (Zvaritch et al. 2009).

Chapter 3 The effect of the STAC3 W284S mutation on intracellular Ca^{2+} signalling and bioenergetics

3.1 Introduction

As part of a whole exome sequencing (WES) project on congenital myopathy patients, a mutation in *STAC3* was identified in a male teenager with King-Denborough Syndrome (KDS) (Zaharieva et al. 2014). KDS is a rare condition characterised by malignant hyperthermia susceptibility (MHS), delayed motor development, short stature, skeletal abnormalities and a variety of dysmorphic features such as ptosis, malar hypoplasia (underdeveloped cheekbones) and low-set ears (Dowling et al. 2011). The patient in the WES study specifically presented with severe scoliosis, learning difficulties, sickle cell disease with recurrent crises and had experienced a malignant hyperthermia reaction during a previous anaesthetic induction. Interestingly, his muscle biopsy sample also showed core-like changes.

Since mutations in RYR1 have been associated with KDS (D'Arcy et al. 2008; Dowling et al. 2011), the patient had previously undergone RYR1 screening but the results came back negative. Subsequent whole exome sequencing analysis identified a homozygous missense mutation (c.851G>C; rs140291094) in the STAC3 gene (Zaharieva et al. 2014). STAC3 is a poorly characterised adaptor protein that has been shown to have a role in EC coupling and skeletal muscle development (see Introduction 1.5 & 1.6, respectively). At the amino acid level, the patient's mutation corresponds to a W284S change, which is situated in the first SH3 domain of STAC3 and so affects its binding specificity (Horstick et al. 2013). This could affect its ability to chaperone the principal DHPR subunit, $Ca_V1.1$, to the t-tubule membrane, according to a recent study (Polster et al. 2015).

The W284S mutation in STAC3 is known to cause NAM (see Introduction 1.7) but has never before been associated with core formation. In this chapter I will assess the impact that the STAC3 mutation has on Ca^{2+}

signalling and mitochondrial function in skin fibroblasts derived from the patient described above. Although STAC3 is predominantly expressed in skeletal muscle, preliminary characterisation of these fibroblasts will be the first step towards a longer project using MyoD-transduced or iPSC-derived myotubes (discussed in 3.4.4). It is useful to know the properties of fibroblasts before converting them into a muscle model and to see how Ca^{2+} signalling changes specifically with differentiation.

3.2 Methods

3.2.1 Chemicals

All chemicals were purchased from Sigma unless otherwise stated.

3.2.2 Cell culture

Primary human fibroblasts were obtained from the Biobank at the MRC Centre for Neuromuscular Disease, London. Two control samples with no known neuromuscular disease were age-matched to the affected individual. Fibroblasts were cultured in high glucose (4.5g/L) DMEM with Glutamax, supplemented with 10% FBS, 50 units/mL penicillin and 50ug/mL streptomycin (hereafter referred to as 1% PS) (all from Invitrogen).

3.2.3 Cytosolic Ca^{2+} imaging

Cells were plated on 22mm glass coverslips and measurements were carried out in RB. Cells were loaded with 5μM indo-1 AM (Molecular Probes) for 30min at RT before being washed with RB and imaged (excitation at 351nm, emission simultaneously detected at 400nm and 475nm) on a Zeiss 510 UV-VIS CSLM using a 40x objective and a 37°C heated stage.

ImageJ (NIH) was used for image analysis. Background was subtracted from both 400nm and 475nm images and regions of interest (ROIs) were drawn around individual cells. 400nm/475nm ratio was used to illustrate cytosolic Ca^{2+} levels in each cell. Resting indo-1 ratio was defined as the average ratio over the first 24 secs before 10μM histamine addition. Δindo-1 was calculated as the difference between the resting ratio and the peak ratio following histamine stimulation.

3.2.4 Measurements of resting mitochondrial membrane potential

Fibroblasts were equilibrated with RB containing 25nM TMRM for 15 mins at 37°C. Confocal images were then acquired on a Zeiss 510 UV-VIS CLSM

using a 40x oil objective. RB containing only 25nM TMRM was present throughout imaging. Fluorescence was excited at 535nm and measured at >560nm.

ImageJ was used for image analysis. ROIs were drawn around individual cells and images were thresholded to quantify the mean of mitochondria-localised signal intensities within each ROI. Identical acquisition settings and threshold values were used in repeat experiments.

3.2.5 Respirometry of intact cells

Cells were trypsinised and resuspended at 1 million cells/mL in DMEM buffered with 20mM HEPES, supplemented with 5.5mM glucose, 2mM glutamine and 1mM pyruvate. Respiration rates were measured at 37°C with the High-Resolution Oxygraph (Oroboros Oxygraph-2k). Once resting rate had stabilised, 2.5μM oligomycin A was added to measure leak respiration, 1μM FCCP to determine maximal oxidative capacity and 2.5μM antimycin A to measure non-mitochondrial (background) O_2 consumption. Each of these respiratory states was defined as the average value over a user-defined region of stabilised signal (Figure 3.1).

3.2.6 Statistics

Data for both control cell lines was pooled together and compared with data for the STAC3 W284S cell line. Values are presented as mean ± standard error. Statistical analysis was performed using Prism 6 (GraphPad software). Unpaired two tail t-tests were applied to test significance to a P value of 0.05. Significant differences are indicated with asterisks (* if $P<0.05$, ** if $P<0.01$, *** if $P<0.001$, **** if $P<0.0001$). N indicates total number of cells measured unless otherwise stated.

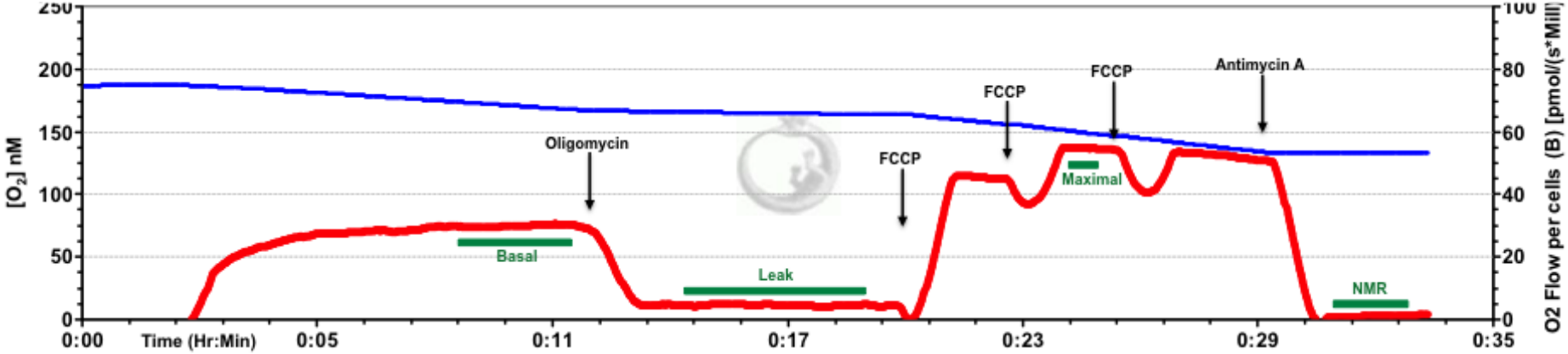

Figure 3.1: Example of O_2 consumption measurements of intact cells

Blue line indicates O_2 concentration inside the chamber, while the red line shows O_2 flux per million cells. After adding the cell suspension, the chambers were allowed to acclimatise until a stable signal was achieved (Basal/resting state). 2.5µM oligomycin was added to induce the leak state, followed by titrations of 1µM FCCP to reach the maximal respiratory rate. A final addition of 2.5µM Antimycin A was used to measure non-mitochondrial respiration (NMR). Green bars indicate regions over which average respiratory state values were calculated.

3.3 Results

3.3.1 The W284S mutation in STAC3 increases histamine-induced Ca^{2+} release

Previous studies have shown that STAC3 plays a role in EC coupling (Horstick et al. 2013; Nelson et al. 2013). Although the EC coupling machinery is only present in muscle tissue, it was thought that the STAC3 W284S fibroblasts might reveal a disorder in general Ca^{2+} homeostasis in the patient. To visualise intracellular Ca^{2+} levels, control and STAC3 W284S fibroblasts were loaded with indo-1 AM. Like fura-2, indo-1 is a ratiometric Ca^{2+} indicator that is not affected by loading conditions or bleaching. While fura-2 shows a shift in its excitation spectra when it binds Ca^{2+}, indo-1 shows a shift in its emission spectra, from about 475nm without Ca^{2+} to about 400nm with Ca^{2+} (Figure 3.2). This means that only one excitation laser is required for indo-1, which allows for faster acquisition times and a more accurate description of intracellular Ca^{2+} release.

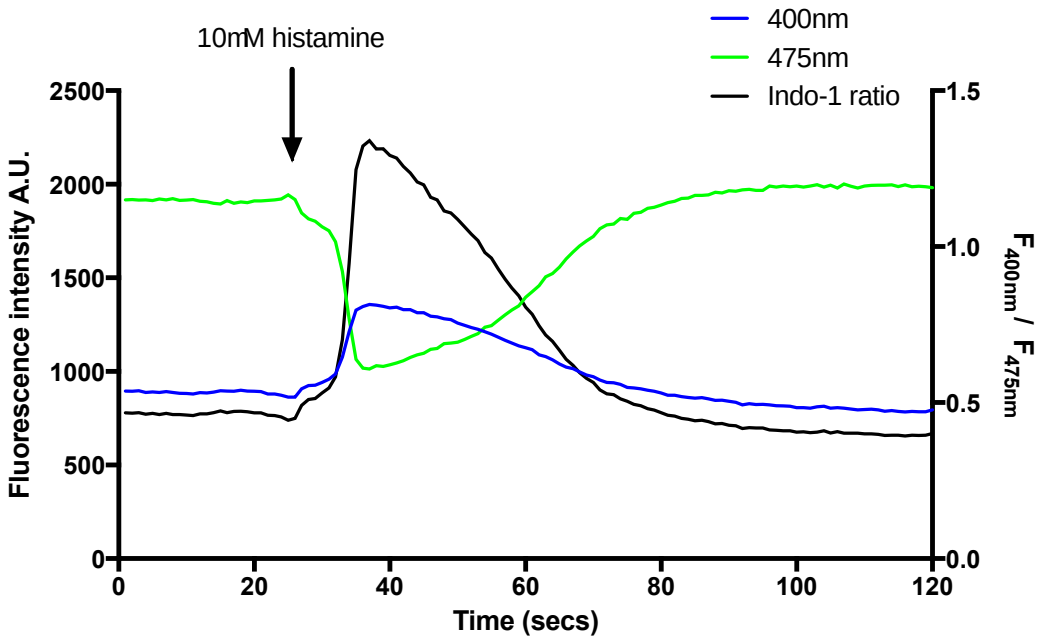

Figure 3.2: Example of indo-1 Ca^{2+} measurements

When excited at 350nm, indo-1 emits fluorescence at 400nm (blue) and 475nm (green). An increase in $[Ca^{2+}]_c$ is observed as an increase in fluorescence at 400nm and a decrease in fluorescence at 475nm, which corresponds to an increase in indo-1 ratio (right-hand y axis, black trace).

Quantification of average Δindo-1 ratio showed that histamine evoked significantly more Ca^{2+} release into the cytosol of the STAC3 W284S cells (0.775 ± 0.0996) than in controls (0.423 ± 0.0391) (P=0.0003), although there was a lot of cell-to-cell variability (Figure 3.3a & c). Some of the STAC3 W284S cells also demonstrated a considerable amount of oscillatory activity post-histamine addition (Figure 3.3a). This suggests that the STAC3 mutation is somehow having a global effect on Ca^{2+} signalling in the patient.

Seeing as this patient has an MHS phenotype, and MHS is associated with an increase in SR leak (see section 1.4), I also measured the average resting indo1 ratio of the fibroblast populations. This showed that although the STAC3 W284S cells tended to have higher resting cytosolic Ca^{2+} levels (0.429 ± 0.0531) than control cells (0.325 ± 0.0258), the difference was not statistically significant (P=0.0555) (Figure 3.3b).

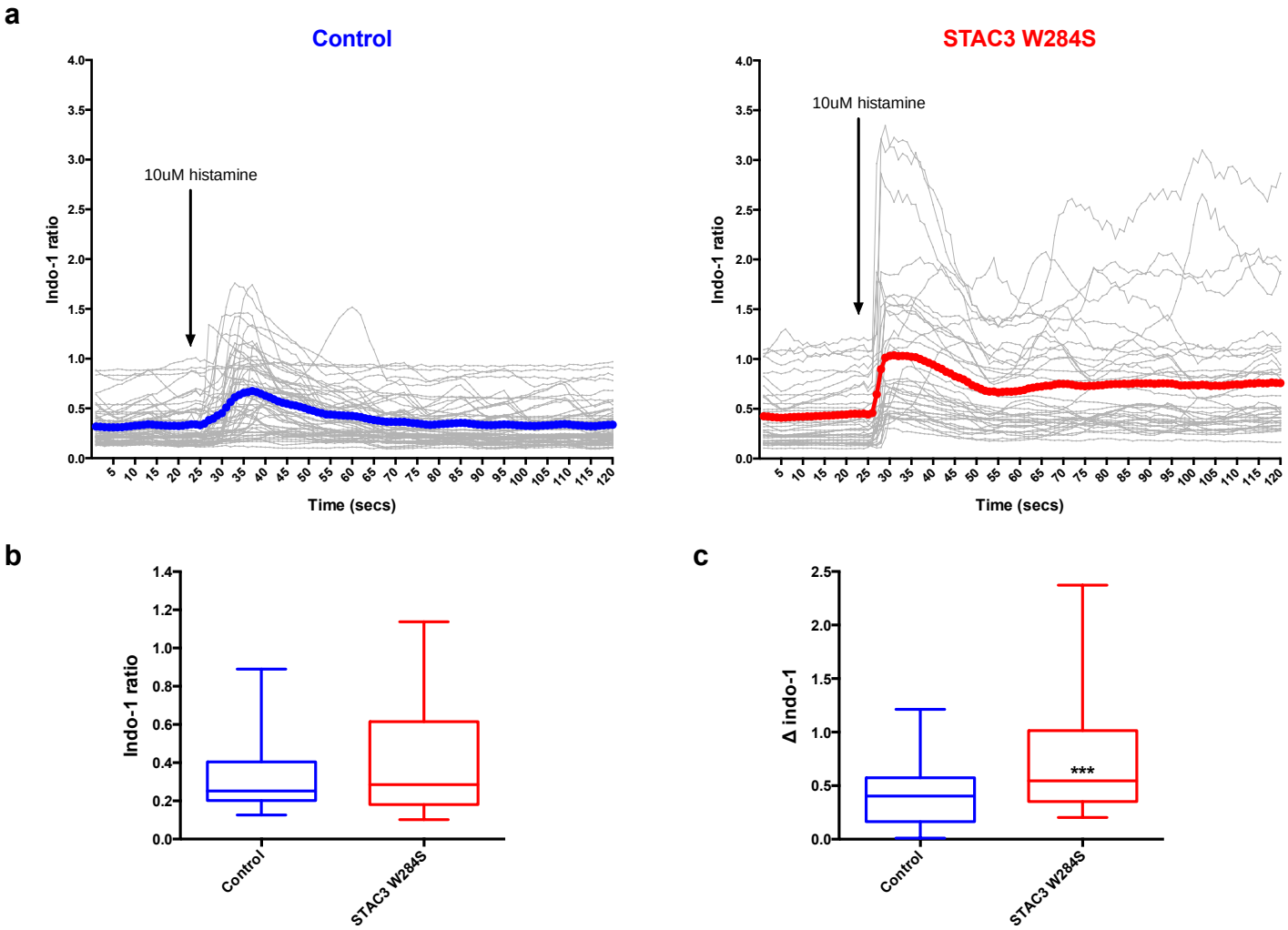

Figure 3.3: Intracellular Ca^{2+} signals are elevated in STAC3 W284S fibroblasts

Control (blue) and STAC3 W284S (red) fibroblasts were loaded with indo-1 AM and stimulated with 10μM histamine (a). Coloured trace illustrates average response of all cells (grey traces). Average indo-1 ratio prior to stimulation was used as a measure of resting cytosolic Ca^{2+} concentration (b). ⊿indo-1 was calculated as the difference between the average resting indo1 ratio and the peak ratio following histamine addition (c). n>35 cells measured over 3 different experimental days.

3.3.2 Mitochondrial depolarisation in STAC3 W284S fibroblasts

$\Delta\Psi_m$ is a key bioenergetic parameter that gives an indication of mitchondrial function. To assess whether $\Delta\Psi_m$ was affected by the STAC3 W284S mutation, control and STAC3 W284S fibroblasts were imaged in the presence of TMRM (Figure 3.4a). STAC3 W284S cells had significantly reduced TMRM fluorescence (0.867 ± 0.0163) compared to controls (1.001 ± 0.0124) (P<0.0001) (Figure 3.4b), which shows that their mitochondria are slightly depolarised i.e. $\Delta\Psi_m$ is more positive so less dye is accumulated.

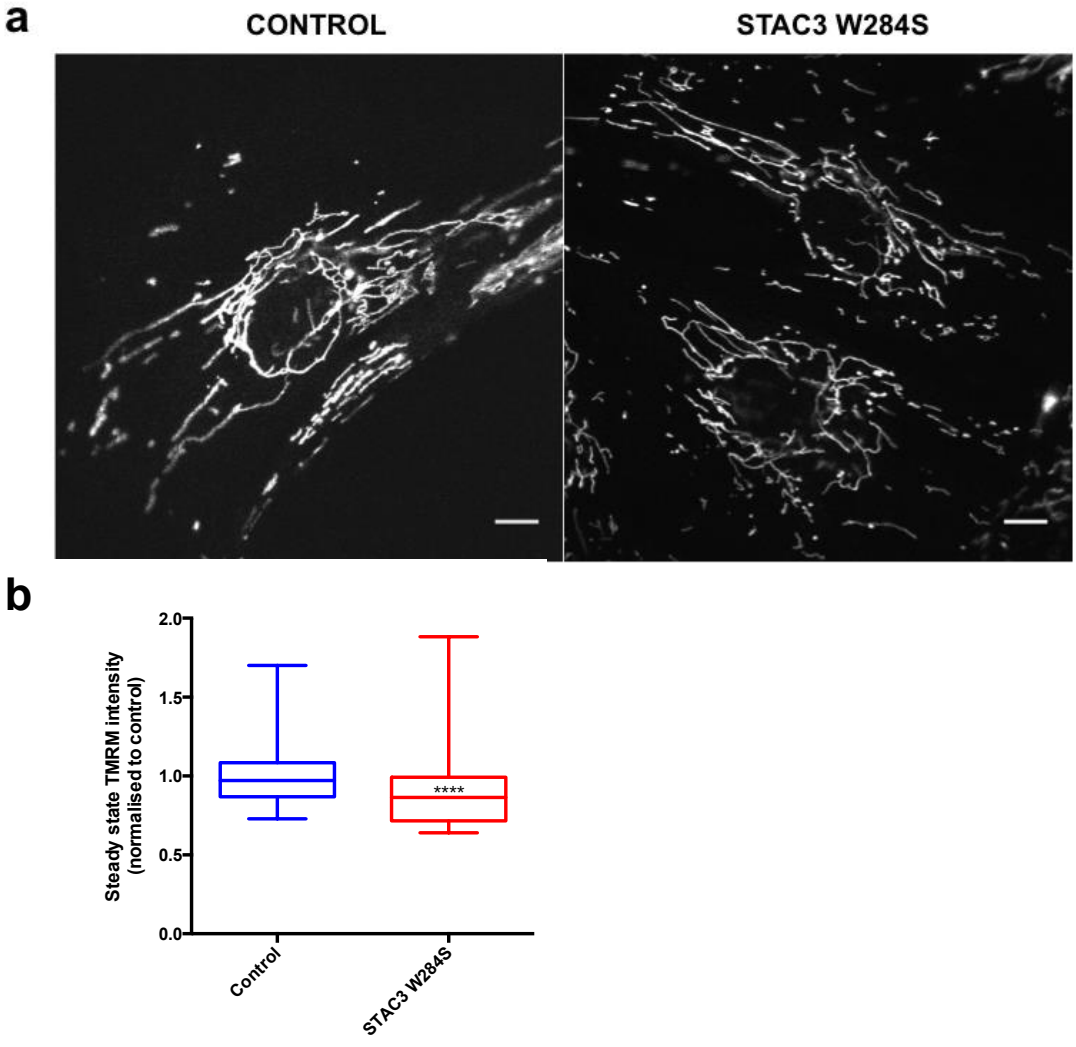

Figure 3.4: Mitochondrial depolarisation in resting STAC3 W284S fibroblasts

Representative confocal images of TMRM staining in control and STAC3 W284S fibroblasts (a). Average TMRM intensity was quantified and normalised to the mean control intensity (b). n>118 cells from 3 independent experiments. Scale bars 10µm.

3.3.3 Mitochondrial O_2 consumption is unchanged in STAC3 W284S fibroblasts

As $\Delta\Psi_m$ is crucial for maintaining the physiological function of the electron transport chain, high-resolution respirometry measurements were carried out. No significant differences were observed in mitochondrial O_2 consumption in the resting (P=0.946), leak (P=0.499) and maximal states (P=0.352) (Figure 3.5).

	Basal			Leak			Maximal		
Control	31.8	33.2	28.7	3.5	5.2	3.5	-	62.2	54.0
STAC3 W284S	36.2	29.2	28.8	2.6	4.3	3.7	-	62.0	64.4

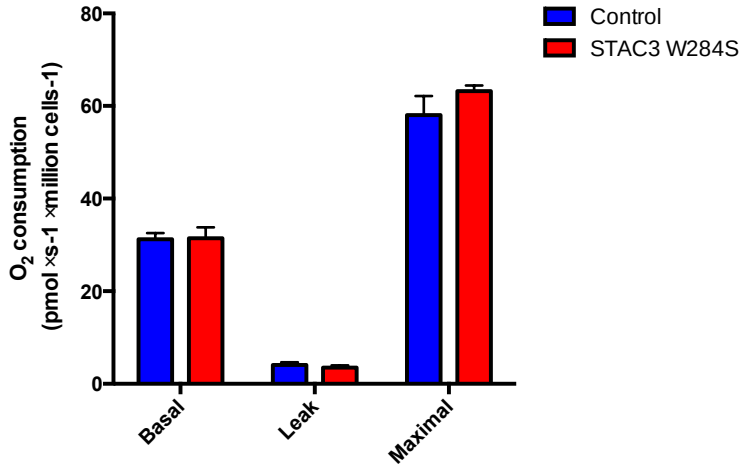

Figure 3.5: Mitochondrial O_2 consumption in STAC3 W284S cells is similar to controls

O_2 consumption of intact cells in the basal state, leak state (2.5μM oligomycin present) and maximal state (1μM FCCP present) were measured using high-resolution respirometry (see Figure 3.1 for example measurement). Raw measurements (pmol s^{-1} million $cells^{-1}$) from each experimental day are shown in the table. The mean averages of these measurements are shown in the bar graph (error bars SEM). n=3 independent experiments (except for maximal measurements, where n=2 as one experiment was prematurely terminated by addition of FCCP that may have been contaminated with Antimycin A).

3.4 Discussion

In this chapter I have characterised Ca^{2+} homeostasis and mitochondrial function in fibroblasts from an individual with a mutation in STAC3, with the intention of providing preliminary data for a future project using fibroblast-derived myotubes. STAC3 is a relatively new player in the regulation of EC coupling but its association with Native American Myopathy, and now KDS and core myopathy, highlight its importance in skeletal muscle health. While it may not be surprising that a defect in EC coupling results in muscle disease, it is interesting to see that a mutation in STAC3, like RYR1, can have an effect on the mitochondria that leads to core formation.

3.4.1 Ca^{2+} homeostasis in STAC3 W284S fibroblasts

While resting cytosolic Ca^{2+} levels were similar to controls, histamine-induced Ca^{2+} release was significantly higher in the STAC3 W284S fibroblasts. This suggests that, despite STAC3 being predominantly expressed in skeletal muscle, its physiological function may be important for Ca^{2+} regulation across the body. Although it is difficult to envisage a physiological purpose for communication between the skin and skeletal muscle, Ca^{2+} waves can propagate between dissimilar cell types (Sanderson et al. 1994), so perhaps the primary Ca^{2+} defect in skeletal muscle has caused compensatory changes in Ca^{2+} regulation in the skin. It will be interesting to see whether Ca^{2+} signals produced by future myotube models compare to my results from the fibroblast precursors, or whether they recapitulate the reduced skeletal muscle Ca^{2+} transients observed in the STAC3 W284S zebrafish model (Horstick et al. 2013).

3.4.2 Mitochondrial function in STAC3 W284S fibroblasts

Confocal imaging with TMRM showed that the mitochondrial population was slightly depolarised in the STAC3 W284S fibroblasts. As mitochondrial Ca^{2+} uptake is driven by the $\Delta\Psi_m$, depolarisation may reduce the Ca^{2+} buffering ability of the mitochondria, giving a possible explanation for the increased

cytosolic Ca^{2+} transients observed upon histamine stimulation. Due to limited time and resources, I did not investigate mitochondrial Ca^{2+} uptake in the fibroblasts but this is something that should be measured in future myotube models using either genetically engineered Ca^{2+} indicators (Hill et al. 2014), or cationic dyes such as rhod-2 AM (Davidson & Duchen 2012). If mitochondrial depolarisation were also observed in STAC3 W284S myotubes, then I would expect to see a reduction in mitochondrial Ca^{2+} accumulation. This could result in a metabolic deficit, which would significantly contribute to the muscle weakness experienced by the patient.

Respirometry measurements showed that the STAC3 W284S cells behaved similarly to controls in terms of basal, leak or maximal mitochondrial O_2 consumption. This was surprising as I expected mitochondrial depolarisation to mean one of two things: more proton leak from the matrix i.e. increased O_2 consumption under the oligomycin-induced leak state, or a lack of proton pumping from the matrix to the IMS i.e. a reduction in the activity of respiratory chain complexes and a reduction in overall O_2 consumption. Again due to time limitations, I could not investigate this discrepancy further but these measurements should certainly be repeated in future myotube models. As mitochondrial depolarisation can signify respiratory chain inhibition and ATP depletion, assays for ATP production and OXPHOS complex activity should also be carried out.

3.4.3 Expression of STAC3 in fibroblasts

The first published study on STAC3 showed that it is abundant in the skin as well as fast and slow-twitch muscles of Atlantic salmon (Bower et al. 2012). Although subsequent studies have not tested STAC3 expression in the skin, they show that STAC3 is predominantly expressed in skeletal muscle (Reinholt et al. 2013; Horstick et al. 2013; Nelson et al. 2013; Zhang et al. 2014). Recently it has been shown that STAC3 is required for efficient membrane trafficking of the muscle-specific $Ca_V1.1$ subunit of the DHPR (Polster et al. 2015); this again suggests that STAC3 is a skeletal muscle specific isoform.

Being the only available model at the time, skin fibroblasts were selected for these experiments with the aim of providing preliminary data towards a longer project using MyoD-transduced or iPSC-derived myotubes. It is useful to know the properties of fibroblasts before converting them into a muscle model and to see how Ca^{2+} signalling changes specifically with differentiation. However, with hindsight, whether STAC3 is expressed in this fibroblast model should have been determined prior to characterisation. This would help to confirm whether the changes in Ca^{2+} signalling and mitochondrial function I have observed are actually due to the mutation in STAC3. Without this knowledge, it is difficult to interpret my results; the observed differences may have been due to genetic variation between individual patient donors, rather than the STAC3 mutation.

3.4.4 Developing a skeletal muscle model

To fully understand the pathological consequences of the STAC3 W284S mutation, a skeletal muscle cell model needs to be established. To avoid the use of animals and also open up the possibility of a future therapy, it would be ideal to use cells derived from the patient himself. While it is possible to establish primary myoblast cell lines from patients with muscle disease (Mamchaoui et al. 2011), the process of obtaining a muscle biopsy is invasive and can be painful for the patient, particularly if the patient is a child (Skram et al. 2009). This particular patient also has a history of malignant hyperthermia, which increases the risk associated with anaesthetic procedures. If histopathological and biochemical analysis is also to be performed from one biopsy, the amount of muscle remaining for cell culture may be somewhat limited. Once isolated, primary skeletal muscle cells have a short proliferative lifespan and limited myogenic potential (Lauren Cornall 2012). Immortalisation can solve this problem, though it is important to adequately characterise an immortalised skeletal muscle cell line to ensure it replicates the physiology of the original tissue and retains the phenotypic traits of the donor cells (Lauren Cornall 2012).

Seeing as we already have fibroblasts from the patient, it might be better to convert them into skeletal muscle cells. One way to do this is to directly transform the fibroblasts into myoblasts by using a viral vector system to force the expression of the myogenic 'master switch', MyoD (Weintraub et al. 1989). If this approach was successful, it would be interesting to see if the W284S mutation has any effect on myogenic differentiation, as has been previously reported in KD studies (Bower et al. 2012; Ge et al. 2014). Another approach would be to revert the fibroblasts back to pluripotency, resulting in iPSCs that can then be differentiated to a skeletal muscle fate (Takahashi & Yamanaka 2006). The iPSCs could also be differentiated into neuronal cells, which might give an insight into why this patient also has learning difficulties. Once MyoD transduction or reprogramming has been carried out, it will be important to check that the resulting myogenic cells are fully differentiated and behave like mature muscle i.e. they express DHPR and RyR1 and can be stimulated to produce contractile Ca^{2+} transients.

Chapter 4 Exploring the physiological consequences of MICU1 deficiency in fibroblasts

4.1 Introduction

While the MCU KO mouse may lack an obvious phenotype, the physiological importance of mitochondrial Ca^{2+} handling has been highlighted by our discovery of the first human disease to be directly associated with dysfunctional mitochondrial Ca^{2+} uptake (Logan et al. 2014). In collaboration with clinicians, we identified 15 individuals lacking in MICU1 who presented with a novel brain and muscle disorder as infants or young children. Characteristic features included muscle weakness, elevated serum creatine kinase levels, learning difficulties and progressive extrapyramidal motor disturbances (Logan et al. 2014). Features associated with mitochondrial disease were also reported in some cases, including ataxia, microcephaly, opthalmaplegia, ptosis, optic atrophy and axonal peripheral neuropathy. Available muscle biopsies showed myopathic features including clusters of regenerating fibres and minicores (Figure 4.1).

Figure removed due to copyright restrictions

Figure 4.1: Patients with mutations in MICU1 present with minicores

Quadriceps biopsy from a patient at 10.7 years of age stained with NADH tetrazolium reductase (blue). Minicores are indicated with arrows. Scale bar 50μm. Adapted from (Logan et al. 2014).

While 11 individuals from 5 UK families had a splice acceptor site mutation, c.1078-1G>C, the remaining 4 individuals from 2 unrelated Dutch families had a different homozygous mutation affecting a splice donor site, c.741+1G>A (Logan et al. 2014). Sequencing of cDNA from the 15 subjects revealed intronic insertions causing frameshifts, which resulted in a significant loss of MICU1 mRNA and a complete loss of the protein.

In line with the objectives set out in 1.6, the aim of this chapter is to characterise intracellular Ca^{2+} homeostasis and mitochondrial function in primary fibroblast cell lines derived from two unrelated teenagers carrying the c.1078-1G>C mutation (hereafter referred to as ΔMICU1). This will give an insight into the physiological consequences of the absence of MICU1, which will also help to understand the core myopathy pathology in these patients. While some of the data in this chapter has been published (Logan et al. 2014), the rest of the dataset shows the follow-up project.

4.2 Methods

4.2.1 Chemicals

All chemicals were purchased from Sigma unless otherwise stated.

4.2.2 Cell culture

Primary human fibroblasts were obtained from the MRC Centre for Neuromuscular Disease Biobank, London. Two control samples with no known neuromuscular disease were age-matched to two ΔMICU1 patients. Fibroblasts were cultured in high glucose (4.5g/L) DMEM with Glutamax, supplemented with 10% FBS, 50 units/mL penicillin and 50µg/mL streptomycin (hereafter referred to as 1% PS) (all from Invitrogen). Where galactose conditions are indicated, fibroblasts were cultured in zero glucose DMEM with L-glutamine (Invitrogen), 10% FBS (Invitrogen), 1mM sodium pyruvate (Sigma), 0.1% w/v (5.5mM) galactose (MP Biomedicals) and 1% PS (Invitrogen).

4.2.3 Mitochondrial Ca^{2+} measurements with aequorin

Fibroblasts were seeded in white 96 well plates (50,000 cells/well) and transduced for 48hrs with an adenovirus expressing mitochondria-targeted luminescent aequorin (mtAEQ) under cytomegalovirus (CMV) control (Ainscow & Rutter 2001). The mAEQ adenoviral construct was produced using the AdEasy system (Stratagene) by Professor Guy Rutter (Imperial College London). Prior to assay, cells were reconstituted with 5µM coelenterazine (Invitrogen) for 2hrs at 37°C. Mitochondrial signals induced by 10µM histamine were measured in a plate reader (Fluostar Optima, BMG Labtech) using a luminescence optic with 3mm diameter light guide. Assays were carried out at 37°C. 1mM digitonin was used to generate a saturating concentration of Ca^{2+} inside the cells and thus give the maximum light intensity. Luminescence values were converted into Ca^{2+} concentration with

a mathematical algorithm that uses the maximum light intensity value and parameters based on the affinity of the aequorin used (Brini et al. 1995).

4.2.4 Measurements of resting $\Delta\Psi_m$

Fibroblasts plated on 22mm glass coverslips were equilibrated with RB containing 25nM TMRM for 15 mins at 37°C. Confocal z stacks were then acquired on a Zeiss 700 CLSM using a 40x oil objective and a 37°C stage. RB containing only 25nM TMRM was present throughout imaging. Fluorescence was excited at 555nm and measured at >560nm.

ImageJ was used for image analysis. Maximum intensity projections were used for quantification to avoid bias in the focal plane. ROIs were drawn around individual cells and images were thresholded to quantify the mean of mitochondria-localised signal intensities within each cell. Identical acquisition settings and threshold values were used in repeat experiments.

4.2.5 Cytosolic Ca^{2+} measurements of cell populations

Fibroblasts were seeded in black 96 well plates (50,000 cells/well) and loaded with RB containing 5μM Fluo-4 AM, 0.002% pluronic acid and 1mM probenecid for 30mins at RT. For measurements of histamine-evoked Ca^{2+} release, cells were washed with RB, pre-treated with 0.1% DMSO or 1μM FCCP (to eradicate mitochondrial Ca^{2+} uptake) for 10mins and then assayed at 37°C on a plate reader (Fluostar Optima, BMG Labtech) using fluorescence optics and light guide with 485BP12 excitation and Em520 emission filters. 10μM histamine was injected to induce a cytoplasmic Ca^{2+} signal followed by 2μM ionomycin, which provided a maximum fluorescence reading. To assess intracellular Ca^{2+} store content, a similar plate reader set up was used but cells were present in Ca^{2+} free RB supplemented with 200μM EGTA and 2μM ionomycin was injected.

Background (measured in an empty well with RB) corrected fluorescence intensities were calibrated into Ca^{2+} concentration using the following equation (Maravall et al. 2000):

$$[Ca^{2+}] = K_d \times (F / F_{max} - 1/R_f) / (1 - F/F_{max})$$

Where K_d = 350nM, F_{max} is the maximum fluorescence after ionomycin application, R_f = 100. *F* is fluorescence as measured in these experiments.

4.2.6 Confocal imaging of mitochondrial Ca^{2+} levels

Cells plated on 22mm glass coverslips were loaded with RB containing 5μM rhod-2 AM or rhod-FF AM (both Molecular Probes) and 0.002% pluronic acid. Images were acquired on a Zeiss 700 CLSM (excitation at 555nm, emission at >560nm) using a 40x objective and a 37°C stage.

ImageJ was used for image analysis. ROIs were drawn around individual cells and images were thresholded to quantify the mean of mitochondria-localised signal intensities within each cell. Identical acquisition settings and threshold values were used in repeat experiments.

4.2.7 High content imaging of basal mitochondrial Ca^{2+} levels

Control and ΔMICU1 cells were seeded in 96 well imaging plates (BD Biosciences) and transduced for 4hrs with an adenovirus expressing wild type (WT) MICU1-HA and GFP (gift from Rizzuto lab, Padua). The following day cells were loaded in RB with rhod-2 AM (5μM; 30min at RT and then replaced with dye free RB), and 2μg/mL Hoecsht 33342 (present throughout) to label nuclei for cell counting. Cells were imaged on an ImageXpress Micro XL high-content imaging system (Molecular Devices) using a custom protocol to image three wavelengths (Lumencor solid-state illumination with Semrock (Brightline) filters (nm) ex377/50 em447/60 for Hoechst 33342, ex472/30 em520/35 nm for GFP, and ex531/40 em593/40 for detection of Rhod-2). Nine fields per well were imaged using a 40x objective, binning 1 (full resolution) with a Complementary Metal-Oxide Semiconductor (CMOS)

detector. Acquisition was performed using MetaXpress software (Molecular Devices) and analysis was carried out using the proprietary Multi-Wavelength Scoring Application Module within this software. The Hoecsht signal was used to create a nuclear mask and thus allow cell identification, while the GFP signal was used to create a green cytosolic mask (Figure 4.2). Green areas larger than 400μm^2 that also possessed a nucleus were scored as GFP-positive cells (Figure 4.2). The rhod-2 signal was separated into nuclear and cytosolic signals, with the nuclear signal being assumed to represent pure cytosolic signal with minimal mitochondrial interference. A ratio between the two was then used to detect specific mitochondrial signal. Outliers resulting from imaging artefacts were excluded by applying a maximum threshold for rhod-2 intensities.

Figure removed due to copyright restrictions

Figure 4.2: High-throughput analysis of the effect of MICU1 expression on basal [Ca^{2+}]$_m$

Demonstration of the workflow of the Multi-Wavelength Scoring Application Module, which was used to quantify basal mitochondrial rhod-2 intensities in cells infected with adenovirus expressing WT MICU1-GFP. Adapted from (Logan et al. 2014).

4.2.8 Rates of cellular ROS production

Cells were imaged in the presence of 5μM dihydroethidium (DHE) (Molecular Probes) on a Zeiss 510 UV-VIS CSLM using a 40x objective and a 37°C stage. Blue fluorescence of the reduced form of DHE was excited at 351nm and emission detected between 435-485nm. Oxidised DHE was excited at 543nm and emission detected >560nm. After background subtraction, a ratio of oxidised / reduced DHE fluorescence was calculated and the rate of change in this ratio was interpreted as the rate of ROS production. The first minute of measurements were excluded to allow for loading of the dye.

4.2.9 Western blotting

Following relevant drug treatment and/or media changes, fibroblasts were washed with PBS, scraped and centrifuged. Cell pellets were then lysed in RIPA buffer (150mM NaCl, 0.5% sodium deoxycholic acid, 0.1% SDS, 1% Triton X-100, 50mM Tris pH8, 1mM PMSF, PhosSTOP phosphatase inhibitors (Roche)) for 30 mins on ice. Samples were subsequently centrifuged at 16,000g at 4'C and protein concentrations determined using Pierce BCA assay (Thermo Scientific).

40μg of protein was boiled at 95°C for 5 mins in NuPAGE 4X LDS sample buffer (Invitrogen) containing 5% β-mercapethanol. Proteins were separated using 4-12% NuPAGE Bis-Tris gels (Invitrogen) with MOPS running buffer (Invitrogen) and transferred onto nitrocellulose membranes using NuPAGE transfer buffer (Invitrogen) supplemented with 20% methanol. Membranes were washed with TBS-T and blocked with 3% BSA in TBS-T for 1 hr at RT, before being incubated with primary antibody solution overnight at 4°C. Following 3 x 10 min washes in TBS-T, membranes were incubated with secondary antibody solution for 1-1.5 hours at RT. After 3 x 5 min washes in

TBS-T, the membranes were developed using Amersham ECL reagent (GE Healthcare) and imaged with a ChemiDoc system (BioRad).

Densitometry analysis was carried out using ImageJ.

Primary antibodies used were anti-DRP1 (mouse, Abcam; 1:1000), anti-phospho DRP1 (Ser637) (rabbit, NEB; 1:1000), anti-LC3b (rabbit, Cell Signaling; 1:2000), anti-β-actin (mouse, Santa Cruz; 1:2000), anti-PDH E1α (mouse, Invitrogen; 1:1000) and anti-phospho PDH E1α (Ser293) (rabbit, Novus Biologicals; 1:1000). Secondary antibodies used were anti-mouse and anti-rabbit (both from Thermo Scientific and diluted 1:4000).

4.2.10 PDH phosphorylation state

To minimise variability relating to substrate supply, protein samples were made approximately 2hrs after refreshing the culture media. Culture plates were also snap frozen at -80°C before scraping to minimise any subsequent kinase and phosphatase activity. Western blotting for phosphorylated PDH (pPDH) was carried out first and then the same membrane was washed and re-probed overnight for total PDH. The proportion of pPDH was then expressed as average intensity of pPDH band / average intensity of total PDH band.

4.2.11 Respirometry of intact cells

Cells were trypsinised and resuspended at 1 million cells/mL in DMEM buffered with 20mM HEPES, supplemented with 5.5mM glucose (or 5.5mM galactose for galactose-grown cells), 2mM glutamine and 1mM pyruvate. Respiration rates were measured at 37°C with the High-Resolution Oxygraph (Oroboros Oxygraph-2k). Once resting rate had stabilised, 10μM histamine was added to induce a Ca^{2+}-dependent rise in O_2 consumption. After returning to resting rate, 2.5μM oligomycin A was added to measure leak respiration, 1μM FCCP to determine maximal oxidative capacity and 2.5μM antimycin A to measure non-mitochondrial (background) O_2 consumption.

Each of these respiratory states was defined as the average value over a user-defined region of stabilised signal (for example see Figure 3.1).

4.2.12 ATP luminescence measurements

Cells were seeded in white 96 well plates (20,000 cells / well) and the next day were incubated with one of the following treatments for 1hr at 37°C: 1uL/mL DMSO, 5μM oligomycin A, 1mM iodoacetic acid (IAA), 10μM CGP-37157 or 10mM 2-deoxyglucose (DG). The cells were allowed to come to RT before incubating with CellTiter-Glo® Reagent (Promega) for 10mins. Luminescence values proportional to ATP content were measured in a plate reader (Fluostar Optima, BMG Labtech) using a luminescence optic with 3mm diameter light guide.

4.2.13 Mitochondrial morphology scoring

Mitochondrial morphology was assessed by eye using images collected from TMRM and Rhod-2 imaging (see 4.3.10). Cells in which <50% of mitochondria were elongated were scored as cells containing fragmented mitochondria.

4.2.14 Measurements of single cell cytoplasmic Ca^{2+} transients

Spontaneous cytoplasmic Ca^{2+} transients were measured by loading cells with 5μM fluo-4 AM (Molecular Probes) for 25min at RT before washing with RB and imaging (excitation at 488nm, emission at >520nm) on a Zeiss 700 CLSM. After 10min, 1μM FCCP was added to eradicate mitochondrial Ca^{2+} uptake. A spontaneous transient was defined as an increase in fluo-4 intensity that was at least 25% greater than baseline intensity. A cell showing at least one of these transients was scored as ‘spontaneously active’.

4.2.15 DRP1 phosphorylation state

Western blotting for phosphorylated DRP1 (pDRP1) was carried out first and then the same membrane was washed and re-probed overnight for total

DRP1. The proportion of pDRP1 was then expressed as average intensity of pDRP1 band / average intensity of total DRP1 doublet.

4.2.16 Assessing autophagy flux

1hr after the culture media was refreshed, fibroblasts were treated with 1uL/mL DMSO or 100nM Bafilomycin A1 for 5 hrs at 37°C. Samples were then processed for western blotting as in 4.2.9 and probed for LC3 expression.

4.2.17 Statistics

Data for both control cell lines was pooled together and compared with similarly pooled data for both ΔMICU1 cell lines. Values are presented as mean ± standard error. N numbers indicate number of independent repeat experiments unless otherwise indicated.

Statistical analysis was performed using Prism 6 (GraphPad software). Where the means of two independent groups were being compared e.g. control group v ΔMICU1 group, unpaired two tail t-tests were applied to test significance to a P value of 0.05. Where the means of three or more independent groups were being compared, one-way analysis of variance (ANOVA) was used. When the effect of two different independent variables was being measured e.g. cell line and drug treatment, two-way ANOVA was used. I considered using repeated measures ANOVA for repeated measurements on the same cell line but decided it was unsuitable as my measurements were never conducted on exactly the same sample of cells i.e. the passage number varied between experiments or the cells were grown in different tissue culture plates. If the same sample of cells had been measured multiple times e.g. in a time course experiment then repeated measures testing would be more appropriate.

When several comparisons between groups were being made, *post hoc* Tukey tests were used to correct for multiple testing.

4.3 Results

4.3.1 Loss of MICU1 leads to accelerated mitochondrial Ca^{2+} uptake

Given the gatekeeping role of MICU1 in mitochondrial Ca^{2+} uptake, my first question was to find out what effect the loss of MICU1 had on mitochondrial Ca^{2+} levels in response to a physiological cytosolic Ca^{2+} rise (induced by histamine, an agonist that triggers IP_3-mediated Ca^{2+} release from internal stores). Control and ΔMICU1 fibroblasts were transduced with an adenovirus encoding for mitochondrial-targeted aequorin (mtAEQ), a Ca^{2+} sensitive photoprotein that can be used to measure matrix Ca^{2+} concentrations in intact cells. Stimulating the mtAEQ-expressing cells with 10μM histamine (Figure 4.3a) showed no significant difference in peak $[Ca^{2+}]_m$ (P=0.616)(Figure 4.3b) but the half time to peak was significantly reduced in the ΔMICU1 cells (2.57 ± 0.132 secs) compared to controls (3.097 ± 0.162 secs) (P=0.030) (Fig 4.3c). Similarly with 50μM histamine, the half time to peak was significantly reduced in the ΔMICU1 cells (2.03 ± 0.049 secs) compared to controls (2.45 ± 0.184 secs) (P=0.0492)(Figure 4.3c) but there was no significant change in peak $[Ca^{2+}]_m$ (P=0.858)(Figure 4.3b).

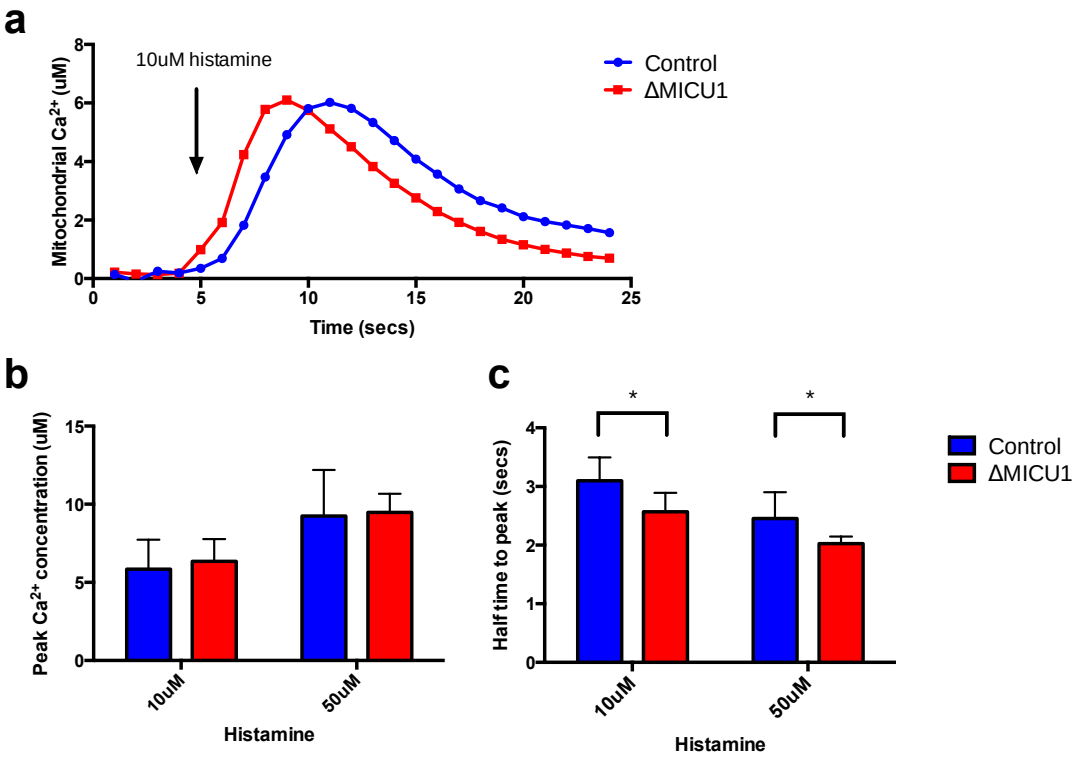

Figure 4.3: ΔMICU1 cells show a significantly faster rate of rise in $[Ca^{2+}]_m$

Representative traces of mtAEQ measurements of cell populations (50,000 cells per well of a 96 well plate) (a). Maximum matrix concentrations in response to 10μM and 50μM histamine were quantified (b). The rate of mitochondrial Ca^{2+} uptake (c) was calculated as the time taken to reach half the maximal concentration i.e. the half time to peak. n=6 replicates pooled from both cell lines (2 control and 2 ΔMICU1 cell lines were measured on 3 experimental days). At least 3 wells were measured per cell line per day. Therefore values shown are mean of means for each replicate. Errors bars show SEM.

4.3.2 Accelerated mitochondrial Ca^{2+} uptake in the ΔMICU1 cells was not due to altered $\Delta\Psi_m$ or intracellular Ca^{2+} store content

As well as being a key determinant of respiratory chain activity, $\Delta\Psi_m$ is the driving force for mitochondrial Ca^{2+} uptake. To see if an increase in $\Delta\Psi_m$ was responsible for the accelerated uptake observed with mtAEQ, control and ΔMICU1 cells were imaged in the presence of TMRM. Quantification of average steady state TMRM intensity, however, showed no significant difference in $\Delta\Psi_m$ between control and ΔMICU1 cells (P=0.370) (Figure 4.4a).

Another factor that could influence mitochondrial Ca^{2+} uptake is the amount of Ca^{2+} stored in the ER. Mitochondria tend to localise at Ca^{2+} release sites of the ER, so if the loss of MICU1 somehow caused an increase in ER store Ca^{2+}, the mitochondria could be exposed to higher Ca^{2+} fluxes during store release and thus exhibit altered uptake kinetics. ER store content can be measured using the SERCA inhibitor, thapsigargin, which prevents Ca^{2+} pumping into the ER and so causes ER depletion. Unfortunately, thapsigargin did not seem to be a reliable stimulus in my cytosolic Ca^{2+} plate reader assays (outlined in 4.2.5). Instead I decided to use ionomycin, which non-specifically triggers release from intracellular Ca^{2+} stores. This showed that there was no significant difference (P=0.0739) in intracellular Ca^{2+} content between control (3.627 ± 0.4893) and ΔMICU1 cells (4.610 ± 0.2714) (Figure 4.4b). However it is worth keeping in mind that ionomycin is a potent ionophore, which can also affect the mitochondria (Abramov & Duchen 2003).

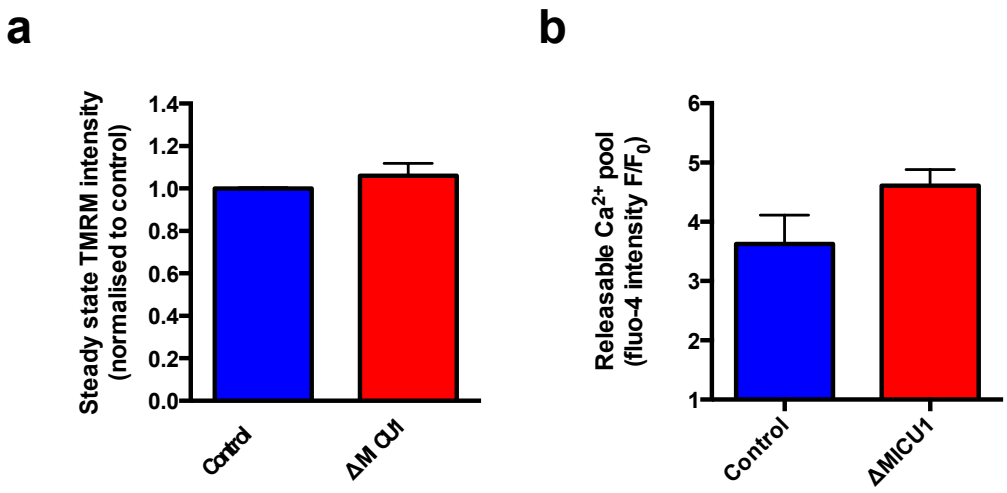

Figure 4.4: Accelerated mitochondrial Ca^{2+} uptake was not due to altered mitochondrial membrane potential or intracellular Ca^{2+} store content

Average TMRM fluorescence of ΔMICU1 fibroblasts was normalised to control average on each experimental day (a). n=6 replicates pooled from both cell lines (2 control and 2 ΔMICU1 cell lines were measured on 3 experimental days). At least 37 cells were measured per cell line per day. Therefore values shown are mean of means for each replicate. Errors bars show SEM.

Intracellular Ca^{2+} store content was measured in fluo-4 loaded cell populations (50,000 cells per well of a 96 well plate) (b). Maximum fluo-4 fluorescence after 2μM ionomycin application was normalised to resting fluorescence and used to signify intracellular Ca^{2+} store content. n ≥ 9 wells measured over 3 experimental days. Therefore values shown are the mean of all wells measured. Error bars show SEM.

4.3.3 Loss of MICU1 results in reduced cytoplasmic Ca^{2+} signals and increased mitochondrial Ca^{2+} buffering

Since mitochondria buffer cytoplasmic Ca^{2+} signals, the magnitude of a rise in $[Ca^{2+}]_c$ can influence mitochondrial Ca^{2+} uptake. To measure the characteristics of agonist-induced cytosolic Ca^{2+} signals, populations of fluo-4 loaded cells were stimulated with 10μM histamine in a plate reader assay (Figure 4.5a). This showed that peak cytoplasmic Ca^{2+} concentration was significantly reduced in the ΔMICU1 cells (786.3 ± 89.73 nM) compared to controls (1104 ± 81.13 nM) (P=0.0203) (Figure 4.5b). This was likely to be due to increased mitochondrial buffering, since pre-treating the cells with FCCP, an uncoupler that prevents mitochondrial Ca^{2+} uptake, prevented this effect (P=0.862) (Figure 4.5c).

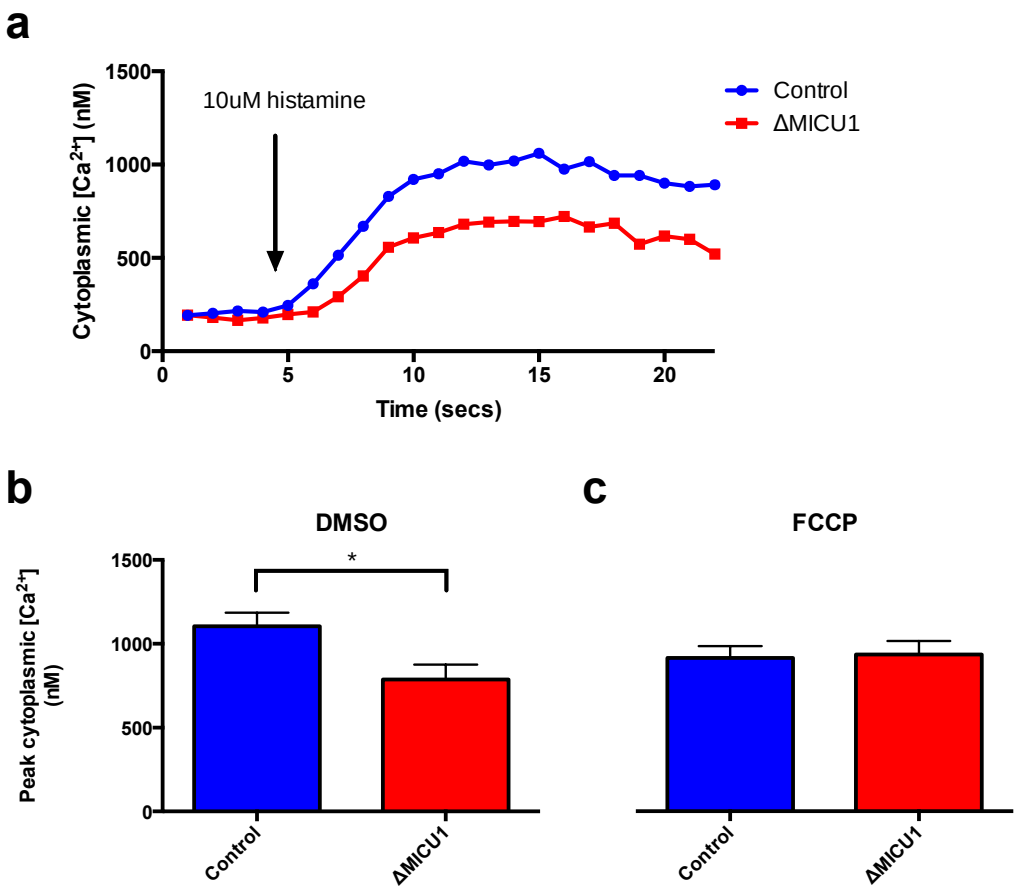

Figure 4.5: ΔMICU1 cells have increased mitochondrial buffering capacity

Representative traces of cytosolic Ca^{2+} measurements of fluo-4 loaded cell populations incubated with DMSO as a control treatment (a). Maximum cytoplasmic Ca^{2+} concentrations in response to 10μM histamine were quantified in DMSO-

treated (a) and FCCP-treated cells (b). n ≥ 9 independent wells measured over 3 experimental days. Values shown are the mean of all wells measured. Error bars show SEM.

4.3.4 The loss of MICU1 leads to chronic activation of the MCU at resting cytosolic Ca^{2+} concentrations

To find out what effect the absence of MICU1 had on basal mitochondrial Ca^{2+} levels, control and ΔMICU1 fibroblasts were labelled with rhod-2 AM, a Ca^{2+} indicator that partitions between the cytosol and the mitochondria in response to $\Delta\Psi_m$ due to the net positive charge of the AM ester. Rhod-2 fluorescence is uniform across the cell (Figure 4.6A) until intracellular Ca^{2+} flux is stimulated. In resting ΔMICU1 cells, the fluorescent signal was bright in the mitochondria, even before stimulation (Figure 4.6B). This is consistent with the gatekeeping function of the protein and shows that mitochondrial Ca^{2+} concentrations at rest are elevated in the absence of MICU1.

Figure removed due to copyright restrictions

Figure 4.6: A loss of MICU1 caused mitochondrial Ca^{2+} loading at rest

Representative confocal image of rhod-2 labelled control (A) and ΔMICU1 (B) fibroblasts. Scale bar 20μm.

To verify that this phenotype was due to the lack of MICU1, the WT protein was re-expressed in the ΔMICU1 cells; subsequent rhod-2 imaging showed that this caused a small but significant reduction in mitochondrial Ca^{2+} content (Figure 4.7). Interestingly, this reduction was also observed in control cells in which MICU1 was overexpressed, suggesting that excessive expression of MICU1 can disturb mitochondrial Ca^{2+} homeostasis (Figure 4.7).

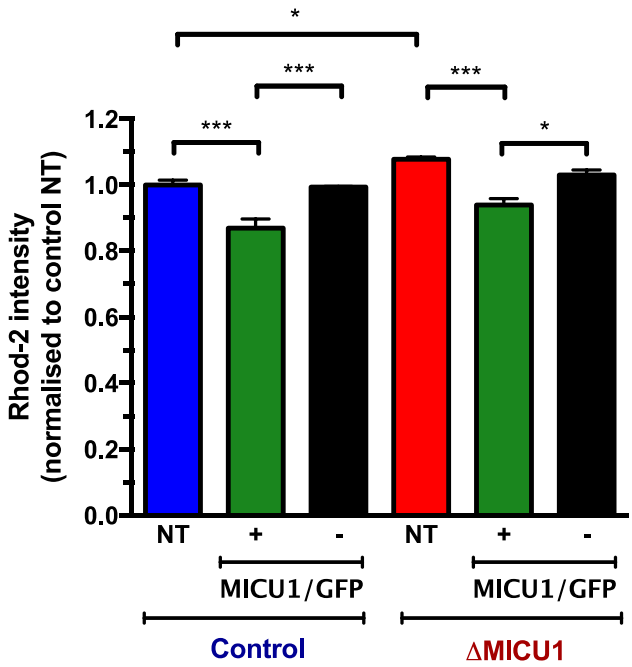

Figure 4.7: Overexpression of WT MICU1 caused a reduction in mitochondrial Ca^{2+} concentration

*Cells transduced with MICU1-GFP expressing adenovirus were loaded with rhod-2 and imaged using a high throughput imaging system (for analysis see section 4.2.7). Values are normalized to the average mitochondrial rhod-2 signal of non-transduced control cells. NT = Non-transduced i.e. no viral treatment, + = positively transduced i.e. GFP expressing, - = not successfully transduced i.e. no GFP expression. n=4 independent wells on the same imaging plate. For comparison of means one-way ANOVA with post hoc Tukey tests were used. This gave the following adjusted P values: Control NT vs ΔMICU1 NT (*P=0.0343), Control NT vs Control + (***P=0.0003), Control – vs Control + (***P=0.0005), ΔMICU1 NT vs ΔMICU1 + (***P=0.0001), ΔMICU1 – vs ΔMICU1 + (*P=0.0118).*

4.3.5 The absence of MICU1 in fibroblasts does not affect cellular ROS production

MICU1 deficiency has previously been shown to result in $[Ca^{2+}]_m$-dependent ROS overproduction (Mallilankaraman, Doonan, et al. 2012; Hoffman et al. 2013). To assess whether MICU1 loss results in oxidative stress, control and ΔMICU1 fibroblasts were imaged in the presence of fluorescent superoxide indicator DHE and average rates of dye oxidation were calculated (Figure 4.8a). This showed no significant difference in the rate of ROS production between control and ΔMICU1 cells (P=0.466) (Figure 4.8b).

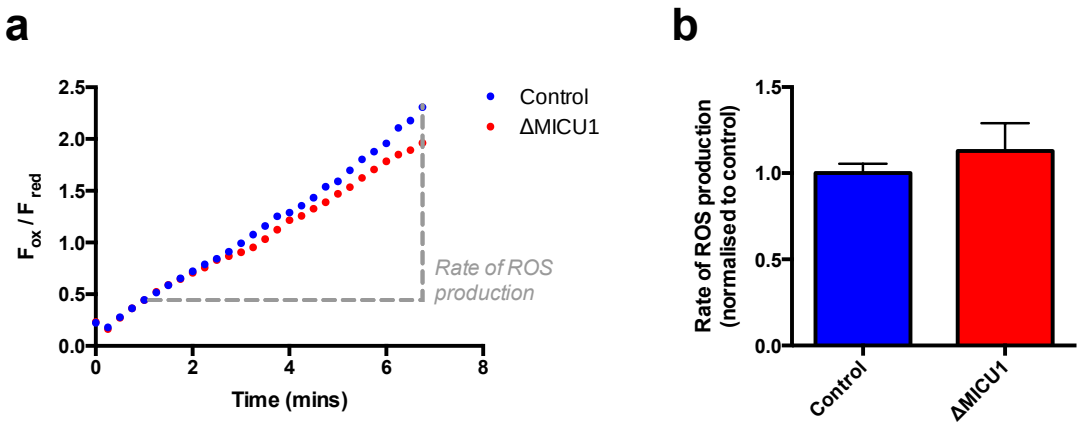

Figure 4.8: The effect of MICU1 loss on cellular ROS production

Representative trace of DHE oxidation in control and ΔMICU1 cells (a). F_{OX} indicates the blue fluorescence intensity emitted by oxidated DHE, while F_{RED} indicates the red fluorescence intensity emitted by reduced DHE. Rate of ROS production was calculated as the change in F_{OX} / F_{RED} over time (shown in grey). Average rates of ROS production were normalised to average control rate on each experimental day (b). n=6 replicates pooled from both cell lines (2 control and 2 ΔMICU1 cell lines were measured on 3 experimental days). At least 8 cells were measured per cell line per day. Therefore values shown are mean of means for each replicate. Errors bars show SEM.

4.3.6 The absence of MICU1 in glycolytic fibroblasts does not cause bioenergetic dysfunction

It is important to establish the bioenergetic consequences of altered MICU1 expression. Measuring O_2 consumption within intact cells can give an indication of electron transport chain functionality and cellular bioenergetics. As an increase in mitochondrial matrix Ca^{2+} concentration increases the supply of NADH and $FADH_2$ through citric acid cycle activation, one might expect to observe increased basal O_2 consumption in the ΔMICU1 fibroblasts. Measurements using a high-resolution respirometer, however, did not show any significant difference in basal mitochondrial O_2 consumption between control and ΔMICU1 cells (P=0.232) (Figure 4.9a). There were also no significant differences in average leak (P=0.267) or in maximal respiration values (P=0.210) (Figure 4.9a). Previous studies described a greater increase in O_2 consumption during stimulation of mitochondrial Ca^{2+} uptake in MICU1 KD cells than in controls (Mallilankaraman, Doonan, et al. 2012; Csordás et al. 2013). In contrast, my measurements showed that histamine-stimulated O_2 consumption was similar between control and ΔMICU1 cells (P=0.972) (Figure 4.9b).

To assess the impact of chronic mitochondrial Ca^{2+} loading on ATP production, ATP levels in control and ΔMICU1 fibroblasts were measured using a commercial luminescence assay kit. In keeping with the respirometry data, there was no significant difference in resting ATP levels between ΔMICU1 cells and controls (P=0.999) (Figure 4.9c). The lack of effect of treatment with complex V inhibitor, oligomycin, revealed that both control and ΔMICU1 fibroblasts do not rely on oxidative phosphorylation for ATP production (Control: DMSO v oligomycin P=0.999, ΔMICU1: DMSO v oligomycin P=0.999) (Figure 4.9c). Treatment with glyceraldehyde-3-phosphate dehydrogenase inhibitor, iodoacetic acid (IAA), caused a large reduction in ATP levels in both populations of cells, confirming that these fibroblasts make most of their ATP via glycolysis (Control: DMSO v IAA P<0.0001, ΔMICU1: DMSO v oligomycin P<0.0001) (Figure 4.9c).

Although it is clear from my respirometry data that these primary fibroblasts do respire aerobically, their basal rates of O_2 consumption were relatively low compared to their maximal capacities and treatment with ATP synthase inhibitor, oligomycin, had no effect on [ATP]. This suggests that mitochondrial oxidative phosphorylation in skin fibroblasts in culture plays a minimal role in energy homeostasis, which is not particularly useful when studying a mitochondrial protein that indirectly regulates mitochondrial metabolism. If these cells can be forced to use their mitochondria, perhaps a bioenergetic defect will be unveiled in the ΔMICU1 cells.

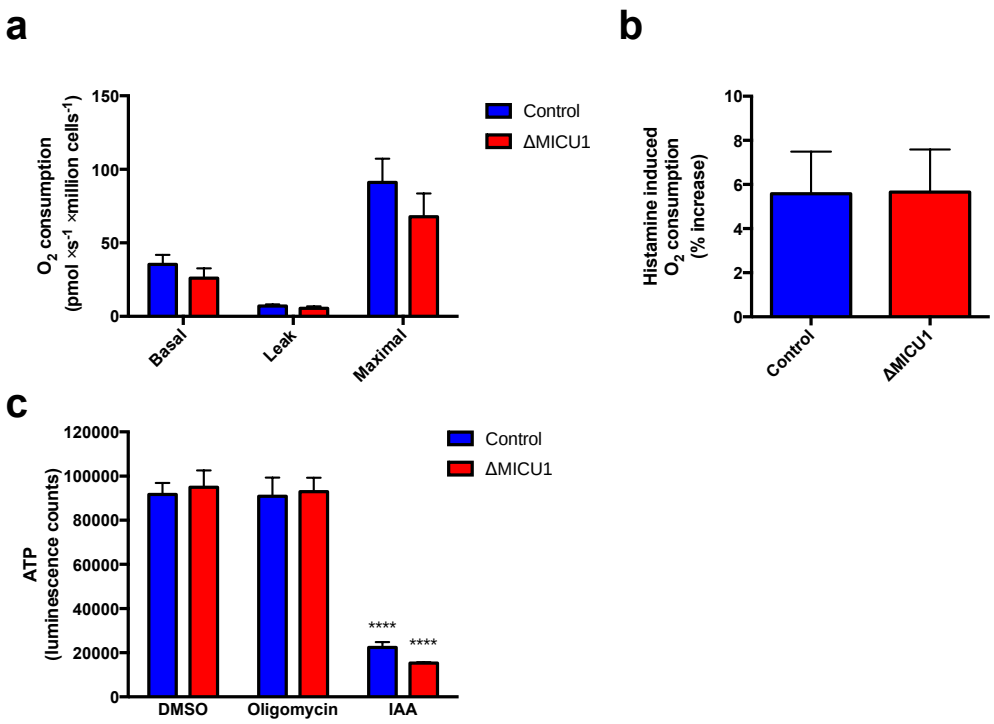

Figure 4.9: The effect of MICU1 loss on mitochondrial energy metabolism

O_2 consumption of intact control and ΔMICU1 cells in the basal state, leakage state (2.5μM oligomycin present) and maximal state (1μM FCCP present) were measured using high-resolution respirometry (a). The effect of 10μM histamine on basal respiration was also measured (b). Control and ΔMICU1 fibroblast populations were pre-treated with DMSO, 5μM oligomycin or 1mM IAA and processed via a commercial ATP assay kit, which gave a luminescence readout proportional to ATP content (c). n=6 replicates pooled from both cell lines (2 control and 2 ΔMICU1 cell lines were measured on 3 experimental days). Asterisks in (c) indicate statistical comparison with corresponding DMSO control. As two different variables (cell line and drug treatment) were being measured in (c), two-way ANOVA with post hoc Tukey tests were used.

4.3.7 ΔMICU1 fibroblasts cultured in galactose are more dependent on mitochondrial ATP production

One way to force cells to have an increased reliance on mitochondrial ATP production experimentally is to replace glucose with galactose in the culture medium. Galactose is metabolised into pyruvate via glycolysis, though at a much slower rate than its structural isomer, glucose (Robinson et al. 1992). As there are no catabolic processes to directly metabolise galactose, it is first converted to galactose-1-phosphate by galactokinase (Berg et al. 2002). Galactose-1-phosphate then acquires a uridyl group from uridine disphosphate (UDP) glucose, which is an intermediate in glycogen chain synthesis (Figure 4.10) (Berg et al. 2002). The resulting products are UDP-galactose, which is subsequently epimerised to regenerate UDP-glucose, and glucose-1-phosphate, which is isomerised by phosphoglucomutase to produce glycolytic intermediate glucose-6-phosphate (Figure 4.10).

Figure removed due to copyright restrictions

Figure 4.10: Generation of glucose-6-phosphate from galactose

Diagram reproduced from section 16.1.11 in (Berg et al. 2002).

The slow metabolism of galactose to glucose-1-phosphate is not sufficient for cells to produce the bulk of their ATP requirements by glycolysis (Robinson et al. 1992). This forces cells to switch to oxidative metabolism and to use glutamine as the major energy source (Reitzer et al. 1979). The immediate product of glutamine metabolism is glutamate, which can be converted to α-ketoglutarate by three different enzymes (Figure 4.11).

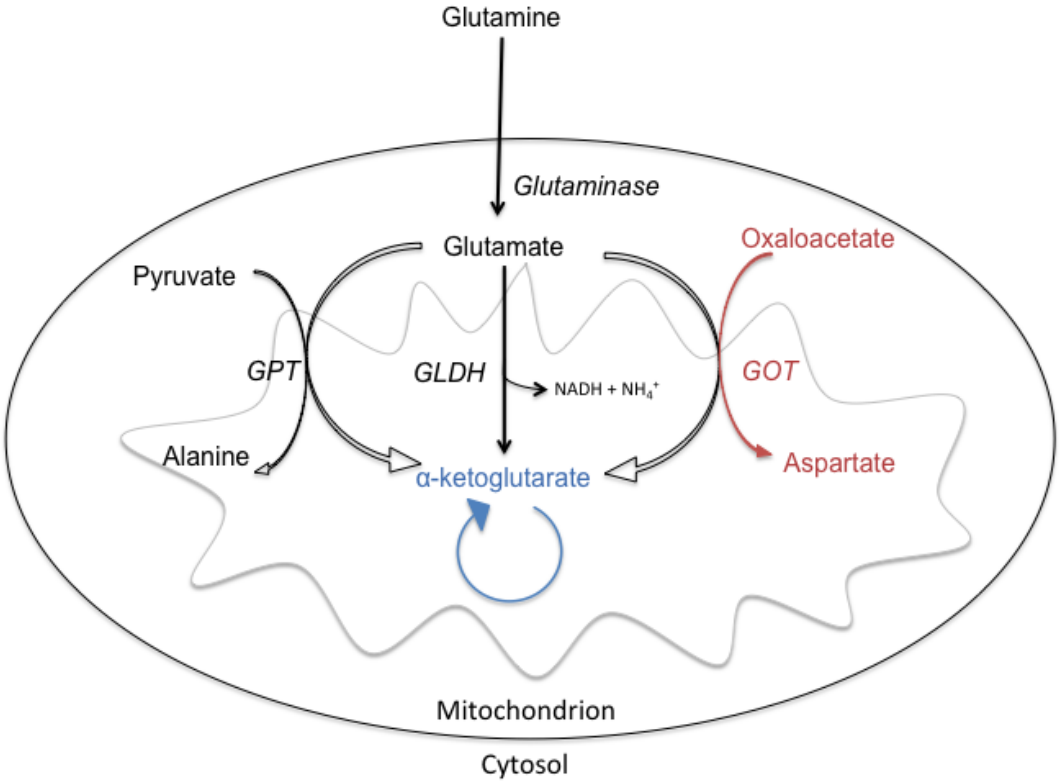

Figure 4.11: Glutaminolysis pathways

Glutaminolysis partly uses reaction steps from the citric acid cycle (blue) and the malate-aspartate shuttle (red). GLDH = Glutamate dehydrogenase, GOT = Glutamate oxaloacetate transaminase (also alanine transaminase), GPT = Glutamate pyruvate transaminase (also aspartate transaminase).

Different types of cells grown in galactose show a significantly higher O_2 consumption rate compared to cells grown in high glucose conditions (Rossignol 2004; Marroquin et al. 2007; Shulga et al. 2010; MacVicar & Lane 2014; Aguer et al. 2011). In addition, lower amounts of lactate and pyruvate accumulate in the media of galactose-grown cells, indicating that the majority of ATP production is from the mitochondrial oxidation of pyruvate and not

from glycolysis (Robinson 1996). The more aerobic state of galactose-grown cells is also thought to be due to changes in mitochondrial structure and an increase in mitochondrial oxidative capacity, as evidenced by increased OXPHOS protein expression and mitochondrial enzymatic activities (Rossignol 2004).

To verify that galactose growth conditions had resulted in a more oxidative phenotype, O_2 consumption was measured in control and ΔMICU1 fibroblasts that had been cultured in galactose for at least two weeks. Although galactose-cultured cells tended to show higher rates of O_2 consumption than glucose-grown cells, the differences were not statistically significant in either basal (Control: glucose v galactose P=0.717, ΔMICU1: glucose v galactose P=0.737), leak (Control: glucose v galactose P=0.998, ΔMICU1: glucose v galactose P=0.991), or maximal states (Control: glucose v galactose P=0.145, ΔMICU1: glucose v galactose P=0.0911) (Figure 4.12a). Despite this slight trend towards increased mitochondrial activity, the galactose-grown control and ΔMICU1 cells still behaved in a similar way as no significant differences could be detected in basal (P=0.836), leak (P=0.999) or maximal respiration values (P=0.302) (Figure 4.12a). Similar to previous glucose results, there was also no change in histamine-stimulated O_2 consumption between galactose-grown control and ΔMICU1 cells (P=0.875) (Figure 4.12b).

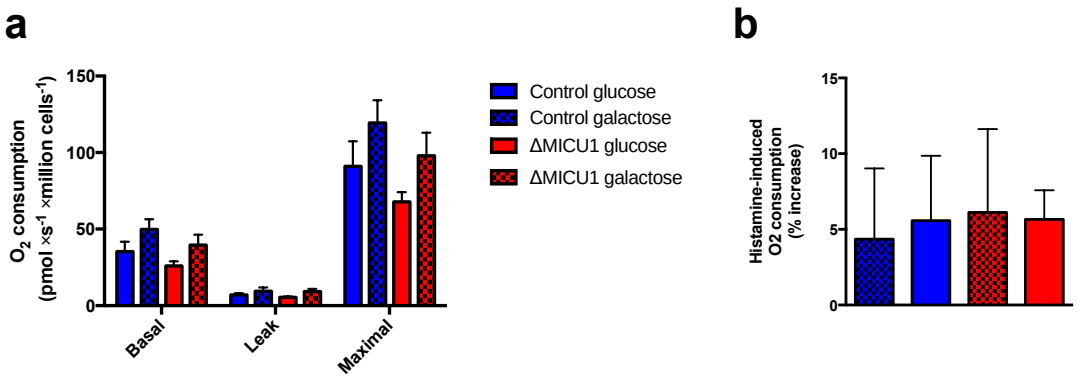

Figure 4.12: Mitochondrial O_2 consumption is normal in galactose-grown ΔMICU1 fibroblasts

High-resolution respirometry was used to measure O_2 consumption of glucose (unpatterned) or galactose (patterned) grown control (blue) and ΔMICU1 (red) cells in the basal state, leakage state (2.5μM oligomycin present) and maximal state

(1μM FCCP present) (a). The effect of 10μM histamine on basal respiration was also measured (b). Statistical differences were tested using two-way ANOVA with post hoc Tukey correction. n=6 replicates pooled from both cell lines (2 control and 2 ΔMICU1 cell lines were measured on 3 experimental days).

To assess whether galactose had successfully caused a metabolic shift from glycolytic to mitochondrial ATP production, ATP levels were analysed in galactose-grown cells treated with DMSO, oligomycin and IAA. Growth in galactose caused the ΔMICU1 cells to become more sensitive to oligomycin (***P<0.001), indicating that more mitochondrial ATP production was taking place than in glucose-grown ΔMICU1 cells (Figure 4.13a). A similar trend in increased oligomycin sensitivity was seen in the galactose-grown control cells, however, this was not significant (P=0.157) (Figure 4.13a). This suggests that, under oxidative conditions, ΔMICU1 cells are more reliant on their mitochondria for ATP production.

IAA treatment caused a large significant decrease in ATP levels in all galactose-grown cells, meaning glycolysis was still highly active (***P<0.0001) (Figure 4.13a). Including 10mM 2-deoxyglucose (DG) in the 1hr treatments confirmed that galactose-grown cells were producing the bulk of their ATP from the glycolytic breakdown of galactose (***P<0.0001) (Figure 4.13b).

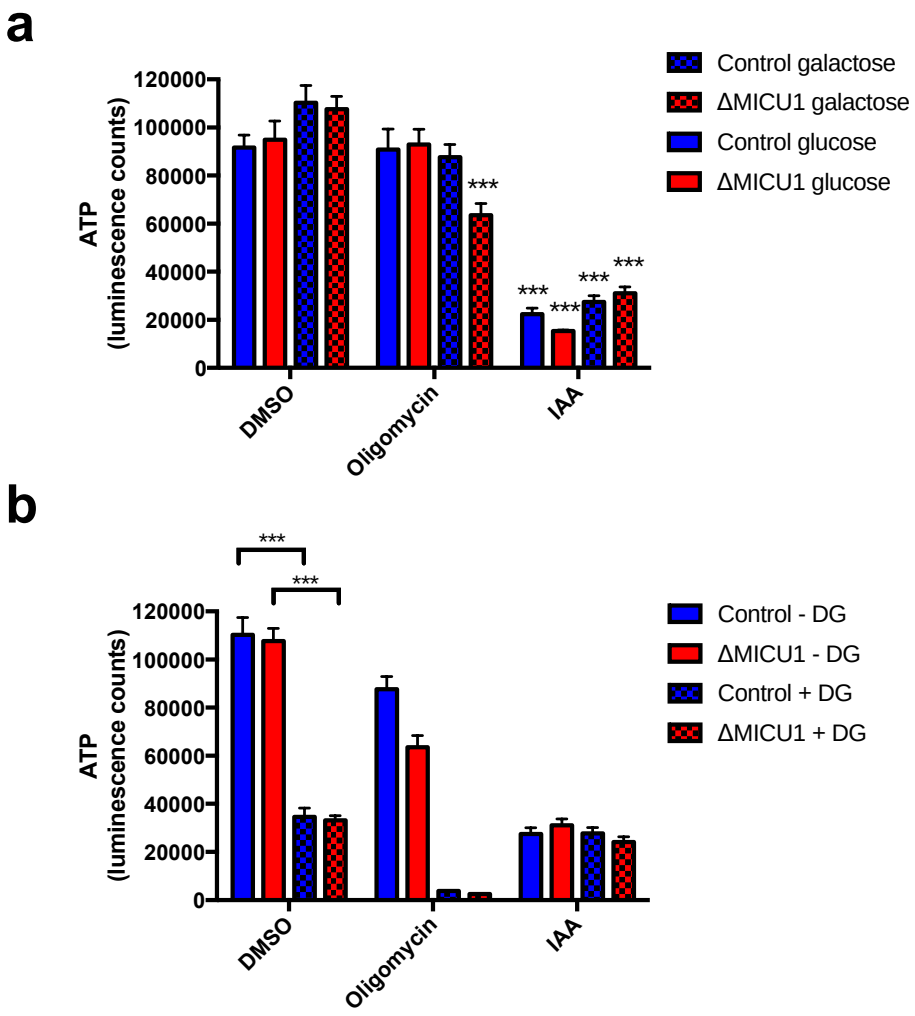

Figure 4.13: ΔMICU1 cells produce more mitochondrial ATP than controls when grown in galactose

Control and ΔMICU1 fibroblasts grown in glucose or galactose were pre-treated with DMSO, 5μM oligomycin and 1mM IAA before being processed via a commercial ATP assay kit (a). 10mM 2-deoxyglucose treatment was also included in the assays of galactose-grown cells (b). Luminescence readout is proportional to ATP content. Asterisks in (a) indicate statistical comparison with corresponding DMSO control. Statistical differences were tested using two-way ANOVA with post hoc Tukey correction. n=6 replicates pooled from both cell lines (2 control and 2 ΔMICU1 cell lines were measured on 3 experimental days).

4.3.8 The loss of MICU1 is associated with increased PDH activity

The loss of MICU1 causes the MCU to be constitutively active and the mitochondria become Ca^{2+} loaded even at resting $[Ca^{2+}]_c$. A rise in $[Ca^{2+}]_m$ increases the activity of three mitochondrial dehydrogenases, including PDH (see Introduction Figure 1.7), so the activity of these enzymes should be increased in the ΔMICU1 cells. To get an indication of its activity, the phosphorylation status of PDH was assessed using western blotting (Figure 4.14a). To account for possible differences in the amount of enzyme present in each cell line, the ratio of pPDH intensity to total PDH intensity was quantified. In keeping with elevated resting $[Ca^{2+}]_m$ and enhanced Ca^{2+}-activated PDP activity, the pPDH/PDH ratio was significantly reduced in ΔMICU1 cells (0.4828 ± 0.0972) compared to controls (1.00 ± 0.129) (P=0.0064) (Figure 4.14b). This is in agreement with our group's published data showing that MICU1 loss results in increased levels of NADH at rest (Logan et al. 2014).

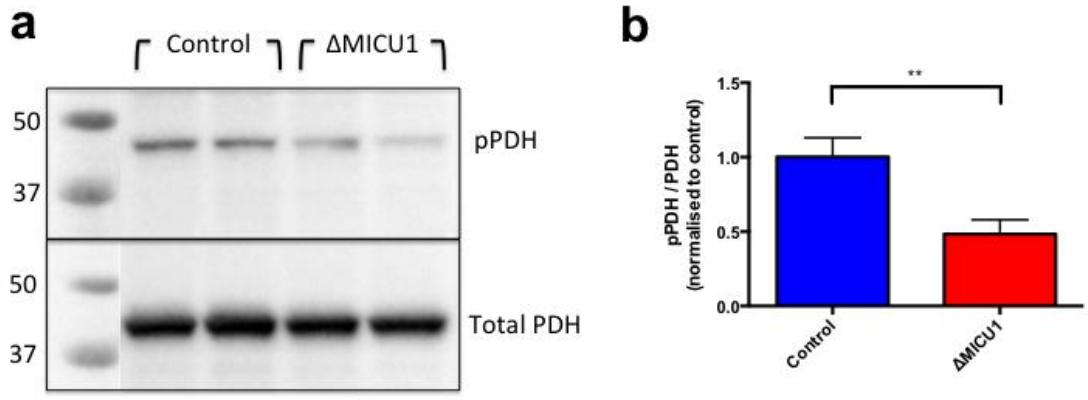

Figure 4.14: PDH is hypophosphorylated in ΔMICU1 cells

Whole cell lysates from galactose-cultured control and ΔMICU1 cells were immunoblotted for pPDH (PDH-E1α pS293) and total PDH (PDH-E1α) (a). The ratio of band intensities was normalised to the average control ratio on each experimental day (b). n=8 replicates pooled from both cell lines (2 control and 2 ΔMICU1 cell lines were measured on 4 experimental days).

4.3.9 Inhibition of mitochondrial Ca^{2+} export revealed futile Ca^{2+} cycling in the ΔMICU1 fibroblasts

An increase in $[Ca^{2+}]_m$ should ultimately activate Ca^{2+} efflux pathways in the mitochondria. Because the ΔMICU1 mitochondria are continually taking up Ca^{2+} at resting $[Ca^{2+}]_c$, it seems inevitable that they are also extruding Ca^{2+} through increased activation of the NCX and subsequent promotion of Na^+/H^+ exchange (see Introduction figure 1.7). This should offset the PMF and reduce ATP generation in the ΔMICU1 cells, though this is not obvious due to the increased PDH activation. To test this futile cycling theory, control and ΔMICU1 fibroblasts loaded with rhod-FF AM were imaged in the presence of NCX inhibitor CGP-37157 (Figure 4.15a & b). Rhod-FF was used because it is a lower affinity Ca^{2+} indicator (K_d=19μM), which should be able to pick up large changes in $[Ca^{2+}]_m$ that would otherwise saturate rhod-2 (K_d=570nM). In keeping with what was previously seen with rhod-2, average resting rhod-FF intensity was significantly higher in the ΔMICU1 cells (169 ± 9.30 A.U.) than in controls (122 ± 5.91 A.U.) ($P<0.0001$) (Figure 4.15c). Application of CGP-37157 caused an increase in mitochondrial Ca^{2+} content in the ΔMICU1 cells (1.56 ± 0.0637 fold) that was significantly larger than in controls (1.32 ± 0.021 fold) ($P=0.0006$) (Figure 4.15d). This increase was also significantly faster in the ΔMICU1 cells (0.0141 ± 0.00317 fold increase per min) than in control cells (0.00415 ± 0.000536 fold increase per min) ($P=0.0022$) (Figure 4.15e).

Accordingly, I measured cellular [ATP] in control and ΔMICU1 cells that had been treated with either DMSO or CGP-357157. This showed that NCX inhibition caused a significantly larger change in [ATP] in the ΔMICU1 cells (108 ± 1.89%) than in controls (95.6 ± 4.85%) ($P=0.04$) (Figure 4.15f). Although this increase in [ATP] was relatively small (approximately 8%), it is consistent with the energetically wasteful mitochondrial Ca^{2+} cycling in the ΔMICU1 cells.

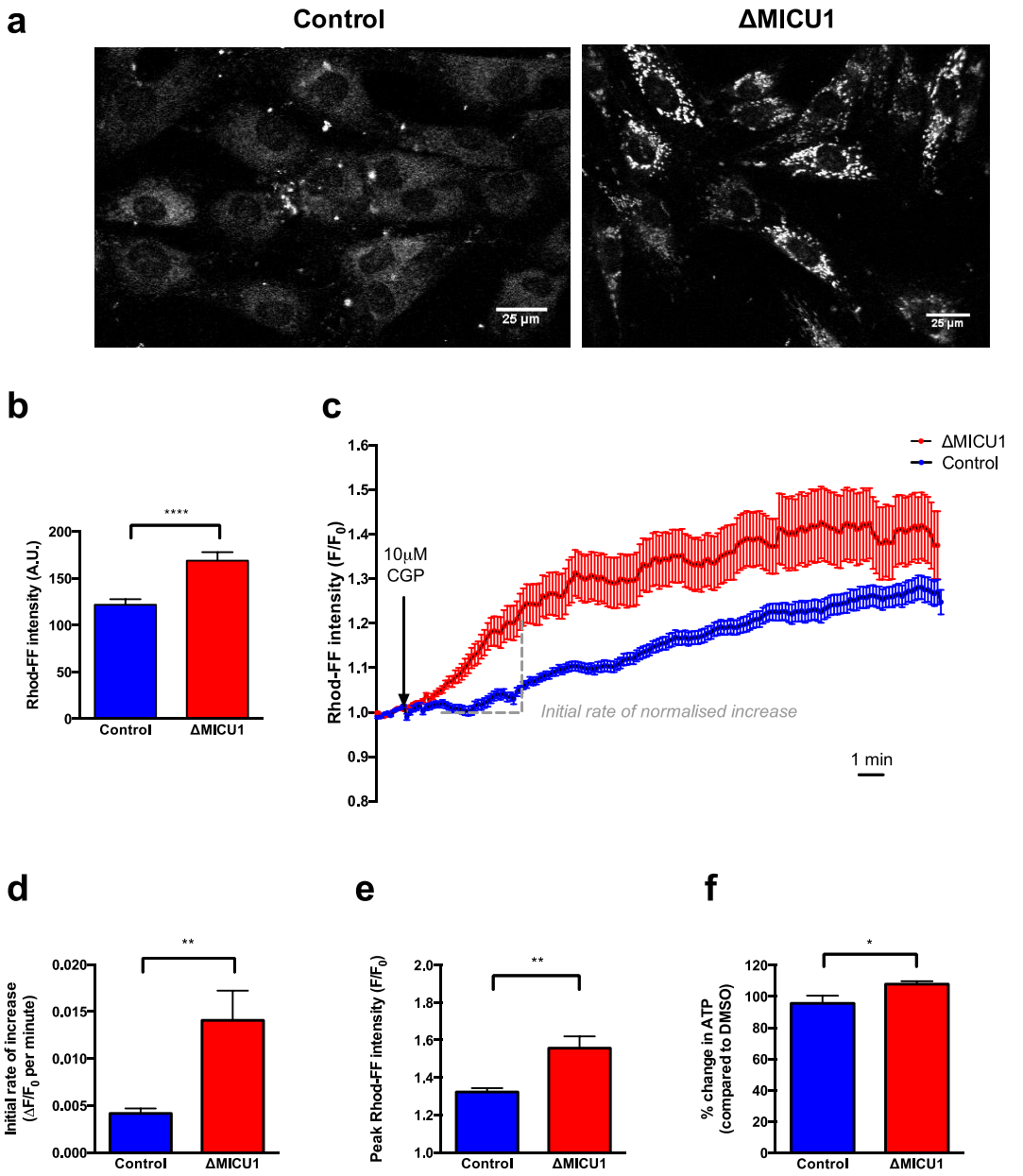

Figure 4.15: ΔMICU1 cells show increased mitochondrial Ca^{2+} uptake when NCX-mediated efflux is blocked

Representative confocal images of galactose-cultured, rhod-FF loaded fibroblasts after approximately 7 mins of 10µM CGP-37157 incubation (a). After normalising each time point to resting rhod-FF intensity (b), average traces were plotted (c). Resting rhod-FF intensity was calculated as the average fluorescence of each cell over the first 30 secs; mean cell average is shown in (b). The initial rate of normalised increase was analysed as shown in (c) and quantified in (d). The peak of normalised rhod-FF intensity was calculated as the maximum value over the entire time course (approx. 20mins) and was quantified in (e). n>100 cells from 3 independent experiments. Control and MICU1-deficient fibroblasts were pre-treated with DMSO and 10µM CGP-37157 before having total ATP content quantified (f).

Luminescence values were normalised to DMSO treatment i.e. 100% indicates no change in ATP. n=3 day averages from 3 independent experiments.

4.3.10 Mitochondrial networks were fragmented in ΔMICU1 cells

Imaging resting cells with TMRM (Figure 4.16a) and rhod-2 (Figure 4.6) revealed differences in mitochondrial morphology; while the control cells had intricate, elongated mitochondrial networks, the ΔMICU1 cells appeared to have more rounded, broken up mitochondria. Further quantification showed that a significant proportion of ΔMICU1 cells had this fragmented phenotype (Figure 4.16b, P=0.0003) (Figure 4.16c, P=0.0041). Quantification of the rhod-2 fluorescence in such cells confirmed that the fragmentation was associated with increased resting mitochondrial Ca^{2+} levels (P=0.0099) (Figure 4.16d).

Figure removed due to copyright restrictions

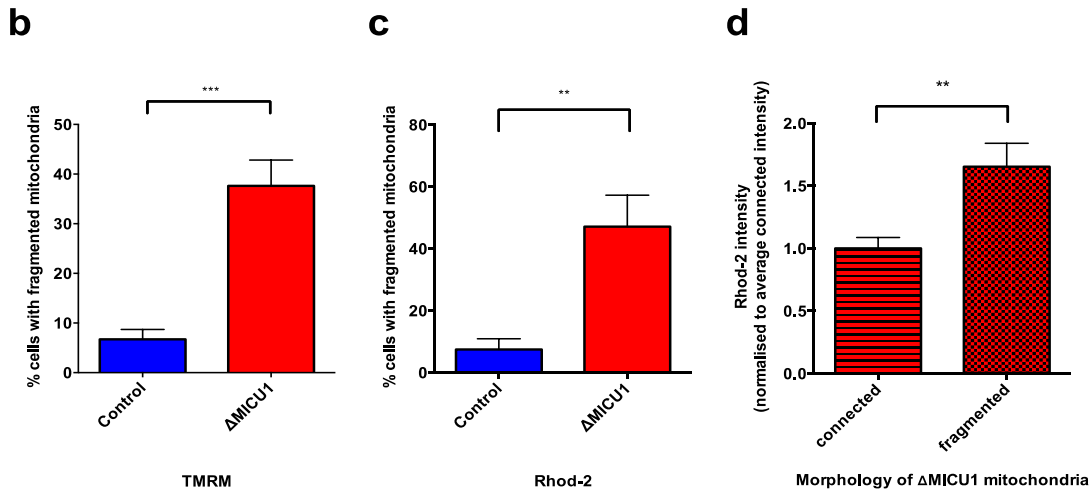

Figure 4.16: Loss of MICU1 affects mitochondrial morphology

Representative confocal image of glucose-cultured fibroblasts co-loaded with fluo-4 and TMRM (a). The number of cells with fragmented mitochondria was quantified from TMRM (b) and rhod-2 (c) images. After morphology scoring, the intensity of each cell was measured and normalised to the average intensity of all 'connected' cells on each experimental day (d). n=6 replicates pooled from both cell lines (2 control and 2 ΔMICU1 cell lines were measured on 3 experimental days). At least 10 cells were measured per cell line per day. Therefore values shown are mean of means for each replicate.

Although a significant proportion of ΔMICU1 cells displayed a fragmented, Ca^{2+} loaded mitochondrial phenotype, not all of the cell population were affected in this way (Figure 4.16b & c). This heterogeneity could reflect the Ca^{2+} signalling history of each cell; a rise in $[Ca^{2+}]_m$ far outlasts the initiating cytosolic Ca^{2+} signal (Boitier et al. 1999), so a cell that shows spontaneous $[Ca^{2+}]_c$ fluctuations might be more likely have a higher resting $[Ca^{2+}]_m$ than a less active cell. In support of this, the fibroblasts showed sporadic $[Ca^{2+}]_c$ transients that varied considerably within the population (Figure 4.17a). The frequency of these spontaneous transients was quantified, and was found to be no different between ΔMICU1 and control cells (P=0.456) (Figure 4.17b). Abolishing mitochondrial Ca^{2+} uptake with FCCP significantly increased the frequency of spontaneous transients in both control (P=0.0377) and ΔMICU1 cells (P=0.0497) (Figure 4.17b), which is consistent with the view that the mitochondria regulate local Ca^{2+} and the propagation of signals (Boitier et al. 1999). There was also no significant difference between the number of spontaneously active cells in control and ΔMICU1 cell populations (P=0.156) (Figure 4.17c).

a

Figure removed due to copyright restrictions

b

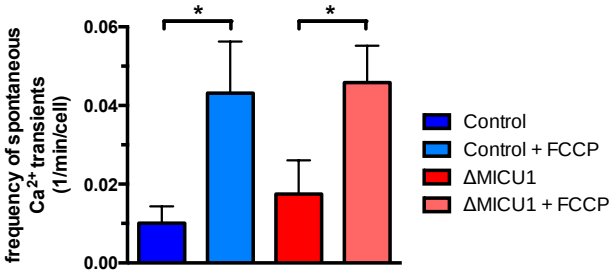

c

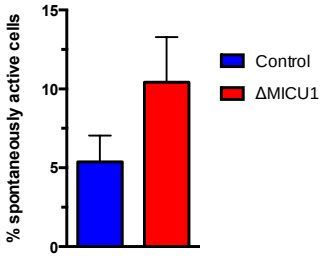

Figure 4.17: Control and ΔMICU1 fibroblasts showed spontaneous $[Ca^{2+}]_c$ activity

Spontaneous Ca^{2+} transients were measured in fluo-4 loaded cells using confocal microscopy. Representative traces from an imaging field of ΔMICU1 cells (a). Frequency of spontaneous Ca^{2+} transients (b) and the number of spontaneously active cells (c) was quantified. n=6 replicates pooled from both cell lines (2 control and 2 ΔMICU1 cell lines were measured on 3 experimental days). At least 5 cells were measured per cell line per day. Therefore values shown are mean of means for each replicate.

4.3.11 Mitochondrial fragmentation in the ΔMICU1 cells may be due to increased DRP1 activity

A significant number of ΔMICU1 fibroblasts had a fragmented mitochondrial network (Figure 4.16). To see whether this phenotype was the result of increased mitochondrial fission, the phosphorylation status of S637 (inhibitory phosphorylation site) of DRP1 was assessed using western blotting (Figure 4.18a). To account for possible differences in the amount of DRP1 protein in each cell line, the ratio of pDRP1 intensity to total DRP1 intensity was quantified. The pDRP1/DRP1 ratio was significantly reduced in the ΔMICU1 cells (0.394 ± 0.0620) when compared to controls (1.00 ± 0.0807) (P<0.0001) (Figure 4.18b), suggesting that DRP1 was more active and mitochondrial fission may have been dominant.

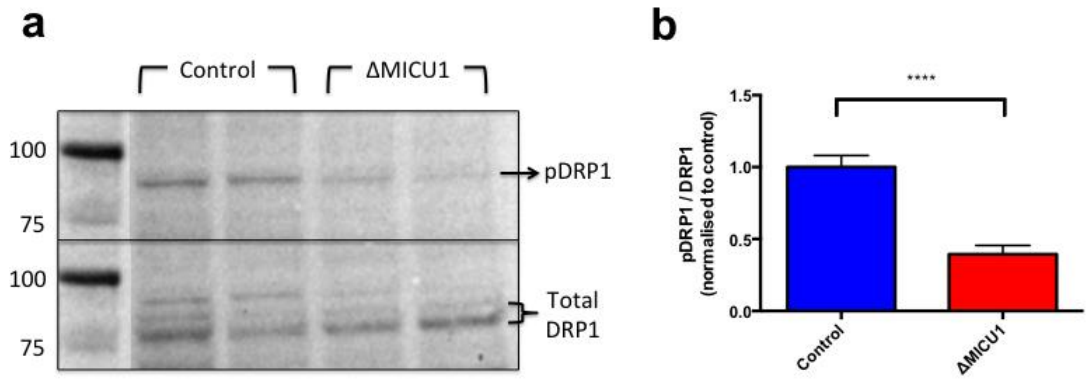

Figure 4.18: Reduced DRP1 S637 phosphorylation in ΔMICU1 cells

Whole cell lysates from galactose-cultured control and ΔMICU1 cells were immunoblotted for pDRP1 (S637) and total DRP1 (a). The ratio of band intensities was normalised to the average control ratio on each experimental day (b). n=8 replicates pooled from both cell lines (2 control and 2 ΔMICU1 cell lines were measured on 4 experimental days).

4.3.12 The loss of MICU1 does not alter autophagy flux

Since mitochondrial fission is a prerequisite for mitophagy, the ΔMICU1 cells maybe activating autophagy as a way to eliminate their fragmented, Ca^{2+} loaded mitochondria. On the other hand, the permanent presence of fragmented mitochondria might suggest that autophagy is being inhibited or is defective in some way. To assess autophagic flux under basal conditions, the amount of LC3-II was measured in DMSO and bafilomycin treated control and ΔMICU1 fibroblasts (Figure 4.19a). As expected, vacuolar H^+ ATPase and autophagy inhibitor bafilomycin significantly increased the level of LC3-II in both control ($P=0.001$) and ΔMICU1 cells ($P<0.0001$) (Figure 4.19b). However there was no significant difference ($P=0.827$) in basal LC3-II levels between control (0.172 ± 0.0186) and ΔMICU1 cells (0.262 ± 0.0142) (Figure 4.19b). There was also no significant difference ($P=0.0509$) in LC3-II levels after bafilomycin treatment between control (0.760 ± 0.0455) and ΔMICU1 cells (1.05 ± 0.0329) (Figure 4.19b).

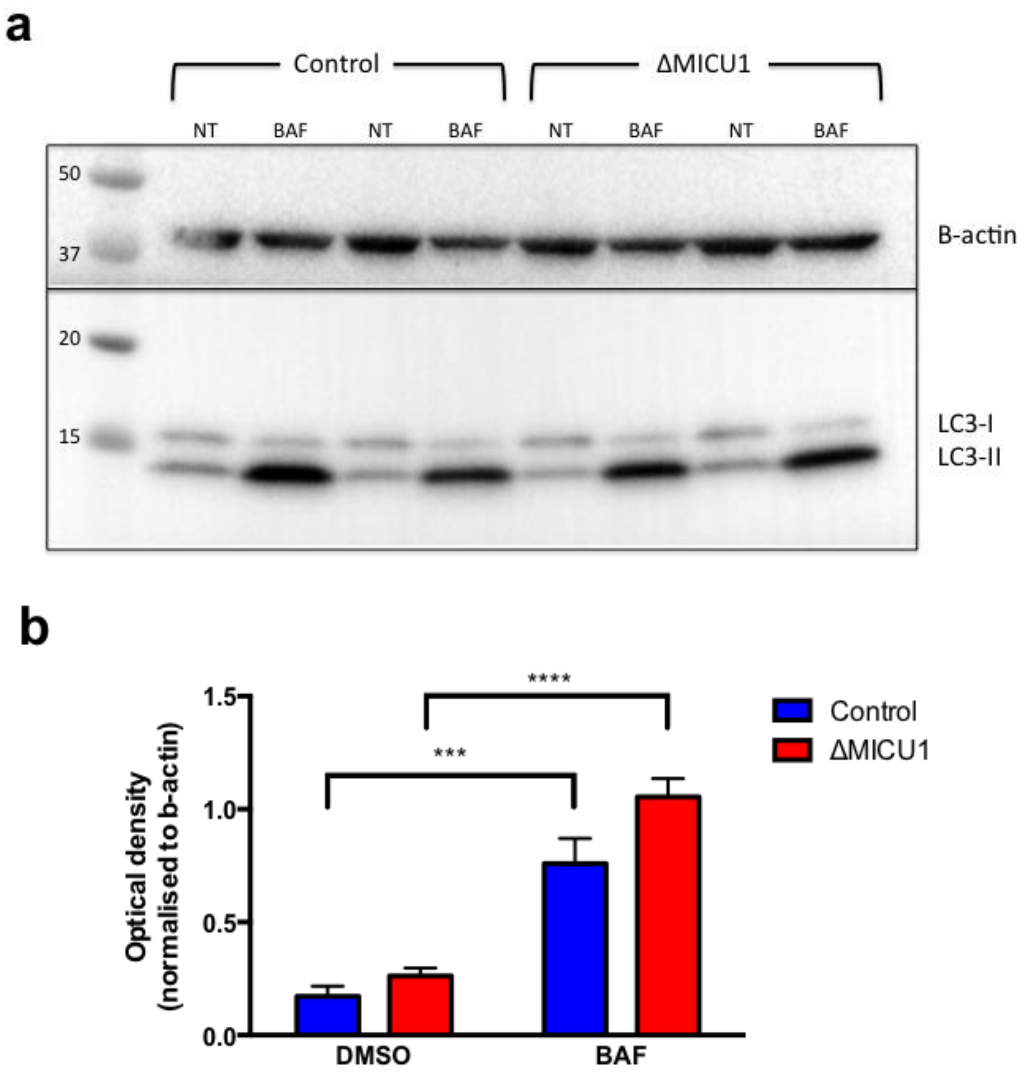

Figure 4.19: Autophagy is not altered in ΔMICU1 cells

Galactose-cultured control and ΔMICU1 cells were treated with 1uL/mL DMSO (NT) or 100nM bafilomycin A1 (BAF) for 5hrs before having total protein extracted and immunoblotted for LC3 (a). Intensity of the LC3-II band at 14kDa was normalised to b-actin loading control (b). Statistical differences were analysed using two-way ANOVA with Tukey post hoc correction. n=6 replicates pooled from both cell lines (2 control and 2 ΔMICU1 cell lines were measured on 3 experimental days).

4.4 Discussion

In this chapter, I have presented a range of data showing the status of cellular bioenergetics and Ca^{2+} homeostasis in fibroblasts derived from patients lacking the MICU1 protein. My results agree with the established theory that MICU1 acts as a gatekeeper of the MCU by setting an intracellular threshold concentration for mitochondrial Ca^{2+} uptake (Mallilankaraman, Doonan, et al. 2012; Csordás et al. 2013). However, there are discrepancies between my work and parts of the literature, which I will now review in conjunction with the aims set out at the start of this thesis (see Introduction 1.6).

4.4.1 Ca^{2+} homeostasis in ΔMICU1 fibroblasts

It is evident that authors of the first MICU1 KD study were mistaken in their conclusion that MICU1 is essential for mitochondrial Ca^{2+} uptake. In agreement with the work of many others, my aequorin data proves that the mitochondria of ΔMICU1 cells are capable of taking up Ca^{2+}. It is not clear why Perocchi et al. observed the opposite result but it may be due to technical and analytical differences. Like Mallilankaraman et al. but in contrast to Csordas et al., I found that a lack of MICU1 does not affect the peak mitochondrial Ca^{2+} concentration reached during ER Ca^{2+} release, but does increase mitochondrial Ca^{2+} load at resting cytosolic concentrations and after spontaneous, low frequency, cytoplasmic Ca^{2+} transients. In addition, I found evidence of accelerated mitochondrial Ca^{2+} uptake, which has not been reported in previous KD studies. These results demonstrate the function of MICU1 in restricting mitochondrial Ca^{2+} uptake to a sigmoidal dependence on $[Ca^{2+}]_c$ (Figure 4.20). Without MICU1 there is no threshold for uptake and sigmoidicity is lost, meaning mitochondria are Ca^{2+}-loaded at rest and uptake occurs in a more linear fashion (Figure 4.20). Although the sigmoidal dependence of mitochondrial Ca^{2+} uptake on $[Ca^{2+}]_c$ has been known about for a long time, its physiological importance is only truly appreciated now that this ΔMICU1 patient cohort has been discovered.

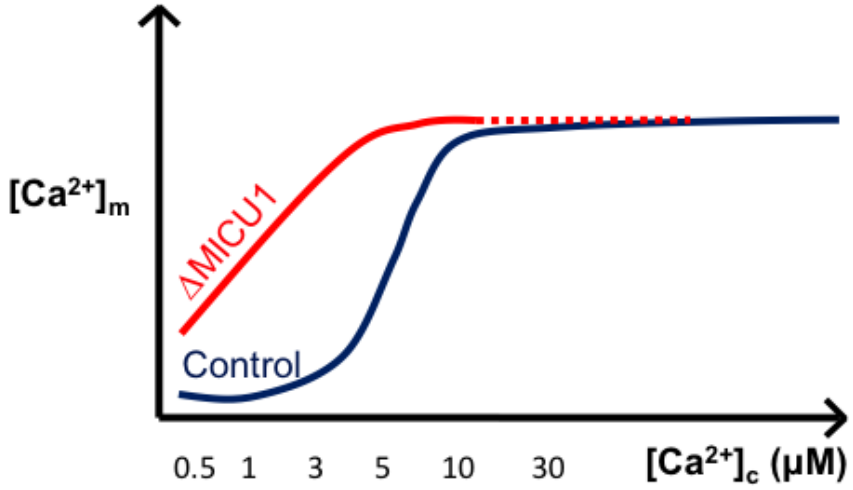

Figure 4.20: Schematic illustration of the sigmoidal dependence of mitochondrial Ca^{2+} uptake on cytosolic Ca^{2+} concentration

The loss of MICU1 alleviates the threshold for uptake, meaning mitochondria are Ca^{2+} loaded at rest and uptake occurs in a more linear fashion. Figure based on data from (Csordás et al. 2013).

Cell population measurements revealed that cytoplasmic Ca^{2+} signals were reduced in ΔMICU1 fibroblasts due to enhanced mitochondrial Ca^{2+} buffering. Given the importance of Ca^{2+} signalling for muscle contraction and synaptic transmission, this enhanced mitochondrial buffering capacity might explain why the muscle and brain are primarily affected in these patients. While it might be surprising that the patients do not have a cardiomyopathy, the heart has a much lower MICU1:MCU expression ratio (De Stefani et al. 2011), which suggests that the threshold concentration for mitochondrial Ca^{2+} uptake is much lower in the heart. In theory, this makes physiological sense, as it is crucial that heart mitochondria make enough ATP to support beat-by-beat contractions.

4.4.2 Bioenergetic consequences of MICU1 loss

Despite having a chronically active MCU, the ΔMICU1 fibroblasts showed no differences in steady state $\Delta\Psi_m$, O_2 consumption or ATP levels; this was surprising, as I expected an increase in mitochondrial matrix Ca^{2+} concentration to activate the citric acid cycle and increase ATP production. On the other hand, my results are in agreement with previous MICU1 KD

studies, where no changes in $\Delta\Psi_m$, resting O_2 consumption or ATP levels have ever been reported. The only discrepancy concerns Ca^{2+}-enhanced respiration; in contrast with Mallilankaraman et al., I found no difference in O_2 consumption between control and ΔMICU1 cells after stimulation with 10μM histamine. However, this result is in keeping with our group's observation that MICU1 loss does not affect NADH levels after 10μM histamine addition (Logan et al. 2014). Furthermore, these results are in agreement with my aequorin data, which showed that a lack of MICU1 does not affect peak $[Ca^{2+}]_m$ after stimulation with 10μM histamine. Mallilankaraman et al. did not measure peak $[Ca^{2+}]_m$ during 10μM histamine stimulation but perhaps it was elevated in their MICU1 KD model, thus explaining why an increase in Ca^{2+}-enhanced respiration was observed.

Measuring ATP levels after treatment with OXPHOS or glycolysis inhibitors revealed that both control and ΔMICU1 fibroblasts were heavily relying on glycolysis for ATP production. As MICU1 is a mitochondrial protein that indirectly regulates mitochondrial metabolism, I concluded that a glycolytic fibroblast model was not particularly useful for investigating the bioenergetic consequences of MICU1; I decided to switch to galactose culture conditions to see if this would reveal a bioenergetic defect in the ΔMICU1 cells. Although basal ATP levels were similar in galactose-grown ΔMICU1 cells and controls, oligomycin treatment showed that the mitochondria of the ΔMICU1 cells were making a bigger contribution to ATP production; this may be attributed to the fact that PDH was hypophosphorylated and therefore more active in these cells. However, this increase in oxidative phosphorylation in the ΔMICU1 cells did not correspond with a significant increase in O_2 consumption. I can only assume that this is because the sensitivity and resolution of the Oroboros respirometer is below that required for these fibroblasts with relatively low overall O_2 flow.

According to the literature, growing cells in galactose causes a metabolic switch from glycolysis to oxidative glutamine metabolism. This is true for the primary human fibroblasts I have tested; when the cells were grown in galactose, there was a trend for an increase in respiratory rates and a

significant increase in mitochondrial ATP production. However, treatment with glycolysis inhibitor 2DG showed that the fibroblasts were still producing the bulk of their ATP through glycolysis i.e. by breaking down the galactose into glucose-6-phosphate. This highlights the need for caution when using galactose as a growth substrate; although it is widely accepted that galactose increases cellular oxidative capacity, how well it can achieve this may vary between cell types. Even though mitochondrial ATP synthesis was higher in the ΔMICU1 cells, 2DG still caused a significantly large drop in [ATP]; this suggests that the ΔMICU1 cells still rely on the glycolytic production of pyruvate, which is used as an anaplerotic substrate for the citric acid cycle, in addition to glutamine use. Indeed, PDH is hypophosphorylated in the ΔMICU1 cells, which could lead to higher flux of pyruvate into the citric acid cycle.

An increase in $[Ca^{2+}]_m$ inevitably leads to the activation of efflux pathways. When mitochondrial Ca^{2+} export was blocked in the ΔMICU1 cells, $[Ca^{2+}]_m$ increased at a much higher rate than in controls. This suggests that under resting conditions a futile mitochondrial Ca^{2+} cycle is maintained in the ΔMICU1 cells, which ultimately undermines their bioenergetic capacity and might explain why overall [ATP] is not increased; the increased activity of PDH is essentially offset by the increased activity of the NCX in conjunction with the Na^+/H^+ exchanger (Figure 4.21). In agreement with this, [ATP] was higher in ΔMICU1 cells than controls after pre-treatment with the NCX inhibitor, CGP-37157. However, a proton influx independent of the ATP synthase should effectively uncouple the mitochondrial membrane and either decrease $\Delta\Psi_m$ or increase O_2 consumption (to maintain $\Delta\Psi_m$) (Figure 4.21). Uncoupling should also cause an increase in the amount of leak respiration i.e. O_2 consumption in the presence of oligomycin. Since I have not observed any of these particular changes, my data are not fully consistent with this futile cycle model. I suspect that O_2 consumption is in fact increased in the absence of MICU1 but this change is below the resolution of the Oroboros respirometer. I also observed a lot of day-to-day variability in these measurements, which might suggest that further optimisation is required, or perhaps that a different respirometry method should be used.

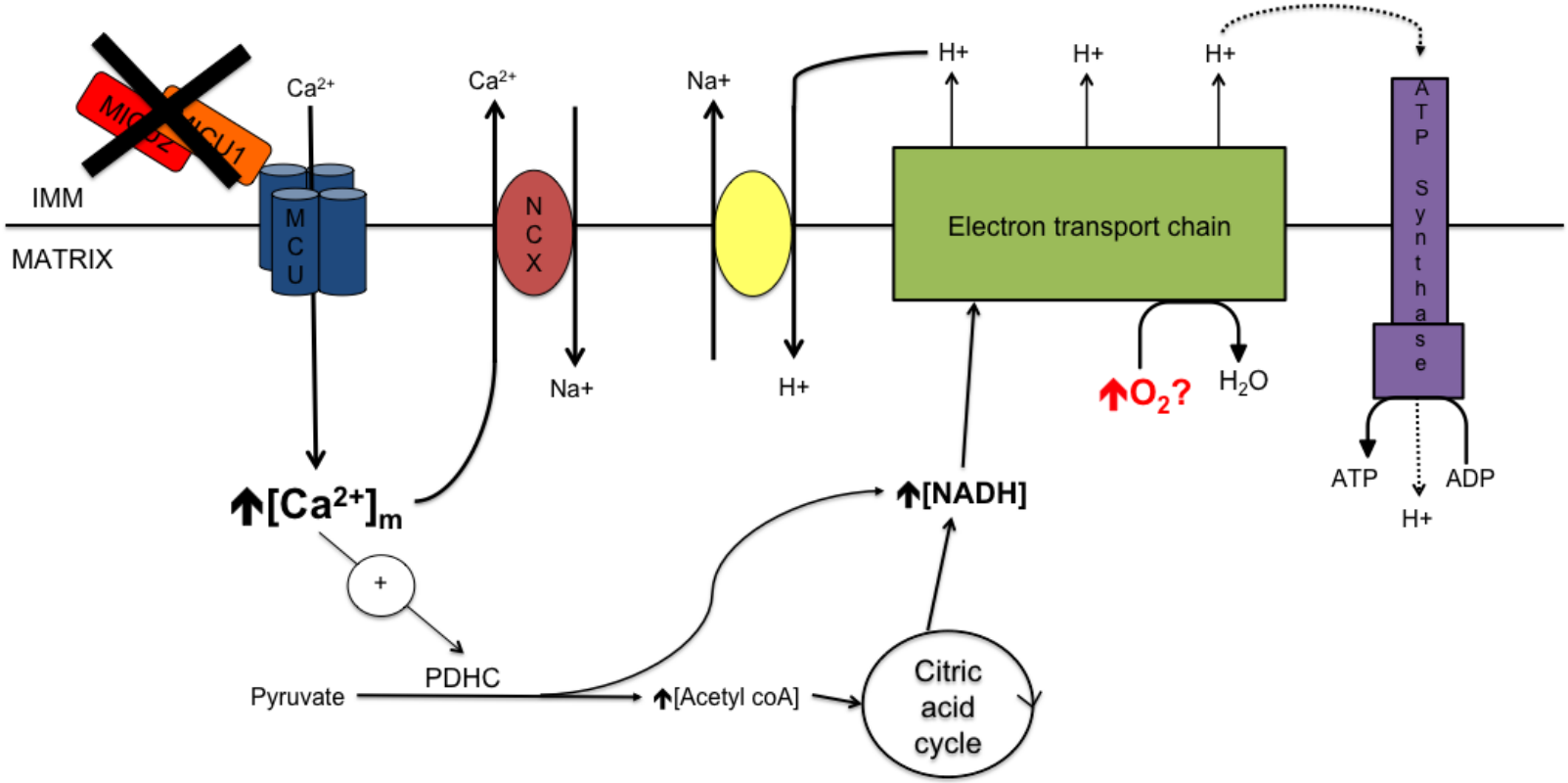

Figure 4.21: Schematic illustrating the bioenergetic cost of mitochondrial Ca^{2+} accumulation in the MICU1-deficient cells

The loss of MICU1 means the MCU is constitutively active and resting $[Ca^{2+}]_m$ is increased. This activates the mitochondrial Na^+/Ca^{2+} exchanger (NCX) and causes a futile Ca^{2+} cycle. Increased $[Ca^{2+}]_m$ also activates the pyruvate dehydrogenase complex (PDHC) and increases NADH production. This increased NADH supply should increase respiratory chain activity and thus O_2 consumption, but this has not been observed in the ΔMICU1 fibroblast model.

4.4.3 Mitochondrial morphology is altered in ΔMICU1 fibroblasts

Although the ΔMICU1 fibroblasts do not seem to be energetically compromised, there is certainly evidence of mitochondrial stress through the fragmented phenotype shown by approximately 40-50% of the cell population. This mitochondrial fragmentation was associated with increased resting $[Ca^{2+}]_m$ and could be somewhat reversed by the viral expression of WT MICU1 protein (Logan et al. 2014). Although MICU1 deficiency has never before been linked to altered mitochondrial morphology, pharmacologically induced mitochondrial Ca^{2+} overload has been shown to cause mitochondrial fission in prostate cancer cells (Kaddour-Djebbar et al. 2010). However, it is not clear why or how increased $[Ca^{2+}]_m$ is associated with mitochondrial fragmentation in the ΔMICU1 fibroblasts, particularly as they do not seem to suffer from energetic dysfunction or increased oxidative stress. Mitochondrial fragmentation is usually an early apoptotic event but increased fission does not necessarily result in cell death (Youle & Karbowski 2005) and I have not observed reduced viability while culturing these cells. It is worth keeping in mind that not all of the ΔMICU1 fibroblasts display fragmented, Ca^{2+} loaded mitochondria at rest, and even within the same cell the mitochondria can vary in appearance and $[Ca^{2+}]_m$. This heterogeneity may reflect the different Ca^{2+} signalling histories of each cell and each mitochondrion; for example, a cell that has undergone frequent spontaneous activity may be more likely to have Ca^{2+} loaded mitochondria at rest. Moreover, if these mitochondria were positioned close to Ca^{2+} release sites at the time of a signal, they may be even more likely to have higher resting $[Ca^{2+}]_m$.

To gain a better understanding of the molecular mechanism behind the increased fragmentation in the ΔMICU1 fibroblasts, I investigated DRP1 activation by quantifying the amount of phosphorylation of its inhibitory S637 site. I found that this S637 site was hypophosphorylated in the MICU1-deficient cells, indicating that increased DRP1 activity was behind the fragmented phenotype. Dephosphorylation of the S637 site is carried out by the cytosolic phosphatase, calcineurin, which is activated during a sustained

rise in intracellular Ca^{2+} levels (Cereghetti et al. 2008). Such a pathological Ca^{2+} rise could occur following mitochondrial depolarisation but my measurements of Ca^{2+} transients after FCCP treatment showed this not to be the case in the ΔMICU1 cells (Figure 4.5c). Although it is not clear exactly how DRP1-dependent fission is activated in the ΔMICU1 cells, it could be an important cellular adaptation. It has been previously shown that DRP1-dependent fission protects against Ca^{2+}-mediated apoptosis by blocking intra-mitochondrial Ca^{2+} waves (Szabadkai et al. 2004). This means that fragmented mitochondria are less exposed to substantial $[Ca^{2+}]_m$ elevations, which seems crucial for ΔMICU1 mitochondria that already have elevated basal $[Ca^{2+}]_m$. As a collective population the ΔMICU1 cells do not show reduced agonist-induced mitochondrial Ca^{2+} uptake, but perhaps on a single cell level the $[Ca^{2+}]_m$ responses vary according to mitochondrial morphology.

Since mitophagy is associated with mitochondrial fission, I tested to see whether basal levels of autophagy were altered in the ΔMICU1 cells. This did not appear to be the case, as the relative amount of the autophagic marker LC3-II after 5 hrs of DMSO or bafilomycin treatment was similar between control and ΔMICU1 cells. This is in agreement with the results of a previous study of MICU1 KD in HeLa cells (Mallilankaraman, Doonan, et al. 2012). While increased $[Ca^{2+}]_m$ appears to have no effect on autophagy, a reduction in $[Ca^{2+}]_m$ is thought to increase autophagy through AMPK activation (Rizzuto et al. 2012; Cárdenas & Foskett 2012). This theory, however, has been recently challenged by the creation of an MCU KO mouse, which showed no alteration in basal metabolism (Pan et al. 2013).

4.4.4 Future work

Previous work has shown that MICU1 KD enhances sensitivity to cell death (Mallilankaraman, Doonan, et al. 2012; Csordás et al. 2013). Time limitations meant that I could not test this in the ΔMICU1 cells but I would expect that their elevated resting $[Ca^{2+}]_m$ would make them vulnerable to cell death through 'priming' of the mPTP. As it is difficult to experimentally observe mPTP opening in whole cells (personal observations within our group), this

theory should be tested by carrying out Ca^{2+} retention capacity (CRC) assays on isolated ΔMICU1 mitochondria (ideally from a muscle sample). This involves sequentially adding Ca^{2+} to a mixture of mitochondria and membrane impermeable fluorescent Ca^{2+} indicator; the mitochondria will take up and buffer this Ca^{2+} (resulting in a decrease in fluorescence signal) until the threshold for mPTP opening is reached and $\Delta\Psi_m$ is lost (causing an increase in fluorescence signal).

The molecular makeup of the mitochondrial calcium uniporter complex is still yet to be fully understood but many different proteins appear to be involved. I have focussed on the physiological role of MICU1 in this project but it would be interesting to investigate its relationship with other proteins residing in the mitochondrial calcium uniporter complex. The relationship between MCU, MICU1 and MICU2 is perhaps of most interest, given the present disagreements in the literature. Mootha et al. have suggested that MICU1 and MICU2 are both gatekeepers of the MCU and are functionally non-redundant (Kamer & Mootha 2014). However, Patron et al. have presented evidence that MICU2 is the gatekeeper and MICU1 is an activator of the MCU; in their paper they show that MICU2 relies on MICU1 for stability, which means that a loss of MICU1 also results in a loss of MICU2 and therefore a lack of MCU regulation (Patron et al. 2014). When the data in this chapter was evaluated for publication, a peer reviewer asked whether MICU2 expression was altered in the ΔMICU1 fibroblasts. Interestingly, MICU2 protein was missing in the ΔMICU1 fibroblasts, but returned to normal levels when MICU1 was re-expressed (Figure 4.22). This supports the theory that MICU2 relies on MICU1 for stability, but does not alter the conclusion that the observed phenotype is the primary consequence of MICU1 deficiency.

Although the ΔMICU1 fibroblasts have shed some light on the general mechanism of mitochondrial Ca^{2+} handling, they have been unable to tell us much about the pathological process that has occurred (and might still be occurring) in the patients. A ΔMICU1 skeletal muscle model will need to be established in order to fully understand how and why minicores develop. The best option might be to make iPSCs from the patient fibroblasts, as these can

then be differentiated into neurons as well as skeletal muscle. It would then be interesting to know the effect of MICU1 deficiency on EC coupling, and whether there are any parallels to disease mechanisms proposed by other core myopathy models.

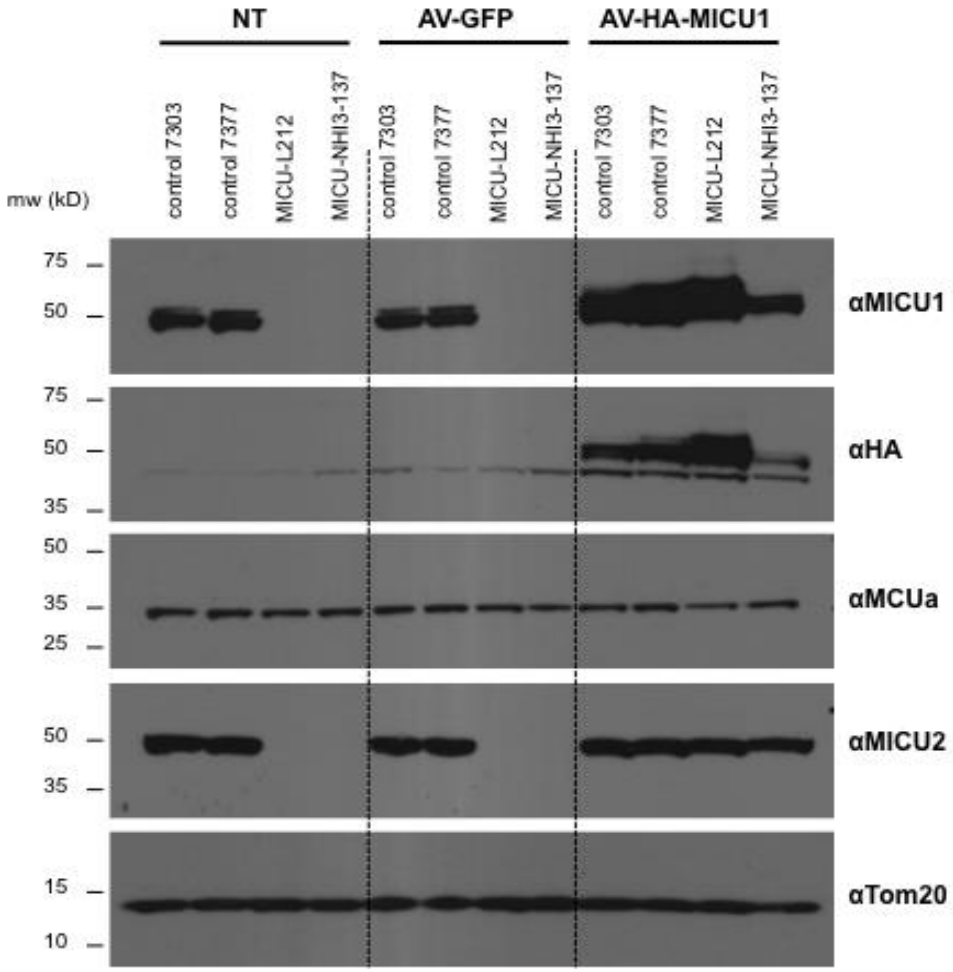

Figure 4.22: MICU1, MICU2 and MCU expression levels in ΔMICU1 fibroblasts

Left four lanes show non-transfected cells, the middle and right four lanes show cells transduced with GFP and HA-tagged MICU1 expressing adenoviral constructs, respectively. Anti-HA antibody shows the presence of exogenous MICU1. Expression of mitochondrial protein Tom20 was measured as a loading control. Figure kindly provided by the Rizzuto lab, Padova.

Chapter 5 Final conclusions

5.1 Summary of findings

The aim of this thesis has been to explore the possibility that mitochondria are contributing to core myopathy pathology by suffering from Ca^{2+}-related dysfunction. To test this theory, I assessed intracellular Ca^{2+} homeostasis and its possible effect on mitochondrial function in three core myopathy models with mutations in different proteins involved in muscle Ca^{2+} homeostasis.

The first model, which was discussed in Chapter 2, was a knockin mouse with a heterozygous RYR1 mutation that is associated with CCD in humans. Myotubes and myofibres originating from this mouse were used as cell models, reflecting immature and mature skeletal muscle cells, respectively. Unfortunately, both of these cell models failed to demonstrate the reduced cytosolic Ca^{2+} signals that this 'EC uncoupled' mutation is supposed to cause (Avila et al. 2001; Boncompagni et al. 2010; Loy et al. 2011). Despite the genetic alteration in RYR1, there appeared to be no functional alteration in the behaviour of the RyR1 channel and consequently, no significant mitochondrial dysfunction was observed. These results were attributed to the fact that this particular mouse sub-line was maintained on a mixed genetic background that had never been explored before. I concluded that successive breeding to a C57BL/6J background had drastically diluted the disease phenotype, as well as the functional RyR1 phenotype observed in the founder 129S2/SvPasCrl sub-line (Zvaritch et al. 2009). Although these findings significantly limit the value of this mouse sub-line for studying core myopathy pathology, it is interesting that genetic background has such a strong influence on the mouse phenotype; this may explain the variable disease severity also seen in humans.

In chapter 3 I described the first case of a core myopathy caused by a mutation in STAC3. Fibroblasts originating from this individual were characterised in terms of Ca^{2+} signalling and mitochondrial function, with the

purpose of providing preliminary data before a patient-specific muscle model is established. Histamine-induced Ca^{2+} release was significantly higher in the patient fibroblasts than in controls, which confirms that STAC3 has a role in general Ca^{2+} homeostasis but is difficult to interpret further, as fibroblasts do not express the EC coupling machinery that STAC3 is associated with. Although the mitochondrial population in the patient cells was slightly depolarised, O_2 consumption was not affected; this discrepancy should be investigated further in future skeletal muscle models.

In Chapter 4 I studied fibroblasts derived from individuals with loss-of-function mutations in MICU1. These cells displayed a striking mitochondrial phenotype; their mitochondria were largely fragmented and Ca^{2+}-loaded, even at basal unstimulated cytosolic Ca^{2+} concentrations. The sigmoidal dependence of mitochondrial Ca^{2+} uptake on $[Ca^{2+}]_c$ was also lost in these cells, which is consistent with the previously characterised gatekeeping function of MICU1. Despite chronic activation of the MCU and increased activation of Ca^{2+}-sensitive PDH, the ΔMICU1 fibroblasts showed no change in $\Delta\Psi_m$, basal O_2 consumption or ATP levels. The cells appear to have developed compensatory mechanisms to deal with such mitochondrial stress, which is perhaps reflected in the slow progression of clinical features in affected individuals (Logan et al. 2014; Bhosale et al. 2015). Interrupting mitochondrial Ca^{2+} efflux in these cells revealed some evidence of a futile Ca^{2+} cycle, where ongoing mitochondrial Ca^{2+} uptake at rest activates Na^+-H^+ exchange and effectively wastes PMF on balancing $[Ca^{2+}]_m$ rather than producing ATP. This shows that mitochondrial Ca^{2+} accumulation carries an energetic cost; although this may not be so obvious in this glycolytic fibroblast model, it is clearly evident in the cell types primarily affected by the mutation i.e. muscle and neurons. The physiological role of MICU1 appears to be as a signal-to-noise discriminator, filtering out cell noise and restricting uptake to only robust Ca^{2+} signals, thus allowing energy demand to be coupled to oxidative metabolism (Bhosale et al. 2015).

5.2 Does mitochondrial dysfunction contribute to core myopathy pathology?

I found no indication of mitochondrial dysfunction in the RYR1 I4895T mouse sub-line but given that there was also no evidence of RyR1 uncoupling or core formation, I think it is difficult to consider this particular sub-line as a core myopathy model. Although the same could be said about the skin fibroblasts I have studied, the fact that they are derived from core myopathy patients themselves gives them some value in answering the proposed question. The data collected on STAC3 W284S fibroblasts offers preliminary evidence of mitochondrial dysfunction inflicted by Ca^{2+} deregulation, though a lot more work is required to fully understand the patient disease pathology. The characterisation of fibroblasts from MICU1-deficient patients clearly demonstrates mitochondrial involvement in core pathology; the patients' disease is primarily caused by the loss of a protein that regulates mitochondrial Ca^{2+} uptake, resulting in obvious mitochondrial stress through fragmentation and basal Ca^{2+} loading. Although there was evidence of an energetically wasteful mitochondrial Ca^{2+} cycle in these ΔMICU1 cells, the overall degree of bioenergetic dysfunction was relatively mild, which was probably due to the glycolytic nature of this fibroblast model. A ΔMICU1 skeletal muscle model will now need to be developed to fully understand the patient disease pathology.

In this thesis I have shown that defective mitochondrial Ca^{2+} handling has a role in core myopathy pathology, though many questions remain about how exactly this leads to muscle weakness and core formation; the genetic and phenotypic variability across the core myopathy spectrum makes it seem likely that several pathological mechanisms exist. Nevertheless, mitochondria are clearly an integral part of skeletal muscle Ca^{2+} homeostasis and should not be overlooked in future core myopathy research.

References

Abrahams, J.P. et al., 1994. Structure at 2.8 A resolution of F1-ATPase from bovine heart mitochondria. *Nature*, 370(6491), pp.621–8.

Abramov, A.Y. & Duchen, M.R., 2003. Actions of ionomycin, 4-BrA23187 and a novel electrogenic Ca2+ ionophore on mitochondria in intact cells. *Cell calcium*, 33(2), pp.101–12.

Adhihetty, P.J. et al., 2003. Plasticity of skeletal muscle mitochondria in response to contractile activity. *Experimental physiology*, 88(1), pp.99–107.

Aguer, C. et al., 2011. Galactose enhances oxidative metabolism and reveals mitochondrial dysfunction in human primary muscle cells. *PloS one*, 6(12), p.e28536.

Ainscow, E.K. & Rutter, G.A., 2001. Mitochondrial priming modifies Ca2+ oscillations and insulin secretion in pancreatic islets. *The Biochemical journal*, 353(Pt 2), pp.175–80.

Alberts, B. et al., 2002. *Molecular Biology of the Cell* 4th ed., Garland Science.

Avila, G., O'Brien, J.J. & Dirksen, R.T., 2001. Excitation-contraction uncoupling by a human central core disease mutation in the ryanodine receptor. *Proceedings of the National Academy of Sciences*, 98(7), pp.4215–4220.

Bailey, A.G. & Bloch, E.C., 1987. Malignant hyperthermia in a three-month-old American Indian infant. *Anesthesia and analgesia*, 66(10), pp.1043–5.

Balaban, R.S., 2009. The role of Ca(2+) signaling in the coordination of mitochondrial ATP production with cardiac work. *Biochimica et*

biophysica acta, 1787(11), pp.1334–41.

Barbieri, E. & Sestili, P., 2012. Reactive oxygen species in skeletal muscle signaling. *Journal of signal transduction*, 2012, p.982794.

Barrientos, G.C. et al., 2012. Gene dose influences cellular and calcium channel dysregulation in heterozygous and homozygous T4826I-RYR1 malignant hyperthermia-susceptible muscle. *The Journal of biological chemistry*, 287(4), pp.2863–76.

Baughman, J.M. et al., 2011. Integrative genomics identifies MCU as an essential component of the mitochondrial calcium uniporter. *Nature*, 476(7360), pp.341–345.

Beck, M., 2012. Rare and Ultra Rare Diseases□. *Journal of Developing Drugs*, 01(06).

Berchtold, M.W., Brinkmeier, H. & Müntener, M., 2000. Calcium ion in skeletal muscle: its crucial role for muscle function, plasticity, and disease. *Physiological reviews*, 80(3), pp.1215–65.

Berg, J.M., Tymoczko, J.L. & Stryer, L., 2002. *Biochemistry* 5th ed., W H Freeman.

Bhosale, G. et al., 2015. Calcium signaling as a mediator of cell energy demand and a trigger to cell death. *Annals of the New York Academy of Sciences*, 1350(1), pp.107–116.

van der Bliek, A.M., Shen, Q. & Kawajiri, S., 2013. Mechanisms of mitochondrial fission and fusion. *Cold Spring Harbor perspectives in biology*, 5(6), p.a011072–.

Bloom, W. & Forcett, D.W., 1968. *A TEXTBOOK OF HISTOLOGY* 9th ed., Saunders.

Boitier, E., Rea, R. & Duchen, M.R., 1999. Mitochondria exert a negative feedback on the propagation of intracellular Ca2+ waves in rat cortical astrocytes. *The Journal of cell biology*, 145(4), pp.795–808.

Boncompagni, S. et al., 2009. Characterization and temporal development of cores in a mouse model of malignant hyperthermia. *Proceedings of the National Academy of Sciences of the United States of America*, 106(51), pp.21996–2001.

Boncompagni, S. et al., 2010. The I4895T mutation in the type 1 ryanodine receptor induces fiber-type specific alterations in skeletal muscle that mimic premature aging. *Aging cell*, 9(6), pp.958–70.

Bower, N.I. et al., 2012. Stac3 is required for myotube formation and myogenic differentiation in vertebrate skeletal muscle. *The Journal of biological chemistry*, 287(52), pp.43936–49.

Bower, N.I. & Johnston, I.A., 2010. Discovery and characterization of nutritionally regulated genes associated with muscle growth in Atlantic salmon. *Physiological genomics*, 42A(2), pp.114–30.

Boyer, P.D., 1993. The binding change mechanism for ATP synthase--some probabilities and possibilities. *Biochimica et biophysica acta*, 1140(3), pp.215–50.

Brand, M.D., 2010. The sites and topology of mitochondrial superoxide production. *Experimental gerontology*, 45(7-8), pp.466–72.

Brand, M.D., Chen, C.H. & Lehninger, A.L., 1976. Stoichiometry of H+ ejection during respiration-dependent accumulation of Ca2+ by rat liver mitochondria. *J Biol Chem*, 251(4), pp.968–974.

Brini, M. et al., 1995. Transfected aequorin in the measurement of cytosolic Ca2+ concentration ([Ca2+]c). A critical evaluation. *The Journal of biological chemistry*, 270(17), pp.9896–903.

Brislin, R.P. & Theroux, M.C., 2013. Core myopathies and malignant hyperthermia susceptibility: a review. *Paediatric anaesthesia*, 23(9), pp.834–41.

Brookes, P.S. et al., 2004. Calcium, ATP, and ROS: a mitochondrial love-hate triangle. *American journal of physiology. Cell physiology*, 287(4), pp.C817–33.

Brostrom, C.O., Hunkeler, F.L. & Krebs, E.G., 1971. The regulation of skeletal muscle phosphorylase kinase by Ca2+. *The Journal of biological chemistry*, 246(7), pp.1961–7.

Buntinas, L. et al., 2001. The rapid mode of calcium uptake into heart mitochondria (RaM): comparison to RaM in liver mitochondria. *Biochimica et biophysica acta*, 1504(2-3), pp.248–61.

Cannavino, J. et al., 2014. PGC1-α over-expression prevents metabolic alterations and soleus muscle atrophy in hindlimb unloaded mice. *The Journal of physiology*, 592(Pt 20), pp.4575–89.

Cárdenas, C. & Foskett, J.K., 2012. Mitochondrial Ca(2+) signals in autophagy. *Cell calcium*, 52(1), pp.44–51.

Cereghetti, G.M. et al., 2008. Dephosphorylation by calcineurin regulates translocation of Drp1 to mitochondria. *Proceedings of the National Academy of Sciences of the United States of America*, 105(41), pp.15803–8.

Chance, B., 1965. The Energy-Linked Reaction of Calcium with Mitochondria. *J Biol Chem*, 240, pp.2729–2748.

Chelu, M.G. et al., 2006. Heat- and anesthesia-induced malignant hyperthermia in an RyR1 knock-in mouse. *FASEB journal : official publication of the Federation of American Societies for Experimental Biology*, 20(2), pp.329–30.

Chen, H. et al., 2010. Mitochondrial fusion is required for mtDNA stability in skeletal muscle and tolerance of mtDNA mutations. *Cell*, 141(2), pp.280–9.

Chen, H. et al., 2003. Mitofusins Mfn1 and Mfn2 coordinately regulate mitochondrial fusion and are essential for embryonic development. *The Journal of cell biology*, 160(2), pp.189–200.

Close, R.I., 1972. Dynamic properties of mammalian skeletal muscles. *Physiological reviews*, 52(1), pp.129–97.

Cooper, S.T. et al., 2004. C2C12 co-culture on a fibroblast substratum enables sustained survival of contractile, highly differentiated myotubes with peripheral nuclei and adult fast myosin expression. *Cell motility and the cytoskeleton*, 58(3), pp.200–11.

Cribbs, J.T. & Strack, S., 2007. Reversible phosphorylation of Drp1 by cyclic AMP-dependent protein kinase and calcineurin regulates mitochondrial fission and cell death. *EMBO reports*, 8(10), pp.939–44.

Crompton, M. & Andreeva, L., 1993. On the involvement of a mitochondrial pore in reperfusion injury. *Basic research in cardiology*, 88(5), pp.513–23.

Csordás, G. et al., 2013. MICU1 controls both the threshold and cooperative activation of the mitochondrial Ca^{2+} uniporter. *Cell metabolism*, 17(6), pp.976–87.

Csordás, G., Thomas, A.P. & Hajnóczky, G., 1999. Quasi-synaptic calcium signal transmission between endoplasmic reticulum and mitochondria. *The EMBO journal*, 18(1), pp.96–108.

Cusimano, V. et al., 2009. Assembly and dynamics of proteins of the longitudinal and junctional sarcoplasmic reticulum in skeletal muscle cells. *Proceedings of the National Academy of Sciences of the United*

States of America, 106(12), pp.4695–700.

D'Arcy, C.E. et al., 2008. King-denborough syndrome caused by a novel mutation in the ryanodine receptor gene. *Neurology*, 71(10), pp.776–7.

Dainese, M. et al., 2009. Anesthetic- and heat-induced sudden death in calsequestrin-1-knockout mice. *FASEB journal : official publication of the Federation of American Societies for Experimental Biology*, 23(6), pp.1710–20.

David, G., Barrett, J.N. & Barrett, E.F., 1998. Evidence that mitochondria buffer physiological Ca2+ loads in lizard motor nerve terminals. *The Journal of physiology*, 509 (Pt 1, pp.59–65.

Davidson, S.M. & Duchen, M.R., 2012. Imaging mitochondrial calcium signalling with fluorescent probes and single or two photon confocal microscopy. *Methods in molecular biology (Clifton, N.J.)*, 810, pp.219–34.

Deluca, H.F. & Engstrom, G.W., 1961. Calcium uptake by rat kidney mitochondria. *Proc Natl Acad Sci U S A*, 47, pp.1744–1750.

Denton, R.M., 2009. Regulation of mitochondrial dehydrogenases by calcium ions. *Biochimica et biophysica acta*, 1787(11), pp.1309–16.

Dirksen, R.T. & Avila, G., 2004. Distinct effects on Ca2+ handling caused by malignant hyperthermia and central core disease mutations in RyR1. *Biophysical journal*, 87(5), pp.3193–204.

Dowling, J.J. et al., 2011. King-Denborough syndrome with and without mutations in the skeletal muscle ryanodine receptor (RYR1) gene. *Neuromuscular disorders : NMD*, 21(6), pp.420–7.

Dowling, J.J. et al., 2012. Oxidative stress and successful antioxidant treatment in models of RYR1-related myopathy. *Brain : a journal of*

neurology, 135(Pt 4), pp.1115–27.

Drago, I., Pizzo, P. & Pozzan, T., 2011. After half a century mitochondrial calcium in- and efflux machineries reveal themselves. *EMBO J*, 30(20), pp.4119–4125.

Dubowitz, V. & Roy, S., 1970. Central core disease of muscle: clinical, histochemical and electron microscopic studies of an affected mother and child. *Brain : a journal of neurology*, 93(1), pp.133–46.

Duchen, M.R., 1992. Ca(2+)-dependent changes in the mitochondrial energetics in single dissociated mouse sensory neurons. *The Biochemical journal*, 283 (Pt 1, pp.41–50.

Duchen, M.R., 2000. Mitochondria and calcium: from cell signalling to cell death. *J Physiol*, 529 Pt 1, pp.57–68.

Duchen, M.R., 2004. Mitochondria in health and disease: perspectives on a new mitochondrial biology. *Molecular aspects of medicine*, 25(4), pp.365–451.

Durham, W.J. et al., 2008. RyR1 S-Nitrosylation Underlies Environmental Heat Stroke and Sudden Death in Y522S RyR1 Knockin Mice. *Cell*, 133(1), pp.53–65.

Efremov, R.G. et al., 2015. Architecture and conformational switch mechanism of the ryanodine receptor. *Nature*, 517(7532), pp.39–43.

Eisner, V., Lenaers, G. & Hajnóczky, G., 2014. Mitochondrial fusion is frequent in skeletal muscle and supports excitation-contraction coupling. *The Journal of cell biology*, 205(2), pp.179–95.

ENGEL, W.K. et al., 1961. Central core disease-an investigation of a rare muscle cell abnormality. *Brain : a journal of neurology*, 84, pp.167–85.

Falcone, S. et al., 2014. N-WASP is required for Amphiphysin-2/BIN1-dependent nuclear positioning and triad organization in skeletal muscle and is involved in the pathophysiology of centronuclear myopathy. *EMBO molecular medicine*, 6(11), pp.1455–75.

Fernandez-Fuente, M. et al., 2014. Calcium homeostasis in myogenic differentiation factor 1 (MyoD)-transformed, virally-transduced, skin-derived equine myotubes. *PloS one*, 9(8), p.e105971.

ffrench-Constant, C. et al., 2004. Neuroscience. The mysteries of myelin unwrapped. *Science (New York, N.Y.)*, 304(5671), pp.688–9.

Fill, M. & Copello, J.A., 2002. Ryanodine receptor calcium release channels. *Physiological reviews*, 82(4), pp.893–922.

Flucher, B.E., Phillips, J.L. & Powell, J.A., 1991. Dihydropyridine receptor alpha subunits in normal and dysgenic muscle in vitro: expression of alpha 1 is required for proper targeting and distribution of alpha 2. *The Journal of cell biology*, 115(5), pp.1345–56.

Fujimoto, K. et al., 2010. Targeting cyclophilin D and the mitochondrial permeability transition enhances beta-cell survival and prevents diabetes in Pdx1 deficiency. *Proceedings of the National Academy of Sciences of the United States of America*, 107(22), pp.10214–9.

Ge, X. et al., 2014. Stac3 inhibits myoblast differentiation into myotubes. *PloS one*, 9(4), p.e95926.

Giulivi, C. et al., 2011. Basal bioenergetic abnormalities in skeletal muscle from ryanodine receptor malignant hyperthermia-susceptible R163C knock-in mice. *The Journal of biological chemistry*, 286(1), pp.99–113.

Glancy, B. et al., 2015. Mitochondrial reticulum for cellular energy distribution in muscle. *Nature*, 523(7562), pp.617–20.

Glitsch, M.D., Bakowski, D. & Parekh, A.B., 2002. Store-operated Ca2+ entry depends on mitochondrial Ca2+ uptake. *The EMBO journal*, 21(24), pp.6744–54.

Guerrero-Hernández, A., Ávila, G. & Rueda, A., 2014. Ryanodine receptors as leak channels. *European journal of pharmacology*, 739, pp.26–38.

Haan, E.A. et al., 1990. Assignment of the gene for central core disease to chromosome 19. *Human genetics*, 86(2), pp.187–90.

Hakamata, Y. et al., 1992. Primary structure and distribution of a novel ryanodine receptor/calcium release channel from rabbit brain. *FEBS letters*, 312(2-3), pp.229–35.

Halestrap, A.P. et al., 1997. Cyclosporin A binding to mitochondrial cyclophilin inhibits the permeability transition pore and protects hearts from ischaemia/reperfusion injury. *Molecular and cellular biochemistry*, 174(1-2), pp.167–72.

Halestrap, A.P., 2009. What is the mitochondrial permeability transition pore? *Journal of molecular and cellular cardiology*, 46(6), pp.821–31.

HARMAN, D., 1972. The Biologic Clock: The Mitochondria? *Journal of the American Geriatrics Society*, 20(4), pp.145–147.

Haworth, R.A. & Hunter, D.R., 1979. The Ca2+-induced membrane transition in mitochondria. *Archives of Biochemistry and Biophysics*, 195(2), pp.460–467.

Hernandez-Lain, A. et al., 2011. de novo RYR1 heterozygous mutation (I4898T) causing lethal core–rod myopathy in twins. *European Journal of Medical Genetics*, 54(1), pp.29–33.

Hill, J.M. et al., 2014. Measuring baseline Ca(2+) levels in subcellular compartments using genetically engineered fluorescent indicators.

Methods in enzymology, 543, pp.47–72.

Hoffman, N.E. et al., 2013. MICU1 motifs define mitochondrial calcium uniporter binding and activity. *Cell reports*, 5(6), pp.1576–88.

Hoffman, N.E. et al., 2014. SLC25A23 augments mitochondrial Ca^{2+} uptake, interacts with MCU, and induces oxidative stress-mediated cell death. *Molecular biology of the cell*, 25(6), pp.936–47.

Hogan, P.G. et al., 2003. Transcriptional regulation by calcium, calcineurin, and NFAT. *Genes & development*, 17(18), pp.2205–32.

Hood, D.A., 2001. Invited Review: contractile activity-induced mitochondrial biogenesis in skeletal muscle. *Journal of applied physiology (Bethesda, Md. : 1985)*, 90(3), pp.1137–57.

Hopkins, P.M., 2011. Malignant hyperthermia. *Anaesthesia & Intensive Care Medicine*, 12(6), pp.263–265.

Hopkins, P.M., 2006. Skeletal muscle physiology. *Continuing Education in Anaesthesia, Critical Care & Pain*, 6(1), pp.1–6.

Horstick, E.J. et al., 2013. Stac3 is a component of the excitation-contraction coupling machinery and mutated in Native American myopathy. *Nature communications*, 4, p.1952.

Hou, T. et al., 2012. Characterization of domain-peptide interaction interface: prediction of SH3 domain-mediated protein-protein interaction network in yeast by generic structure-based models. *Journal of proteome research*, 11(5), pp.2982–95.

Hung, V. et al., 2014. Proteomic mapping of the human mitochondrial intermembrane space in live cells via ratiometric APEX tagging. *Molecular cell*, 55(2), pp.332–41.

Hunter, D.R. & Haworth, R.A., 1979. The Ca2+-induced membrane transition in mitochondria. *Archives of Biochemistry and Biophysics*, 195(2), pp.453–459.

Inui, M., Saito, A. & Fleischer, S., 1987. Purification of the ryanodine receptor and identity with feet structures of junctional terminal cisternae of sarcoplasmic reticulum from fast skeletal muscle. *J. Biol. Chem.*, 262(4), pp.1740–1747.

Isaacs, H., Heffron, J.J. & Badenhorst, M., 1975. Central core disease. A correlated genetic, histochemical, ultramicroscopic, and biochemical study. *Journal of neurology, neurosurgery, and psychiatry*, 38(12), pp.1177–86.

Jeyaraju, D. V, Cisbani, G. & Pellegrini, L., 2009. Calcium regulation of mitochondria motility and morphology. *Biochimica et biophysica acta*, 1787(11), pp.1363–73.

Jones, D.A. & Round, J.M., 1990. *Skeletal muscle in health and disease: a textbook of muscle physiology*, Manchester University Press.

Jungbluth, H., 2007a. Central core disease. *Orphanet journal of rare diseases*, 2, p.25.

Jungbluth, H. et al., 2009. Late-onset axial myopathy with cores due to a novel heterozygous dominant mutation in the skeletal muscle ryanodine receptor (RYR1) gene. *Neuromuscular disorders : NMD*, 19(5), pp.344–7.

Jungbluth, H., 2007b. Multi-minicore Disease. *Orphanet journal of rare diseases*, 2, p.31.

Jungbluth, H., Sewry, C.A. & Muntoni, F., 2011. Core myopathies. *Seminars in pediatric neurology*, 18(4), pp.239–49.

Kabeya, Y. et al., 2000. LC3, a mammalian homologue of yeast Apg8p, is localized in autophagosome membranes after processing. *The EMBO journal*, 19(21), pp.5720–8.

Kaddour-Djebbar, I. et al., 2010. Specific mitochondrial calcium overload induces mitochondrial fission in prostate cancer cells. *International journal of oncology*, 36(6), pp.1437–44.

Kamer, K.J. & Mootha, V.K., 2014. MICU1 and MICU2 play nonredundant roles in the regulation of the mitochondrial calcium uniporter. *EMBO reports*, 15(3), pp.299–307.

De Koninck, P. & Schulman, H., 1998. Sensitivity of CaM kinase II to the frequency of Ca2+ oscillations. *Science (New York, N.Y.)*, 279(5348), pp.227–30.

Krause, T. et al., 2004. Dantrolene--a review of its pharmacology, therapeutic use and new developments. *Anaesthesia*, 59(4), pp.364–73.

Kuo, I.Y. & Ehrlich, B.E., 2015. Muscling in on the ryanodine receptor. *Nature structural & molecular biology*, 22(2), pp.106–7.

Kwong, J.Q. et al., 2015. The Mitochondrial Calcium Uniporter Selectively Matches Metabolic Output to Acute Contractile Stress in the Heart. *Cell Reports*, 12(1), pp.15–22.

de la Fuente, S. et al., 2014. Dynamics of mitochondrial Ca2+ uptake in MICU1-knockdown cells. *The Biochemical journal*, 458(1), pp.33–40.

Lai, F.A. et al., 1988. Purification and reconstitution of the calcium release channel from skeletal muscle. *Nature*, 331(6154), pp.315–9.

Lam, S.S. et al., 2014. Directed evolution of APEX2 for electron microscopy and proximity labeling. *Nature Methods*, 12(1), pp.51–54.

Lanner, J.T. et al., 2010. Ryanodine receptors: structure, expression, molecular details, and function in calcium release. *Cold Spring Harbor perspectives in biology*, 2(11), p.a003996.

Larach, M.G. et al., 2010. Clinical presentation, treatment, and complications of malignant hyperthermia in North America from 1987 to 2006. *Anesthesia and analgesia*, 110(2), pp.498–507.

Larsson, N.G. et al., 1998. Mitochondrial transcription factor A is necessary for mtDNA maintenance and embryogenesis in mice. *Nature genetics*, 18(3), pp.231–6.

Lauren Cornall, D.H.M.M. and A.M., 2012. *Muscle Biopsy* C. Sundaram, ed., InTech.

Lazarou, M. et al., 2015. The ubiquitin kinase PINK1 recruits autophagy receptors to induce mitophagy. *Nature*, 524(7565), pp.309–314.

Legha, W. et al., 2010. stac1 and stac2 genes define discrete and distinct subsets of dorsal root ganglia neurons. *Gene expression patterns : GEP*, 10(7-8), pp.368–75.

Lehninger, A.L., 1970. Mitochondria and calcium ion transport. *Biochem J*, 119(2), pp.129–138.

Lieber, R.L., 1992. *Skeletal Muscle Structure and Function: Implications for Rehabilitation and Sports Medicine* J. P. Butler, ed., Williams & Wilkins.

Lin, J. et al., 2002. Transcriptional co-activator PGC-1 alpha drives the formation of slow-twitch muscle fibres. *Nature*, 418(6899), pp.797–801.

Lodish, H. et al., 2000. *Molecular Cell Biology* 4th ed., W. H. Freeman.

Logan, C. V et al., 2014. Loss-of-function mutations in MICU1 cause a brain and muscle disorder linked to primary alterations in mitochondrial

calcium signaling. *Nature genetics*, 46(2), pp.188–93.

Losón, O.C. et al., 2013. Fis1, Mff, MiD49, and MiD51 mediate Drp1 recruitment in mitochondrial fission. *Molecular biology of the cell*, 24(5), pp.659–67.

Loy, R.E. et al., 2011. Muscle weakness in Ryr1I4895T/WT knock-in mice as a result of reduced ryanodine receptor Ca2+ ion permeation and release from the sarcoplasmic reticulum. *The Journal of general physiology*, 137(1), pp.43–57.

Luongo, T.S. et al., 2015. The Mitochondrial Calcium Uniporter Matches Energetic Supply with Cardiac Workload during Stress and Modulates Permeability Transition. *Cell Reports*, 12(1), pp.23–34.

Lynch, P.J. et al., 1999. A mutation in the transmembrane/luminal domain of the ryanodine receptor is associated with abnormal Ca2+ release channel function and severe central core disease. *Proceedings of the National Academy of Sciences*, 96(7), pp.4164–4169.

MacVicar, T.D.B. & Lane, J.D., 2014. Impaired OMA1-dependent cleavage of OPA1 and reduced DRP1 fission activity combine to prevent mitophagy in cells that are dependent on oxidative phosphorylation. *Journal of cell science*, 127(Pt 10), pp.2313–25.

MAGEE, K.R. & SHY, G.M., 1956. A new congenital non-progressive myopathy. *Brain : a journal of neurology*, 79(4), pp.610–21.

Mallilankaraman, K., Cárdenas, C., et al., 2012. MCUR1 is an essential component of mitochondrial Ca2+ uptake that regulates cellular metabolism. *Nature cell biology*, 14(12), pp.1336–43.

Mallilankaraman, K., Doonan, P., et al., 2012. MICU1 is an essential gatekeeper for MCU-mediated mitochondrial Ca(2+) uptake that regulates cell survival. *Cell*, 151(3), pp.630–44.

Mamchaoui, K. et al., 2011. Immortalized pathological human myoblasts: towards a universal tool for the study of neuromuscular disorders. *Skeletal muscle*, 1(1), p.34.

Mammucari, C. et al., 2007. FoxO3 controls autophagy in skeletal muscle in vivo. *Cell metabolism*, 6(6), pp.458–71.

Mammucari, C. et al., 2015. The mitochondrial calcium uniporter controls skeletal muscle trophism in vivo. *Cell reports*, 10(8), pp.1269–79.

Maravall, M. et al., 2000. Estimating intracellular calcium concentrations and buffering without wavelength ratioing. *Biophysical journal*, 78(5), pp.2655–67.

Marroquin, L.D. et al., 2007. Circumventing the Crabtree Effect: Replacing Media Glucose with Galactose Increases Susceptibility of HepG2 Cells to Mitochondrial Toxicants. *Toxicological Sciences*, 97(2), pp.539–547.

Mitchell, P., 1961. Coupling of phosphorylation to electron and hydrogen transfer by a chemi-osmotic type of mechanism. *Nature*, 191, pp.144–8.

Monnier, N. et al., 2001. Familial and sporadic forms of central core disease are associated with mutations in the C-terminal domain of the skeletal muscle ryanodine receptor. *Human molecular genetics*, 10(22), pp.2581–92.

Montero, M. et al., 2000. Chromaffin-cell stimulation triggers fast millimolar mitochondrial Ca2+ transients that modulate secretion. *Nature cell biology*, 2(2), pp.57–61.

Moyle, J. & Mitchell, P., 1977. Electric charge stoicheiometry of calcium translocation in rat liver mitochondria. *FEBS Letters*, 73(2), pp.131–136.

Mulley, J.C. et al., 1993. Refined genetic localization for central core disease. *American journal of human genetics*, 52(2), pp.398–405.

Murphy, E. et al., 2014. Unresolved questions from the analysis of mice lacking MCU expression. *Biochemical and biophysical research communications*, 449(4), pp.384–5.

Nakai, J. et al., 1990. Primary structure and functional expression from cDNA of the cardiac ryanodine receptor/calcium release channel. *FEBS letters*, 271(1-2), pp.169–77.

Nelson, B.R. et al., 2013. Skeletal muscle-specific T-tubule protein STAC3 mediates voltage-induced Ca2+ release and contractility. *Proceedings of the National Academy of Sciences of the United States of America*, 110(29), pp.11881–6.

Norwood, F.L.M. et al., 2009. Prevalence of genetic muscle disease in Northern England: in-depth analysis of a muscle clinic population. *Brain : a journal of neurology*, 132(Pt 11), pp.3175–86.

Otsu, K. et al., 1990. Molecular cloning of cDNA encoding the Ca2+ release channel (ryanodine receptor) of rabbit cardiac muscle sarcoplasmic reticulum. *The Journal of biological chemistry*, 265(23), pp.13472–83.

Palma, E. et al., 2009. Genetic ablation of cyclophilin D rescues mitochondrial defects and prevents muscle apoptosis in collagen VI myopathic mice. *Human molecular genetics*, 18(11), pp.2024–31.

Palty, R. et al., 2010. NCLX is an essential component of mitochondrial Na+/Ca2+ exchange. *Proceedings of the National Academy of Sciences of the United States of America*, 107(1), pp.436–41.

Pan, X. et al., 2013. The physiological role of mitochondrial calcium revealed by mice lacking the mitochondrial calcium uniporter. *Nature cell biology*, 15(12), pp.1464–72.

Paolini, C. et al., 2015. Oxidative stress, mitochondrial damage, and cores in muscle from calsequestrin-1 knockout mice. *Skeletal Muscle*, 5(1), p.10.

Paolini, C. et al., 2007. Reorganized stores and impaired calcium handling in skeletal muscle of mice lacking calsequestrin-1. *The Journal of physiology*, 583(Pt 2), pp.767–84.

Patron, M. et al., 2014. MICU1 and MICU2 finely tune the mitochondrial Ca2+ uniporter by exerting opposite effects on MCU activity. *Molecular cell*, 53(5), pp.726–37.

Patthy, L. & Nikolics, K., 1993. Functions of agrin and agrin-related proteins. *Trends in neurosciences*, 16(2), pp.76–81.

Paupe, V. et al., 2015. CCDC90A (MCUR1) is a cytochrome c oxidase assembly factor and not a regulator of the mitochondrial calcium uniporter. *Cell metabolism*, 21(1), pp.109–16.

Perocchi, F. et al., 2010. MICU1 encodes a mitochondrial EF hand protein required for Ca(2+) uptake. *Nature*, 467(7313), pp.291–6.

Pesta, D. & Gnaiger, E., 2012. High-resolution respirometry: OXPHOS protocols for human cells and permeabilized fibers from small biopsies of human muscle. *Methods in molecular biology (Clifton, N.J.)*, 810, pp.25–58.

Petersen, J. et al., 2012. Comparison of the H+/ATP ratios of the H+-ATP synthases from yeast and from chloroplast. *Proceedings of the National Academy of Sciences of the United States of America*, 109(28), pp.11150–5.

Picca, A. et al., 2013. Aging and calorie restriction oppositely affect mitochondrial biogenesis through TFAM binding at both origins of mitochondrial DNA replication in rat liver. *PloS one*, 8(9), p.e74644.

Plovanich, M. et al., 2013. MICU2, a paralog of MICU1, resides within the mitochondrial uniporter complex to regulate calcium handling. *PloS one*, 8(2), p.e55785.

Polster, A. et al., 2015. Stac adaptor proteins regulate trafficking and function of muscle and neuronal L-type Ca2+ channels. *Proceedings of the National Academy of Sciences of the United States of America*, 112(2), pp.602–6.

Powers, S.K. et al., 2012. Mitochondrial signaling contributes to disuse muscle atrophy. *American journal of physiology. Endocrinology and metabolism*, 303(1), pp.E31–9.

Quan, X. et al., 2015. Essential role of mitochondrial Ca2+ uniporter in the generation of mitochondrial pH gradient and metabolism-secretion coupling in insulin-releasing cells. *The Journal of biological chemistry*, 290(7), pp.4086–96.

Quane, K.A. et al., 1993. Mutations in the ryanodine receptor gene in central core disease and malignant hyperthermia. *Nature genetics*, 5(1), pp.51–5.

Quinlivan, R.M. et al., 2003. Central core disease: clinical, pathological, and genetic features. *Archives of disease in childhood*, 88(12), pp.1051–5.

Raffaello, A. et al., 2013. The mitochondrial calcium uniporter is a multimer that can include a dominant-negative pore-forming subunit. *The EMBO journal*, 32(17), pp.2362–76.

Rao, V.K., Carlson, E.A. & Yan, S.S., 2014. Mitochondrial permeability transition pore is a potential drug target for neurodegeneration. *Biochimica et biophysica acta*, 1842(8), pp.1267–72.

Rasola, A. & Bernardi, P., 2011. Mitochondrial permeability transition in Ca(2+)-dependent apoptosis and necrosis. *Cell calcium*, 50(3), pp.222–33.

Reinholt, B.M. et al., 2013. Stac3 is a novel regulator of skeletal musReinholt, B. M., Ge, X., Cong, X., Gerrard, D. E., & Jiang, H. (2013).

Stac3 is a novel regulator of skeletal muscle development in mice. PloS One, 8(4), e62760. http://doi.org/10.1371/journal.pone.0062760cle deve. *PloS one*, 8(4), p.e62760.

Reitzer, L.J., Wice, B.M. & Kennell, D., 1979. Evidence that glutamine, not sugar, is the major energy source for cultured HeLa cells. *The Journal of biological chemistry*, 254(8), pp.2669–76.

Rizzuto, R. et al., 1998. Close contacts with the endoplasmic reticulum as determinants of mitochondrial Ca2+ responses. *Science (New York, N.Y.)*, 280(5370), pp.1763–6.

Rizzuto, R. et al., 1993. Microdomains with high Ca2+ close to IP3-sensitive channels that are sensed by neighboring mitochondria. *Science*, 262(5134), pp.744–747.

Rizzuto, R. et al., 2012. Mitochondria as sensors and regulators of calcium signalling. *Nature reviews. Molecular cell biology*, 13(9), pp.566–78.

Rizzuto, R. et al., 1992. Rapid changes of mitochondrial Ca2+ revealed by specifically targeted recombinant aequorin. *Nature*, 358(6384), pp.325–7.

Robinson, B.H., 1996. *Mitochondrial Biogenesis and Genetics Part B*, Elsevier.

Robinson, B.H. et al., 1992. Nonviability of cells with oxidative defects in galactose medium: a screening test for affected patient fibroblasts. *Biochemical medicine and metabolic biology*, 48(2), pp.122–6.

Robinson, R. et al., 2006. Mutations in RYR1 in malignant hyperthermia and central core disease. *Human mutation*, 27(10), pp.977–89.

Romanello, V. et al., 2010. Mitochondrial fission and remodelling contributes to muscle atrophy. *The EMBO journal*, 29(10), pp.1774–85.

Romanello, V. & Sandri, M., 2010. Mitochondrial biogenesis and fragmentation as regulators of muscle protein degradation. *Current hypertension reports*, 12(6), pp.433–9.

Romero, N.B. et al., 2003. Dominant and recessive central core disease associated with RYR1 mutations and fetal akinesia. *Brain : a journal of neurology*, 126(Pt 11), pp.2341–9.

Rosenberg, H. et al., 2015. Malignant hyperthermia: a review. *Orphanet journal of rare diseases*, 10(1), p.93.

Rossi, D. et al., 2014. A mutation in the CASQ1 gene causes a vacuolar myopathy with accumulation of sarcoplasmic reticulum protein aggregates. *Human mutation*, 35(10), pp.1163–70.

Rossignol, R., 2004. Energy Substrate Modulates Mitochondrial Structure and Oxidative Capacity in Cancer Cells. *Cancer Research*, 64(3), pp.985–993.

Sancak, Y. et al., 2013. EMRE is an essential component of the mitochondrial calcium uniporter complex. *Science (New York, N.Y.)*, 342(6164), pp.1379–82.

Sanderson, M.J. et al., 1994. Mechanisms and function of intercellular calcium signaling. *Molecular and Cellular Endocrinology*, 98(2), pp.173–187.

Sandri, M. et al., 2006. PGC-1alpha protects skeletal muscle from atrophy by suppressing FoxO3 action and atrophy-specific gene transcription. *Proceedings of the National Academy of Sciences of the United States of America*, 103(44), pp.16260–5.

Satoh, J., Nanri, Y. & Yamamura, T., 2006. Rapid identification of 14-3-3-binding proteins by protein microarray analysis. *Journal of neuroscience methods*, 152(1-2), pp.278–88.

Scarpulla, R.C., 2011. Metabolic control of mitochondrial biogenesis through the PGC-1 family regulatory network. *Biochimica et biophysica acta*, 1813(7), pp.1269–78.

Scarpulla, R.C., 2008. Transcriptional paradigms in mammalian mitochondrial biogenesis and function. *Physiological reviews*, 88(2), pp.611–38.

Sciote, J.J. & Morris, T.J., 2014. Skeletal Muscle Function and Fibre Types: the Relationship Between Occlusal Function and the Phenotype of Jaw-closing Muscles in Human. *http://dx.doi.org.libproxy.ucl.ac.uk/10.1093/ortho/27.1.15*.

Sena, L.A. & Chandel, N.S., 2012. Physiological roles of mitochondrial reactive oxygen species. *Molecular cell*, 48(2), pp.158–67.

Shulga, N., Wilson-Smith, R. & Pastorino, J.G., 2010. Sirtuin-3 deacetylation of cyclophilin D induces dissociation of hexokinase II from the mitochondria. *Journal of cell science*, 123(Pt 6), pp.894–902.

Skram, M.K. et al., 2009. Muscle biopsies in children--an evaluation of histopathology and clinical value during a 5-year period. *Upsala journal of medical sciences*, 114(1), pp.41–5.

Skulačev, V.P., Hinkle, P.C. & Mitchell, P.D., 1981. *Chemiosmotic proton circuits in biological membranes*, Addison-Wesley, Advanced Book Program/World Science Division.

Skulachev, V.P., 2001. Mitochondrial filaments and clusters as intracellular power-transmitting cables. *Trends in Biochemical Sciences*, 26(1), pp.23–29.

Sparagna, G.C. et al., 1995. Mitochondrial calcium uptake from physiological-type pulses of calcium. A description of the rapid uptake mode. *The Journal of biological chemistry*, 270(46), pp.27510–5.

Stamm, D.S. et al., 2008. Native American myopathy: congenital myopathy with cleft palate, skeletal anomalies, and susceptibility to malignant hyperthermia. *American journal of medical genetics. Part A*, 146A(14), pp.1832–41.

Stamm, D.S. et al., 2008. Novel congenital myopathy locus identified in Native American Indians at 12q13.13-14.1. *Neurology*, 71(22), pp.1764–9.

De Stefani, D. et al., 2011. A forty-kilodalton protein of the inner membrane is the mitochondrial calcium uniporter. *Nature*, 476(7360), pp.336–340.

Stewart, C.R., Kahler, S.G. & Gilchrist, J.M., 1988. Congenital myopathy with cleft palate and increased susceptibility to malignant hyperthermia: King syndrome? *Pediatric neurology*, 4(6), pp.371–4.

Swaiman, K.F. et al., 2011. *Swaiman's Pediatric Neurology: Principles and Practice* 5th ed., Elsevier Health Sciences.

Szabadkai, G. et al., 2004. Drp-1-dependent division of the mitochondrial network blocks intraorganellar Ca2+ waves and protects against Ca2+-mediated apoptosis. *Molecular cell*, 16(1), pp.59–68.

Szalai, G. et al., 2000. Calcium signal transmission between ryanodine receptors and mitochondria. *The Journal of biological chemistry*, 275(20), pp.15305–13.

Takahashi, K. & Yamanaka, S., 2006. Induction of pluripotent stem cells from mouse embryonic and adult fibroblast cultures by defined factors. *Cell*, 126(4), pp.663–76.

Takeshima, H. et al., 1989. Primary structure and expression from complementary DNA of skeletal muscle ryanodine receptor. *Nature*, 339(6224), pp.439–45.

Telerman-Toppet, N., Gerard, J.M. & Coërs, C., 1973. Central core disease. *Journal of the Neurological Sciences*, 19(2), pp.207–223.

Tinel, H. et al., 1999. Active mitochondria surrounding the pancreatic acinar granule region prevent spreading of inositol trisphosphate-evoked local cytosolic Ca(2+) signals. *The EMBO journal*, 18(18), pp.4999–5008.

Tong, J., McCarthy, T. V & MacLennan, D.H., 1999. Measurement of resting cytosolic Ca2+ concentrations and Ca2+ store size in HEK-293 cells transfected with malignant hyperthermia or central core disease mutant Ca2+ release channels. *The Journal of biological chemistry*, 274(2), pp.693–702.

Twig, G. et al., 2008. Fission and selective fusion govern mitochondrial segregation and elimination by autophagy. *The EMBO journal*, 27(2), pp.433–46.

Vainshtein, A. et al., 2015. PGC-1α modulates denervation-induced mitophagy in skeletal muscle. *Skeletal muscle*, 5, p.9.

Vais, H. et al., 2015. MCUR1, CCDC90A, Is a Regulator of the Mitochondrial Calcium Uniporter. *Cell Metabolism*, 22(4), pp.533–535.

VASINGTON, F.D. & MURPHY, J. V, 1962. Ca ion uptake by rat kidney mitochondria and its dependence on respiration and phosphorylation. *The Journal of biological chemistry*, 237, pp.2670–7.

Weintraub, H. et al., 1989. Activation of muscle-specific genes in pigment, nerve, fat, liver, and fibroblast cell lines by forced expression of MyoD. *Proceedings of the National Academy of Sciences of the United States of America*, 86(14), pp.5434–8.

Westermann, B., 2010. Mitochondrial fusion and fission in cell life and death. *Nature reviews. Molecular cell biology*, 11(12), pp.872–84.

Wu, S. et al., 2006. Central core disease is due to RYR1 mutations in more than 90% of patients. *Brain : a journal of neurology*, 129(Pt 6), pp.1470–80.

Wu, Z. et al., 1999. Mechanisms Controlling Mitochondrial Biogenesis and Respiration through the Thermogenic Coactivator PGC-1. *Cell*, 98(1), pp.115–124.

Yan, Z. et al., 2015. Structure of the rabbit ryanodine receptor RyR1 at near-atomic resolution. *Nature*, 517(7532), pp.50–5.

Yang, T. et al., 2006. Pharmacologic and Functional Characterization of Malignant Hyperthermia in the R163C RyR1 Knock-in Mouse. *The Journal of the American Society of Anesthesiologists*, 105(6), pp.1164–1175.

Yi, M., Weaver, D. & Hajnóczky, G., 2004. Control of mitochondrial motility and distribution by the calcium signal: a homeostatic circuit. *The Journal of cell biology*, 167(4), pp.661–72.

Youle, R.J. & van der Bliek, A.M., 2012. Mitochondrial fission, fusion, and stress. *Science (New York, N.Y.)*, 337(6098), pp.1062–5.

Youle, R.J. & Karbowski, M., 2005. Mitochondrial fission in apoptosis. *Nature reviews. Molecular cell biology*, 6(8), pp.657–63.

Youle, R.J. & Narendra, D.P., 2011. Mechanisms of mitophagy. *Nature reviews. Molecular cell biology*, 12(1), pp.9–14.

Yuen, B. et al., 2011. Mice expressing T4826I-RYR1 are viable but exhibit sex- and genotype-dependent susceptibility to malignant hyperthermia and muscle damage. *The FASEB Journal*, 26(3), pp.1311–1322.

Zaharieva, I.T. et al., 2014. G.P.261 Whole exome sequencing in patients with congenital myopathies. In *Neuromuscular Disorders*. p. 895.

Zalk, R. et al., 2015. Structure of a mammalian ryanodine receptor. *Nature*, 517(7532), pp.44–49.

Zhang, Y. et al., 1993. A mutation in the human ryanodine receptor gene associated with central core disease. *Nature genetics*, 5(1), pp.46–50.

Zhang, Y. et al., 2014. Identification of the STAC3 gene as a skeletal muscle-specifically expressed gene and a novel regulator of satellite cell differentiation in cattle. *Journal of animal science*, 92(8), pp.3284–90.

Zhou, H. et al., 2006. Epigenetic Allele Silencing Unveils Recessive RYR1 Mutations in Core Myopathies. *The American Journal of Human Genetics*, 79(5), pp.859–868.

Zhou, H. et al., 2007. Molecular mechanisms and phenotypic variation in RYR1-related congenital myopathies. *Brain : a journal of neurology*, 130(Pt 8), pp.2024–36.

Zorzato, F. et al., 1990. Molecular cloning of cDNA encoding human and rabbit forms of the Ca2+ release channel (ryanodine receptor) of skeletal muscle sarcoplasmic reticulum. *J. Biol. Chem.*, 265(4), pp.2244–2256.

Zvaritch, E. et al., 2007. An Ryr1I4895T mutation abolishes Ca2+ release channel function and delays development in homozygous offspring of a mutant mouse line. *Proceedings of the National Academy of Sciences*, 104(47), pp.18537–18542.

Zvaritch, E. et al., 2009. Ca2+ dysregulation in Ryr1(I4895T/wt) mice causes congenital myopathy with progressive formation of minicores, cores, and nemaline rods. *Proceedings of the National Academy of Sciences of the United States of America*, 106(51), pp.21813–8.